UNIVERSIDADE DE SÃO PAULO

INSTITUTO DE FÍSICA DE SÃO CARLOS

LARA MALDANIS CERQUEIRA PERES

3D X-ray imaging of Precambrian microfossils: evaluating biogenicity at the nanoscale with ptychographic X-ray computed tomography

São Carlos

2019

LARA MALDANIS CERQUEIRA PERES

3D X-ray imaging of Precambrian microfossils: evaluating biogenicity at the nanoscale with ptychographic x-ray computed tomography

Thesis presented to the Graduate Program in Physics at the Instituto de Física de São Carlos, Universidade de São Paulo to obtain the degree of Doctor of Science.

Concentration area: Applied Physics
Option: Biomolecular Physics

Advisor: Dr. Douglas Galante

Corrected Version
(original version available on the Program Unit)

São Carlos
2019

Peres, Lara Maldanis Cerqueira
3D X-ray imaging of Precambrian microfossils: evaluating biogenicity at the nanoscale with ptychographic X-ray computed tomography / Lara Maldanis Cerqueira Peres; advisor Douglas Galante - corrected version -- São Carlos 2019.
142 p.

Thesis (Doctorate - Graduate Program in Física Aplicada Biomolecular) -- Instituto de Física de São Carlos, Universidade de São Paulo - Brasil , 2019.

1. Biogenicity. 2. Precambrian microfossils. 3. Ptychographic X-ray computed tomography. 4. Paleobiology. I. Galante, Douglas, advisor. II. Title.

ACKNOWLEDGEMENTS

First, I would like to thank CAPES and FAPESP for the scholarships, FAPESP for the funding of this project (2015/21810-6) and international internship (BEPE project 2016/25681-9), and also to CNPq and Instituto Serrapilheira for the financial support to our team during the experiments abroad.

Some people were fundamental to the development of this work in several aspects, way beyond the professional one, so I would like to acknowledge them:

First, the person who was my main partner during these years of PhD, my dear friend and supervisor, Douglas Galante. Thank you for always believing in me (many times even more than myself!), since I was only a young biologist, starting to be interested about this crazy world of synchrotron physics. This trust, alongside with all the opportunities that you've offered me were fundamental for my development into the scientist and person that I am today. Thank you also for all the great moments of true friendship and partnership, whether during beamtimes, drinking or even climbing mountains, among countless others. I admire you not only for the great scientist who you are, but also as one of the greatest hearts that I've ever met (and I'm not taking only because of your infinite patience with my last-minutes requests!).

I would like also to thank my host supervisor in France, Loïc Bertrand for kindly receiving me in his lab, supervising me during my stay and providing me several opportunities within the international community. I really appreciate your continuous support to the development of this research but also to my professional and academic career. Merci beaucoup!

Talking about France, my 15 months in this country wouldn't have been so nice if not for the nice colleagues and friends that I had the chance to meet in IPANEMA. A great thanks to my office and "cafecito" partners, Victoria, and Patricio for the every-day time spent together, to Pierre for the collaborations and support in several experiments and ongoing projects, and also to Bénedicte, Selwin, Rafaella, Josiane, Cécile, Jiayi and Maëva for al the good moments full of nice conversations, beers, and for all the relaxed and informal French and science lessons. Also, a big thanks to the other Ipanemians who were more than even nice colleagues, always supporting me for everything that I needed and always making me feel like home: Regina, Sophie, Anne-Fleur, Serge, Sebastian and Mathieu.

I would like to thank Dr. Frances Westall from CBM-Orléans, for the support and collaboration that constituted the fundamental basis of this project, for providing all the samples and being always helpful to discuss our results. Thank you also MSc. Keyron Hickman-Lewis, for being a true partner and helping me to carry on all the experimental part, with choosing and preparing the samples, participating in the synchrotron experiments until manuscript writing. Thank you also for the all great moments sharing with me beers and part of your knowledge and enthusiasm with early life sciences.

I would like to thank the staff of the cSAXS beamline who supported me during the experiments, particularly our local contact Mariana Verezhak, who was part of our two beamtimes, always extremely accessible and helpful, and fundamental for the development of the data treatment approach. Thank you also Manuel Guizar-Sicairos for joining us with your expertise that was an important differential.

Thank you, Felisa Berenguer, from Soleil Synchrotron, for the support in the development of this project and for guiding us in the first round of ptychography experiments at Cristal beamline, which, although not successful, comprised the first steps of fundamental importance for the following fruitful developments of this project.

Thanks André Freitas from the Centro Brasileiro de Pesquisas Físicas for accepting this collaboration and kindly conducting part of the FIB-based sample preparations.

And also Prof. Ricardo Trindade and Plinio Jaqueto for the support with the magnetic analysis for the manuscript, and the financial support with the thematic project.

This work could not have been realized without the support of the Brazilian Synchrotron Light Laboratory (LNLS), providing me all the infrastructure for the development of this PhD and financial support for the costly sample preparation.

Aos colegas e amigos do LNLS e Astroliga com quem compartilhei muitas risadas, momentos gostosos e que me ensinaram e ajudaram muito ao longo de todos esses anos: Fabio, Adriano, Tami, Flávia, Maria Fernanda, Nathaly, Bianca, Marcelo, Verônica, João Júlio, Camili. Um agradecimento cheio de saudade ao Rodrigo por todo o carinho que teve comigo e por ter sido me servido de exemplo de como ser uma pessoa um pouco melhor.

E por fim gostaria de agradecer especialmente às pessoas que são fundamentais na minha vida e que sempre foram os maiores entusiastas e apoiadores de cada um dos meus passos:

Heloisa, cuja “ajuda em termodinâmica” que começou em 2015 mudou minha forma de ser e ver o mundo. Sua parceria e companheirismo se estendem a todos os aspectos da minha vida e sou muito grata por isso!

E por fim, acredito que nosso florescer depende muito de nossas raízes. Gostaria então de agradecer meu pai Marcelus e minha mãe Anatália pela base sólida que me proporcionaram, regada de constante apoio, amor e incentivo, que permitiram que a semente de cientista dentro de mim pudesse crescer e desabrochar chegando até onde pude chegar hoje. Um agradecimento também com muito carinho às minhas queridas irmãs e parceiras ao longo de todos esses anos, Fabiola e Mariana.

“Enquanto os homens exercem seus podres poderes,
motos e fuscas avançam os sinais vermelhos
e perdem os verdes. Somos uns boçais”

Caetano Veloso, 1984

ABSTRACT

PERES, L. M. C. **3D X-ray imaging of Precambrian microfossils:** evaluating biogenicity at the nanoscale with ptychographic X-Ray computed tomography. 2019. 142 p. Thesis (Doctor in Science) - Instituto de Física de São Carlos, Universidade de São Paulo, São Carlos, 2019.

Precambrian microfossils are structures difficult to be investigated by means of conventional imaging approaches due to their small size, geochemical composition and relative scarcity that limits the use of destructive methods. One recurrent problem in the study of these earliest life forms relies on attesting their biogenicity given that structures formed abiotically can strongly resemble fossilized cells of simple morphology. The search of novel analytical methods for contributing to the evaluation of these ancient structures is of great importance for the development of the field of Precambrian paleobiology. In this work, the coherent X-ray imaging approach of ptychographic X-ray computed tomography is explored for assessing *bona fide* microfossils from the Gunflint Formation, Canada, the Draken Formation, Norway and early Archean controversial structures described as fossil bacteria from the Hoogenoeg and Kromberg Formations of the Barberton Greenstone Belt, South Africa. The microfossils were imaged non-destructively in 3D with nanometric resolution and quantitative electron density contrast, which allowed the estimation of mass density of the materials. The tomographic images provided information on both the morphology and geochemical composition of the specimens at the nanoscale within a microscale context. From the morphological data, it was possible to distinguish the 3D distribution of kerogenous material, which revealed a novel preservation pattern and traces of taphonomic alterations for filaments of Gunflint Formation, and ultrastructural details preserved in cell walls of specimen from Draken Formation. The mass density quantification provided supporting evidences, such as the discrimination of kerogen maturation states and identification of minerals, providing also a picture of the taphonomic history of the specimens. Based in the biogenicity criteria investigated at the nanoscale, we could not attest the biogenicity of the structures described in the Barberton Greenstone Belt, but we offered new possible interpretations of biological and biotic origins for the formation of these structures. The results represent significative advances for the comprehension of fossilized microorganisms and add important contribution for the assessment of biogenicity through a robust combination of morphological and geochemical 3D information from the nano to the micron-scale.

Keywords: Biogenicity. Precambrian microfossils. Ptychographic X-ray computed tomography. Paleobiology.

RESUMO

PERES, L. M. C. **Imageamento por raios-X em 3D de microfósseis Pré-Cambrianos:** avaliando a biogenicidade na nanoescala com Tomografia Pticográfica de Raios-X. 2019. 142 p. Tese (Doutorado em Ciências) - Instituto de Física de São Carlos, Universidade de São Paulo, São Carlos, 2019.

Microfósseis Pré-Cambrianos são estruturas difíceis de serem investigadas por técnicas de imagem convencionais devido ao seu pequeno tamanho, composição geoquímica e por serem relativamente raros no registro geológico, o que limita o uso de técnicas destrutivas. Um problema recorrente no estudo dessas primeiras formas de vida é em se atestar sua biogenicidade uma vez que estruturas formadas abioticamente podem difíceis de serem distinguidas de células fossilizadas de simples morfologia. A busca de novos métodos analíticos para contribuir na avaliação dessas estruturas é de grande import6ancia para o desenvolvimento da área de paleobiologia Pré-Cambriana. Neste trabalho, a técnica de imagem de raios X coerente de Tomografia Pticográfica de Raios X foi explorada para investigar microfósseis da Formação Gunflint, Canadá, Formação Draken, Noruega, e estruturas controversas descritas como bactérias fósseis das Formações Hoogenoeg e Kromberg de Barberton Greenstone Belt, África do Sul. Os microfósseis foram imageados em 3D com resolução micrométrica e contraste quantitativo por densidade eletrônica, o que possibilitou a quantificação da densidade das estruturas. As imagens tomográficas forneceram informação sobre a morfologia e composição geoquímica dos espécimes em nano-escala e dentro de um contexto de micro-escala. Os dados morfológicos permitiram distinguir a distribuição 3D de querogênio, os quais revelaram um novo padrão de preservação e traços de alterações tafonômicas para espécimes da Formação Gunflint, e detalhes de organização ultra-estrutural preservados em paredes celulares de espécime da Formação Draken. A quantificação de densidade forneceu evidências complementares, como a discriminação do estado de maturação do querogênio e identificação de minerais, fornecendo também uma visão da história tafonômica dos espécimes. Baseados nos critérios de biogenicidade em nanoescala, não foi possível atestar a biogenicidade das estruturas de Barberton Greenstone Belt, mas novas possíveis interpretações de origem biológica e abiótica para essas estruturas foram levantadas. Os resultados obtidos fornecem avanços significativos na compreensão de micro-organismos fósseis e adiciona uma importante contribuição para a investigação da biogenicidade através de uma robusta combinação de informação morfológica e geoquímica em 3D.

Palavras-chave: Biogenicidade. Microfósseis pré-cambrianos. Tomografia pticográfica de Raios X. Paleobiologia.

LIST OF FIGURES

LIST OF TABLES

LIST OF ABREVIATIONS AND ACRONYMS

BGB	Barberton Greenstone Belt
CT	Computed Tomography
EDS	Energy Dispersive Spectroscopy
EPS	Extracellular Polymeric Substance
Fm	Formation
Ga	*giga-annum* (billion year)
Ma	*mega-annum* (million year)
NASA	National Aeronautics and Space Administration
PXCT	ptychographic X-ray computed tomography
SEM	Scanning Electron Microscopy
TEM	Transmission Electron Microscopy
VLM	Visible Light Microscopy

LIST OF SYMBOLS

A	**molar mass**
N_A	**Avogrado’s number**
μm	**micrometer**
nm	**nanometer**
Z	**number of electrons**

CONTENTS

1 INTRODUCTION

The origin of life on Earth is one of the most complex and intriguing interrogations of science. Questions like *how*, *where* and *when* life appeared in our planet have been the focus of several fields of research, which try to combine interdisciplinary efforts to obtain complementary clues about the emergence and evolution of the earliest life forms on Earth.

Paleobiology is a scientific field which seeks to decode the biosphere of past Earth based in its traces preserved in the geological record. It evolved from the classical paleontology, which was focused on identifying the nature and affinity of fossils and using them for contextualization of the rocks. With the conceptual advances of areas as evolution and paleoecology, the field of paleobiology started to emerge by integrating concepts from phylogenetic systematics, geochemistry, taphonomy[1], paleobiogeography, among others, while novel fossil discoveries also changed the paradigms in the comprehension of the history of life on Earth. (1) Over the last decades, technological developments and the exploration of novel and quantitative analytical methods from different fields yielded greater improvements and robustness to the paleobiological discoveries. This interdisciplinary effort that combines different areas of knowledge for developing methodologies, preferentially non-destructive, for the assessment of paleobiological questions is called paleometry. (2-3)

Paleometry also constitutes a converging point for the fields of paleobiology and astrobiology. As astrobiology seeks to understand the origin and evolution of life in the Universe, the development of methods for the detection of traces of early life (on Earth or other planets), for attesting their biogenicity and for their contextualization within their paleoenvironment constitutes some problems and interests which are also shared with paleobiology. (2,4)

---

[1] Taphonomy is the study of the fossilization process which occur from the death of the organism to its discovery as a fossil. (1)

This work was conceptualized in the context of above-mentioned questions and with the aim of exploring synchrotron-based X-ray imaging techniques for contributing to these discussions. The use of synchrotron X-ray approaches within paleometry has allowed great advances in several branches of paleobiology over the last two decades. Important results of 3D imaging of exceptionally-preserved fossils and geochemical characterizations of preserved elements and biomolecules have deeply extended our knowledge about the early life and its preservation in the fossil record, and consolidated paleometry within both synchrotron and paleobiology laboratories (Figure 1).

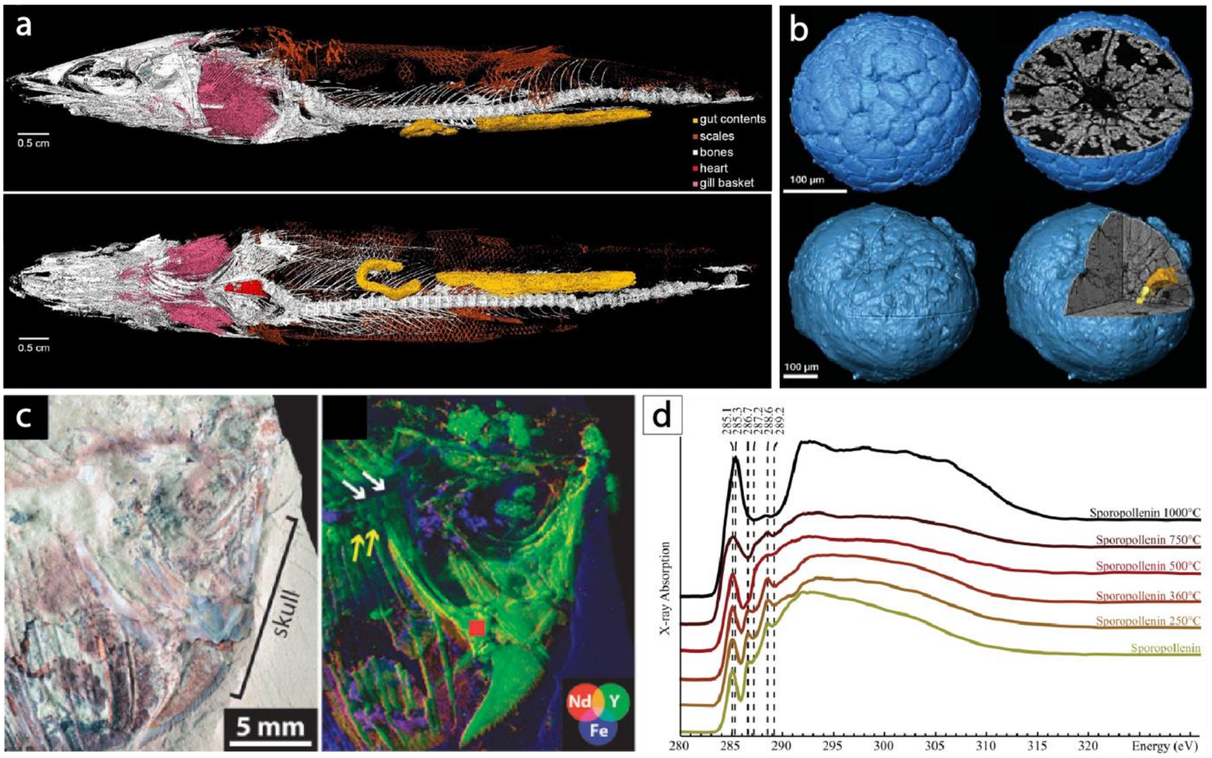

Figure 1 - Examples of paleometry works using synchrotron approaches. **a,** Fossilized tissues revealed with synchrotron phase-contrast micro-CT from a ~110 Ma exceptionally well-preserved 3D fossil fish from the Santana Formation, Araripe Basin, Brazil. Several soft tissues were identified, including the first described fossilized heart. (8) **b,** Synchrotron micro-CT reconstruction of the earliest animal embryos from the Lower Cambrian (~ 540 Ma) Kuanchuanpu Formation, China.(5) **c,** Visualization of anatomic details of a Cretaceous (~ 95 Ma) fish from Marocco exposed by elemental analysis by synchrotron X-ray fluorescence. The elemental map revealed features invisible by naked eye and provided information on the fossilization processes. (6) **d,** Evaluation of the thermal degradation of the biopolymer sporopollenin using synchrotron X-ray Absorption Spectroscopy. The absorption spectra of carbon was measured after different heat-treatments and showed the molecular evolution of the organics. (7)

Source: Adapted from MALDANIS et al. (8); DONOUGHUE et al. (5); GUERIAU et al. (6) ; BERNARD. et al. (7)

Our interest for the development of this work was on exploring the novel approaches in X-ray imaging in the assessment of fossilized microorganisms, the so-called microfossils.

For more than half of the approximately 4.6 Ga[2] of terrestrial history, all the life present on the planet was restricted to microscopic forms. (9) Microorganisms remain as the most diverse and numerous forms of life on Earth until present-day times. These characteristics, along with their widespread distribution in different environments, from the most habitable to the most extreme ones, makes them also potential analogues for the forms of life to be searched on other worlds (see Domagal-Goldman et al. for a review (10). The study of fossilized traces of microbial life offers not only valuable insights into the early chemistry, morphology, mineralogy and the paleoenvironmental conditions which sustained the presence of life on Earth and its preservation on deep-time, but also provide us with a basis of the types of fossil biosignatures which could be searched on other rocky planets, like Mars. Locating and studying possible traces of past life is a strategic priority of space agencies as NASA and ESA, and the selection of promising paleoenvironments for future return missions is one of the primary objectives of Nasa's Mars 2020 rover. (11-12)

Microbial life could have been potentially present in our planet since liquid water was available, at 4.4 Ga. (13) The so-called "late heavy bombardment" of meteorites, which lasted until about 3.85 Ga, possibly vaporized the oceans and had the potential of sterilizing Earth's surface numerous times (14), although this hypothesis is still controversial. (15) Still, even if present, possible morphological record of these first life forms was lost due to the crust recycling caused by tectonic activity, and even the majority of the remaining Early Archean[3] rocks are deeply altered or metamorphized. There are only two places on our planet so far where it is possible to find exposed, sedimentary and well-preserved Early Archean rocks (~3.5 - 3.3 Ga): the Barberton Greenstone Belt, in eastern South Africa; and the Pilbara craton on Western Australia. These rocks provide a valuable insight into the early life forms that inhabited our planet, their environmental context and the conditions for their existence and preservation

---

[2] *giga-annum* (billion year)

[3] The Archean Eon comprises 4 – 2.5 billion years ago

over time. Therefore, although lacking geological records to obtain a more precise estimation of *"when"* life appeared, the study of the biosignatures preserved in Archean rocks can still provide us means of approaching the *"how"* and "*where"* aspects of the emergence of life on Earth.

The exploration of different analytical and imaging techniques has also yield important advanced in micropaleontology over the last decades (see Wacey et al. 2017 for a review). Although these constitute challenging materials to be analyzed, synchrotron-based approaches are now reaching sub-micrometric spatial resolutions (17), detection of trace levels of elements (18) and chemical speciation (19–21), which are allowing different and novel aspects of early life to be assessed (Figure 2). These works highlight the importance of exploring the analytical approaches available on different fields and understanding their fundaments and capabilities for attaining important developments in the study of these complex traces of early life.

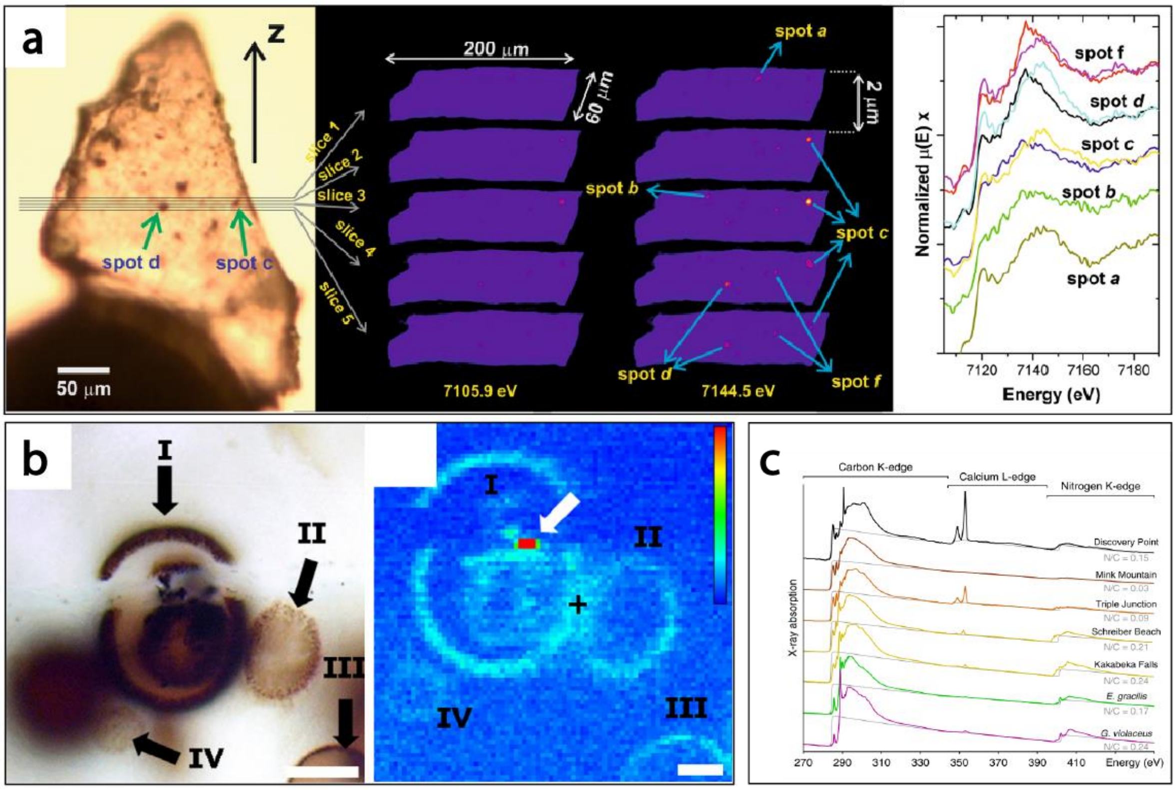

Figure 2 - Examples of studies of Precambrian microfossils with synchrotron approaches. **a,** Analysis of the oxidation state of iron in microfossils from the Gunflint Formation, Schreiber Beach Locality (1.88 Ga) with synchrotron Energy Dispersive X-ray Absorption Spectroscopy (µED-XAS). The spectra were collected in sequential slices over an angular range before the iron K absorption edge (7105.9 eV) and around the pyrite maximum (7144.5 eV) and shows the speciation of this element along the microfossil's extension. (17) **b,** Analysis of a 700-800 My-old microfossil from the Draken Formation using synchrotron X-ray Fluorescence. The fluorescence map obtained at 2500 eV shows the distribution of S within the organic cell wall and in a pyrite grain. (18) Scalebar: 5 µm. **c,** X-ray absorption spectra of Gunflint microfossils from different localities. The spectra comprise the absorption energies of C and N and offers an insight into the degree of molecular preservation of the fossils of this Formation.

Source: Adapted from SANCHEZ et al. (17); LEMELLE et al. (18); ALLEON et al. (19)

This thesis is focused in the study of Precambrian[4] microfossils, which comprise the earliest evidences of life on Earth. One of the main challenges in early-Earth paleobiology relies on how to identify and attest the biological origin of a given structure found in the geological record. This complex investigation requires several aspects to be covered, from morphology, ultrastructure, and geochemical composition up to taphonomy and paleoecology.

For addressing these questions, we explore the potential of the imaging approach called ptychographic X-ray computed tomography (PXCT). This imaging method provides 3D nanometric-resolution and quantitative electron-density contrast for specimens of tens of microns, covering a gap of size and resolution between electron microscopies and microtomography.

This thesis is divided in the following structure:

Section 1.1 presents an historical overview of the study of microfossils. Section 1.2 describes the theoretical basis of visible light and X-ray microscopies and how the different interactions of X-ray with matter affects the information obtained for geobiological materials.

Section 2 outlines the main objectives of this work.

Section 3 describes the experimental approach. The description of the fossils analyzed and their geological provenance, sample preparation, data acquisition and treatment are discussed in this section.

Section 4 describes the results and discuss their implication on morphology, taphonomy, paleoecology and biogenicity.

1.1 THE STUDY OF PRECAMBRIAN MICROFOSSILS

One primary step for the study of Precambrian records of life consists in defining and understanding what kind of traces can be expected to be preserved in the geological record. A term which is commonly applied for referring to signals of life from early Earth or beyond is “biosignature”. There is a variety of forms of biosignatures that can be

---

[4] Informal unit of geologic time which spans from Earth formation (~4.6 Ga) to the beginning of Cambrian Period (~541 Ma.), comprising the Hadean, Archean and Proterozoic eons.

found in the geological record and understanding their origin, modes of preservation and defining methods for their unequivocal identification is of prime importance for guiding the evaluation of the records of early life on Earth.

Chemical biosignatures correspond to chemical signals characteristics of biological metabolisms, such as the presence of some organic molecules (*e.g* products of the degradation of lipids and proteins), biominerals, distinctive isotopic fractionations of some bio-elements, such as carbon, sulfur, nitrogen and iron, or distinctive ratio of bio-essential elements. (22) Elemental and isotopic biosignatures are the more persistent over deep time in comparison with morphological ones. Isotopes, for example, have been used as evidences of life prior to 3.7 Ga. (23-24), yet, their biogenicity have been focus of controversy. (25) Moreover, chemical signs of microbial life are more difficult to be detected in comparison with morphologically preserved ones (Figure 3).

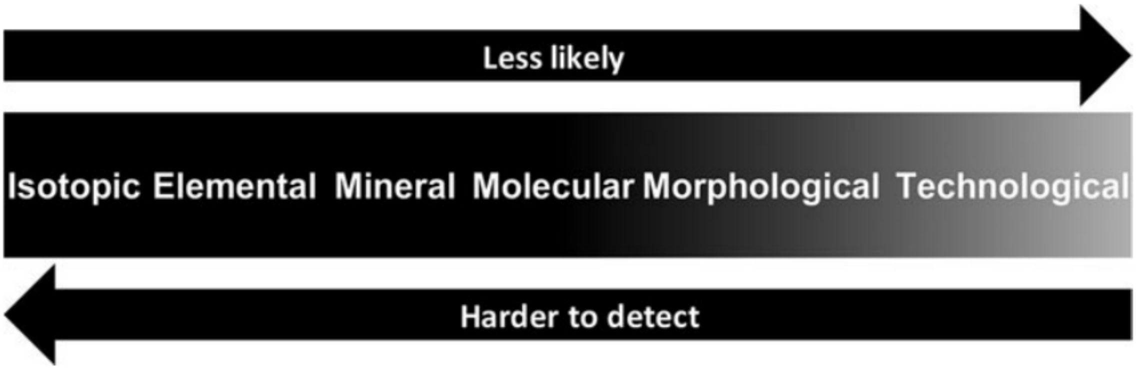

Figure 3 - Graphical representation of the relationship between the different types of biosignatures, their probability of preservation and the feasibility of detection.
Source: GOMES et al. (2)

Morphological biosignatures comprise cells and cellular products, microbial mats and bioconstructions. In the case of Archean life, composed by primitive prokaryotic cells lacking any hard parts, only soft materials as cell walls, membranes, sheaths and associated secreted substances can be present. The extracellular polymeric substance (EPS) secreted by microorganisms for protection, adherence and micro-environmental control has a good chance of preservation because it contains functional groups which favors the binding and precipitation of minerals. (22) These properties lead to the preservation of biomineralized structures such as microbial mats and stromatolites, or bio-induced ones, as the *Microbially Induced Sedimentary Structures* (MISS) (26) (Figure 4).

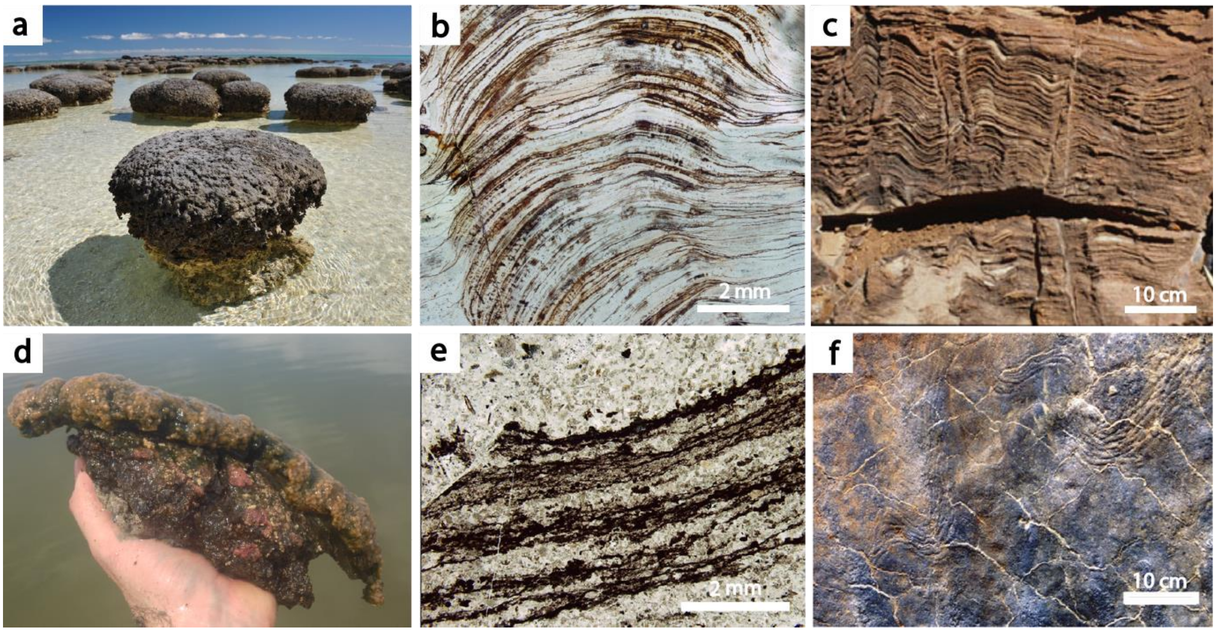

Figure 4 - Examples of morphological biosignatures including some of the oldest records of life on Earth. **a,** Extant stromatolite from Shark Bay, Australia **b,** Petrographic micrography of a pseudocolumnar stromatolite fossil from the Gunflint Formation, Mink Mountain locality (1.88 Ga), Canada. **c,** Early Archean coniform-pseudocolumnar stromatolite from the Strelley Pool Formation (3.43 Ga). (27) **d,** extant microbial mat from Lagoa Vermelha, Rio de Janeiro, Brazil. **e,** Fossil multi-laminar microbial mat from the Middle Marker horizon (3.47 Ga) of the Hooggenoeg Formation, South Africa. (28) **f,** Microbially Induced Sedimentary Structure (MISS) from the Moodies Group of the Barberton Greenstone Belt (3.2 Ga), South Africa. (29)

Source: **a,b,d** By the author; **c, e, f**, Adapted from WESTALL et al. (27);HICKIMAN-LEWIS et al. (28); NOFFKE (29)

Cells and cellular traces preserved in the geological record are called microfossils and, once their biological origin is confirmed, represent direct evidences of early microbial life. Depending on their degree of preservation, these structures can provide insights into the morphology, composition, evolution, and even ecological interactions of ancient life forms. Their taphonomic alterations can additionally provide us means of understanding the physico-chemical conditions which allowed the preservation of such delicate structures from deep-time. Moreover, due to the difficulties on identifying and interpreting chemical biosignatures and even other indirect morphological biosignatures, *bona fide*[5] microfossils have the potential to represent robust and direct evidences of fossilized life on the oldest terrestrial rocks or even in material from meteorites or returned from other planets. (30)

---

[5] Latin term used to express “genuine”

A benchmark for the study of Precambrian microfossils was the description of an exceptionally well preserved biota (Figure 5) in rocks from the approximately 1.9 Ga Gunflint Formation in the Lake Superior region of Canada by Barghoorn and Tyler 1965. (31) Their abundance, diversity, complexity and state of preservation resulted in a widespread acceptance by the scientific community, which, at that time, still had some skepticism about the existence and preservation of Precambrian life. The Gunflint biota plays a critical role in the understanding of the Precambrian life and its paleoenvironment, and due to their universally accepted biogenicity, it also became reference for the establishment of biogenicity criteria, for evaluating the putative biological origin of older, less preserved structures, and as ideal samples for the exploration of capabilities of novel imaging techniques (Figure 2a,c). (17,19-20,32-33)

Although the preservation of microorganisms has been described to occur also as compressions in fine-grained sediments (34), or by minerals such as pyrite (35), silica is considered the ideal medium for the preservation of these microstructures. Archean oceans were saturated in silica, originated from a high input of hydrothermal fluids and dissolution of volcanic rocks, favoring a rapid silicification of cells. The small crystalline matrix of silica also allows the preservation of fine-scale detail, which, associated to its resistance to dissolution and weathering, give rise to the most exquisite three-dimensional preservations, such as the specimens of the Gunflint chert[6]. (37-38)

---

[6] Sedimentary rock composed of quartz (silica). The microcrystalline and resistant nature of this rock are favorable for the preservation of microfossils.

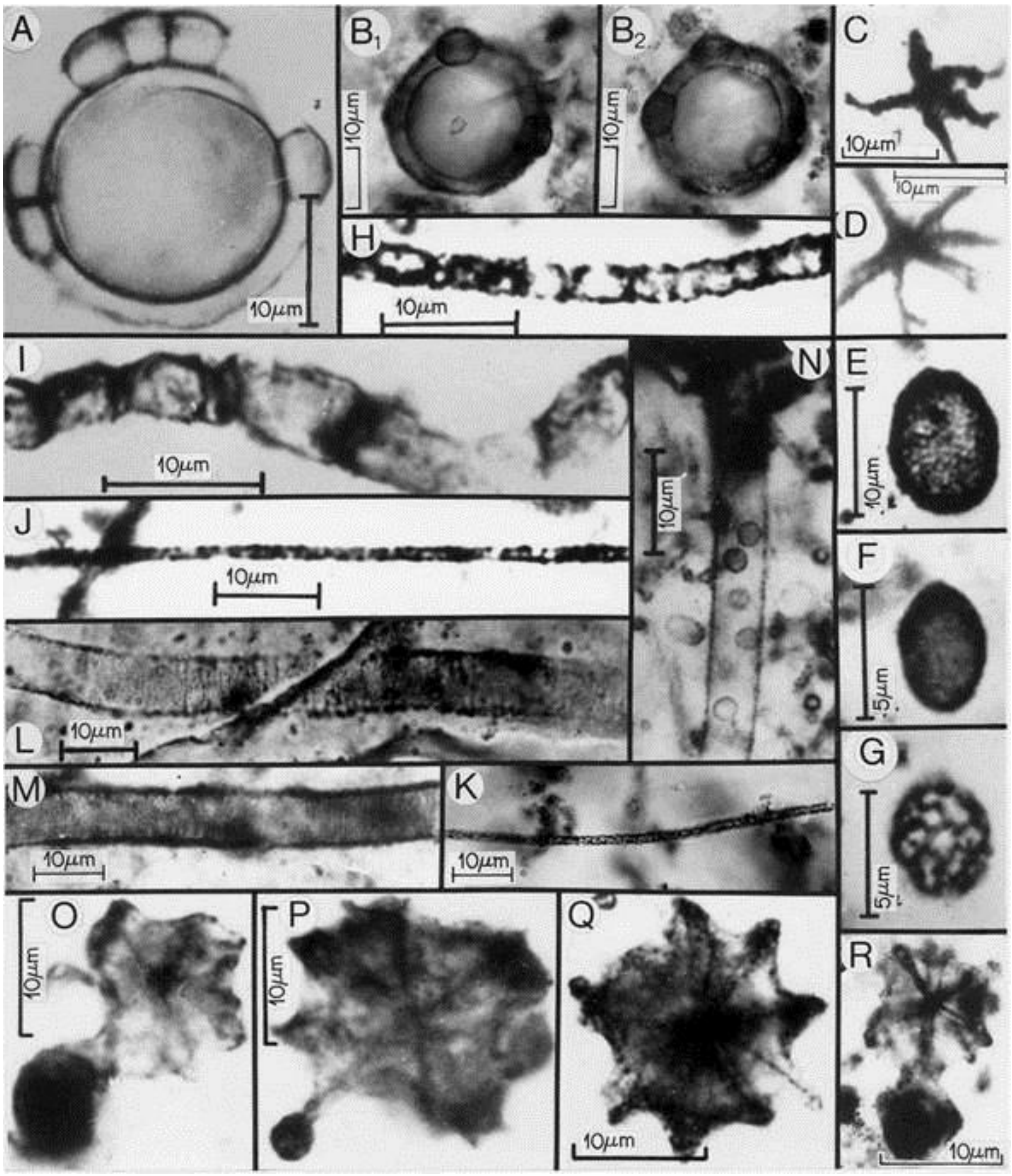

Figure 5 - Microfossils from the Gunflint Formation described by Barghoorn and Tyler in 1965. (31) The exceptional state o preservation and diversity make this assemblage a benchmark in the study of microfossils and a reference for assessments of biogenicity.
Source: SCHOPF (38)

The fossilization occurs when mineral ions interacts with functional groups of the cell wall or the EPS and triggers the mineral polymerization, forming a crust that can sometimes encapsulate the organic remnants. (35-36) The resulting structure can be hardly morphologically distinguishable from a range of artefacts generated by abiotic geological processes (40) or from condensation of carbon around crystalline nuclei or volcanic glass. (41)

The difficulty on the discrimination of biotic and abiotic features emphasizes the need of precautious prerogatives and of robust and complementary evidences when claiming the description of a putative Precambrian microbe. This requires a multi-scalar approach, which starts with a careful characterization of the geological context at the field, from the kilometer to millimeter scale, followed by a fine microscopic evaluation for inspecting both morphological and geochemical contexts at the level of the preserved structures. These analyses should also focus on evaluating if the paleoenvironmental context was favorable to the existence of microorganisms, if the preservation environment supports their preservation, and if there are evidences of a syngenetic[7] origin with the rock, discarding later contaminations. Finally, any possible abiotic explanation for the formation of the given structure should be considered during the evaluation of its biogenicity.

Nevertheless, attesting the biogenicity of a putative microfossil is a task particularly challenging when regarding Precambrian structures. The first reason for this difficulty is that the earliest life forms are expected to be similar to the modern prokaryotic microorganisms. Those consist of cells of minute size, usually 1-2 μm in diameter and up to ~10 μm in length, and a simple morphology, being mostly spherical, rod shaped or spiral and lacking ornamentations. From the components that compose these cells, the cell wall has the best chance of preservation due to its composition of peptidoglycan and natural resistance against external forces. (22)

Since the beginning of the studies of Precambrian microfossils, the need for establishing methods or criteria for demonstrating the biogenicity of a microfossil-like object has been repeatedly addressed. (42-43)

The difficulty on studying the earliest microfossils on Earth is well illustrated by the contentious debate surrounding the "Apex chert[8] structures". Schopf 1993 (46) described a diverse assemblage of microfossils in 3.46 Ga rocks from the Apex chert of the Pilbara craton, Western Australia (Figure 6a). Besides claiming to have described the oldest known microfossils on Earth, several specimens were classified as photoautotrophs due to similarities with living cyanobacteria. This implied in a remarkably rapid diversification of microbial life since its origin, especially when

---

[7] Contemporaneous with the host rock

[8] sedimentary rock composed of quartz (silica). The microcrystalline and resistant nature of this rock are favorable for the preservation of microfossils.

considering that the late heavy bombardment of meteorites with sterilizing potentials finished at approximately 3.8 Ga. (14) These structures were further revisited by Brasier et al. 2002 (25) who reinterpreted them as "pseudofossils" or microfossil-like artefacts formed from amorphous graphite in the context of a hydrothermal vein. The debate continued with several works questioning and supporting the biogenicity of these structures (Figure 6) (44-45,47-48), and consequently stimulated the exploration of novel imaging and analytical techniques as means of supporting or contesting biogenic characters. (44,49–51) Although the controversy still remains in some degree, several of these techniques became part of routine approaches in the study of microfossils, stimulating significative advances in the field of geobiology.

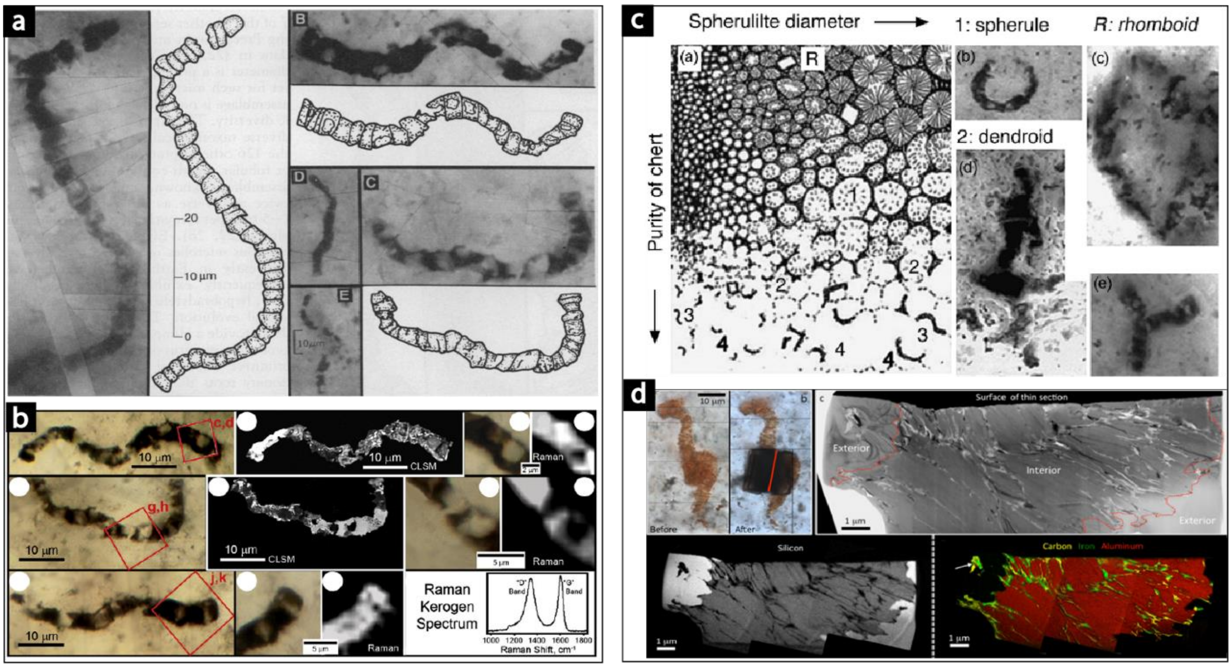

Figure 6 - Illustration of the Apex Chert debate. Left panel: images of the structures interpreted as microfossils in the Apex Chert. Right panel: reassessments of these structures proposing abiotic origins. **a,** Petrographic photomicrographs of the Apex Chert structures. (46) **b,** Petrographic photomicrographs, confocal laser scanning microscopy (CLSM) and Raman images of carbonaceous specimens from the Apex Chert. The 3D morphology, presence of cellular compartment and kerogenous composition were used for supporting their biogenicity. (44) **c,** Scheme for explaining an abiotic origin for the Apex structures. Carbonaceous material was redistributed to the margins of crystals during recrystallization of the chert. This hypothesis supported by observation of different morphologies, some of which are inconsistent with biology. (45) **d,** Transmission Electron Microscopy analysis of Apex Chert structures interpreted as pseudofossils. Elemental maps show that carbon is distributed along quartz-aluminosilicates boundaries and do not present cell-like distribution.

Source: Adapted from SCHOPF (46); SCHOPF et al. (44); BRASIER et al. (45); BRASIER et al. (49)

Another iconic example for the challenge of biogenicity was the description of fossil microbes in cracks of a Martian meteorite found in Antarctica. (30) The structures of few hundreds of nanometers in size were interpreted as nanobacteria, and were publicly announced as the first evidence of life beyond Earth. (52) These claims inflamed discussions in the scientific community, and the structures were further reinterpreted as mineralogical artefacts. (53) This event brought to light the difficulty on distinguishing morphological fossils from structures produced non-biologically and highlighted the necessity of developing rigorous approaches and novel analytical methods for the attesting the biogenicity of morphological biosignatures in the context of both paleobiology and astrobiology.

These famous discussions illustrate the importance of defining biogenicity criteria used for the study of early life traces, particularly when regarding Precambrian structures.

A compilation of these criteria was made by Wacey 2009. (22) Based on this review, the criteria with strong reliance on imaging approaches for their evaluation, and therefore relevant for the purpose of this thesis, are listed below:

Set of proposed biogenicity criteria, extracted and adapted from Wacey 2009 (22):

a) Structures should exhibit biological morphology that can be related to extant cells, sheaths, traces of activity or waste products. Ideally life cycle variants should be identifiable (reproductive stages), comparable to that found in morphologically similar modern or fossil microorganisms.
b) Structures should occur within a geological context that is plausible for life; i.e., at temperatures and pressures that extant organisms are known to survive.
c) Structures should fit within a plausible evolutionary context.
d) Microfossils should ideally be composed of kerogenous[9] carbon. If mineralized this should be a result of microbially mediated precipitation.

---

[9] Kerogen is the insoluble organic constituent of sedimentary rocks(111).

e) Fossilized cells should be hollow. Since cell walls and sheaths are the most probable features to be preserved while cellular constituents are rarely. Besides, mineral artefacts are unlikely to be hollow.
f) Microfossils should have signals of taphonomic degradation, such as collapsed cells, folding of films, fracturing.
g) The object must exceed the minimum size for independently viable cells (~0.25 μm diameter).
h) Microfossils should be demonstrably dissimilar from potentially co-existing non-biological organic bodies (e.g., self-organizing spherulitic structures), and should occupy a restricted biological morphospace.
i) Structures should be abundant and ideally occur in a multi-component assemblage.
j) Following from (i), they should ideally show colonial/community behavior.
k) Following from (j), a preferred orientation indicating a role in the formation of biofabrics would be an additional bonus criterion.

The fact that several biogenicity criteria rely on information obtained using some type of microscopy implies that the evaluation of putative microfossils is based, and therefore limited, by aspects inherent of the applied imaging method. Understanding the physical principles and concepts behind an image generated by different microscopies is thus of fundamental importance for achieving a better understanding of the information obtained and also for allowing the exploration of novel methods for overcoming the existing limitations.

The fossilization processes also generate an important limitation in the study of microfossils, which is caused by their geochemical composition. The mineralization of microorganisms substitutes or dilutes considerably the original organic components, producing structures with densities very similar to the surrounding medium, and limiting the concentration of bio-elements to trace levels. This has important implications in the generation of contrast for most high-resolution imaging techniques, which commonly rely in density variations or chemical maps for the generation of images. This topic will be discussed in detail in the section 1.2.

1.1.1 RECENT ADVANCES IN HIGH RESOLUTION IMAGING OF PRECAMBRIAN MICROFOSSILS

As previously explained, the search for early life traces requires a multi-scale analysis which starts at the field with the full geological characterization of the outcrop and is continued by laboratory petrographic analysis under a visible light microscope. This latter represents the basic method of survey for the discovery and description of microfossils and is explained in detail in section 1.2.1

The development and application of novel imaging techniques in the study of Precambrian material has allowed significant advances over the last decades in the reconstruction of the complexity and context of Earth's ancient biosphere.

Some general properties of any imaging method that are important to be mentioned in the context of Precambrian paleobiology are: *spatial resolution*, *contrast* and *number of represented dimensions (i.e. 2D, 3D).*

Contrast can be defined as the difference in intensity between two adjacent areas. (46-47) This is a very important aspect to be discussed because the contrast obtained by different methods depends on the physical phenomena in which they are based and also on the nature of the analyzed material. Therefore, the information that generates contrast on different microscopies can be understood based in the principles of interaction of the probing radiation with matter.

Since microfossils are three-dimensional structures distributed across a range of depth within the rock samples, the use 3D imaging techniques encounter obvious advantages over the 2D ones. These can be of vital importance in the study of controversial structures, since the observation of three-dimensional features in 2D slices or projections can hinder overlapped features or be restricted to deceptive planes, thus leading to misconceptions in their interpretation.

Resolution is the concept more usually considered during the choice of an imaging method and refers to the capacity of distinguishing two separate features in a specimen. (55) The minute size of Precambrian specimens necessitates high-spatial resolution images for their investigation and assessment of biogenicity. Limitations in resolution can hinder the proper evaluation of minute specimens and even lead to erroneous interpretations of biogenic features. As an example, Brasier et al. 2015 evaluated the biogenicity of putative Apex chert microfossils, among others, using high-resolution approaches of FIB-TEM and FIB-SEM (Figure 6b). The authors affirm that the kerogenous structures alleged to resemble cellular compartments and which are pointed as one of the major biogenic characters of these specimens were misinterpreted because of the low-resolution methods applied (*i.e.* visible light microscopy and micro-Raman). The nanometric resolution and 3D information obtained revealed lengths and widths ratios inconsistent with a biological origin. This information could not be resolved by traditional imaging methods, demonstrating the importance of taking the study of biogenic characters to the nanoscale.

Electron microscopies represent today the highest-resolution methods commonly applied in the study of microfossils and they have been extensively explored over the last decades. The main limitation of electrons for imaging approaches is their low-penetration depth. For imaging based in Scanning Electron Microscopy (SEM), the electrons provide information related to few tens of nanometers in depth, consequently only of the surface of the object. The contrast obtained is usually based on topographic information (secondary electrons) or atomic number (backscattered electrons). Additional elemental analysis can be performed with energy dispersive spectroscopy (EDS) detectors and crystallographic mappings with a backscattered diffraction detector. SEM is commonly applied in microfossils after etching the rocks with acid treatments for revealing the inner structures. (56) This procedure, however, is destructive and can generate artefacts. Transmission Electron Microscopy (TEM) is a modality of electron microscopy which allows resolutions in the order of Ångströms to be achieved. (54) This transmission, however, is only possible for nanometric thin (< 100 nm) specimens, therefore enabling only a very thin section of a micrometric-size organism to be studied at each time and requiring a complex sample preparation which is invasive and destructive. The study of microfossils with this approach was optimized by the precise extraction of slices using a focused ion beam (FIB) coupled to a SEM (FIB-SEM). (57) This approach has been further extended to 3D by combining sequential milling with concurrent EDS-SEM imaging. (50-51) Wacey et al. 2012 first combined FIB-TEM and FIB-SEM for studying Precambrian microfossils and demonstrated their potential for assessing chemistry, ultrastructure, taphonomy and biogenicity of these structures. In summary, the main limitations of electron microscopies are: the small sampling area caused by the low penetrability of electrons and for the FIB-SEM, the high cost, which limits the sampling volume and resolution (essentially defined by the thickness of the slice plus gap between consecutive images, in average >100 nm (16)), and destructive nature of this approach.

X-rays can have wavelengths in the order of atomic distances, therefore also configuring a probing radiation with potential to achieve nanometric spatial resolutions. When compared to electrons, the high-penetrability of this electromagnetic radiation can allow larger volumes to be sampled, fulfilling the gap of *sampling size x resolution* which is present between the electron and visible light microscopies. With the development of the high-brilliance synchrotron sources with nanoprobes, imaging techniques such as scanning transmission X-ray microscopy, X-ray absorption spectroscopy and X-ray fluorescence have been more explored in paleobiology, with some applications also to Precambrian samples. (16–20,60)

The remarkable capability of X-rays for providing 3D information of the specimens, however, has not yet been explored at the nanoscale for Precambrian microfossils. To our knowledge, only one work so far proposed to evaluate the capability of absorption-contrast microtomography for the investigation of Precambrian microfossils (Figure 7). (61) The authors concluded that this method, while providing an overview of petrological context, was limited for the investigation of microfossils.

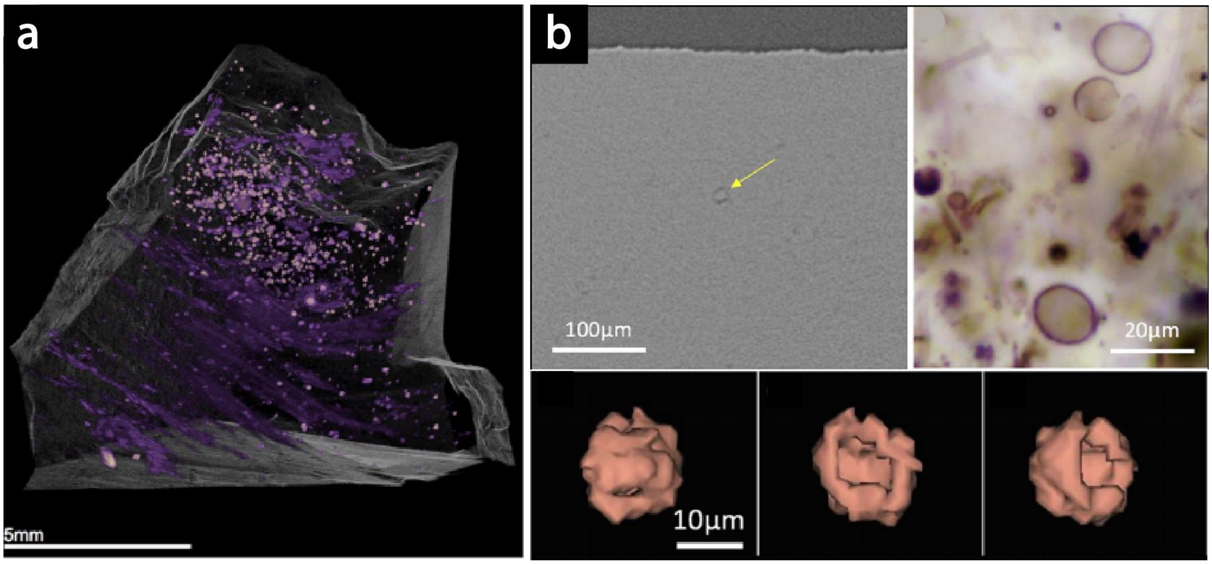

Figure 7 - Results obtained with absorption contrast micro-CT for samples of the Gunflint Formation. a, 3D rendering of a stromatolite from the Mink Mountain locality (Figure 4b). The high-density iron oxide layers and metalliferous crystals can be observed within the silica matrix. b, Results for samples from the Schreiber Beach locality. Some spheroidal objects were interpreted as microfossils, but the low contrast and resolution of the approach hindered detailed investigation.

Source: Adapted from HICKMAN-LEWIS et al. (61)

For being able to explore these capabilities and for defining the approaches with most potential to contribute to the study of Precambrian microfossils, we need to understand the principles of microscopy and X-ray imaging. The following sections describe the fundamentals of microscopy for visible light and X-rays, including the principles of microscopic tomography, and the novel imaging methods of *lensless* x-ray microscopy and Ptychography.

1.2 FUNDAMENTALS OF MICROSCOPIC IMAGING

1.2.1 VISIBLE LIGHT MICROSCOPY

The basic approach for inspecting rocks which might contain microfossils starts with petrographic analysis using visible-light microscopes (VLM), commonly called optical microscopes. For this approach, rocks are prepared in thin sections, usually attached to glass slides, and polished up to tens of microns until they get sufficiently transparent for the transmission of light. Polarizers and additional optics or sources of light can be used for additional geological characterizations, taking in account the refractive and optical properties of some minerals. Due to the low cost, accessibility and potential to perform exploratory investigations in a large number of samples, petrography using VLM consists in the fundamental approach for the detection and description of microfossils.

The principles of the VLM described in this section are based in Murphy and Davidson 2012.

The image obtained in a VLM is basically a combination of the absorption, refraction and diffraction of the light incident on the object. As any type of microscopy, the capability of distinguishing a given object or feature relies on two properties: contrast and resolution.

The basic principle of imaging formation by a microscope was defined by Ernst Abbe in 1873. The diffraction of light by an object is the principal physical process related the formation of the image in the light microscope. Waves diffracted by features of the object in the same order of magnitude of the wavelength of the light will propagate towards the objective lens. The smaller the diffracting feature, the wider the angle of diffraction. Part of these diffracted light will be collected by the objective lens, depending on its numerical aperture (NA). The larger the NA, the higher diffraction orders are collected, therefore higher resolution can be achieved. The objective directs the diffracted waves towards the image plane. Interferences between the diffracted waves will generate a diffraction pattern at the back focal plane of the objective. This corresponds mathematically, to the Fourier Transform (FT) of the object. Therefore, to form the image, the interference of the diffracted and transmitted light after the back focal plane corresponds mathematically to an inverse FT of the object's diffraction pattern (Figure 8).

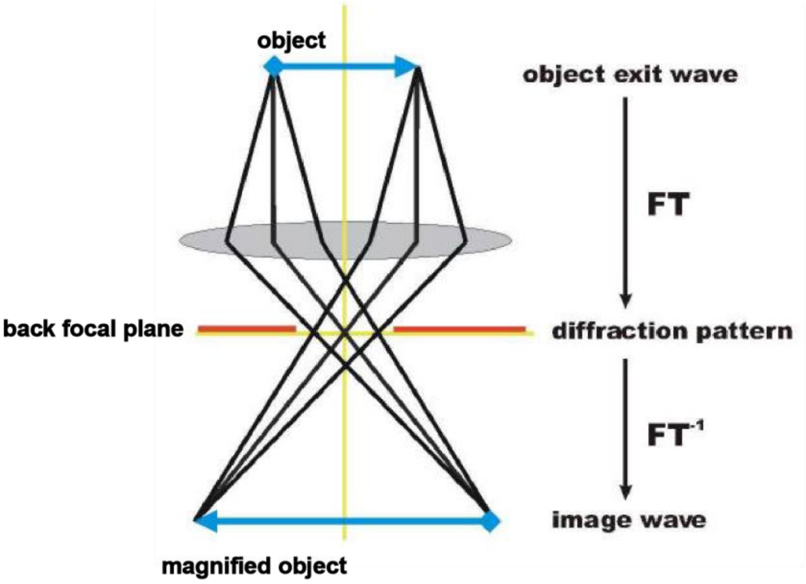

Figure 8 - Diagram of the image formation on a microscope. The light scattered by the object reaches the back focal plane as a diffraction pattern or Fourier transform (FT) of the object. The second lens mathematically performs an inverse FT and reconstructs the final image.
Source: Adapted from: ETH ZÜRICH. (62)

According to the Rayleigh criterion, the resolution d of a microscope is limited by the numerical aperture of the lens NA and by the wavelength λ of the probing radiation, according to the equation:

$$d > \frac{0.61\lambda}{NA} \tag{1}$$

In the case of visible light, the wavelength λ ranges from 400 to 750 nm.

The contrast in VLM is based in a combination of the intensity of the light and its wavelengths (colors). If the intensity of the object or feature is similar to its background or surrounding materials, they are not distinguishable. The intensity, in turn, is proportional to the amplitude A of the electromagnetic radiation such that:

$$I \propto A^2 \tag{2}$$

An object which absorbs, and consequently affects the amplitude of the incoming light is called *amplitude object.* In contrast, some materials (*e.g.* extant cells) are transparent to visible light and cannot be observed in a conventional bight-field microscopy. The changes in the phase of the light waves caused by these objects can be converted in amplitude differences with the approach called phase-contrast microscopy, allowing their observation.

Kerogenous microfossils can be observed by this approach due to the commonly brownish aspect of this material that produces contrast. Still, the contrast will depend on the composition of the surrounding matrix (*i.e.* transparent or presenting a different intensity/color).

The absorption and scattering coefficients which governs these properties for a given material are dependent on the wavelength of the probing radiation and will affect the information that can be obtained by the different microscopies. This subject is particularly relevant for microscopies based on X-rays and it will be discussed in detail in the following sections.

1.2.2 X-RAY MICROSCOPY

1.2.2.1 INTRODUCTION TO X-RAY IMAGING

X-rays were first produced and detected in 1896 by Wilhelm Röntgen who also demonstrated their high penetrability to several materials and produced the first and iconic radiographic image of his wife’s hand and wedding ring (Figure 9). The discovery of this invisible radiation, named due to its unknown nature, was acknowledged with the Nobel of physics in 1901. (63)

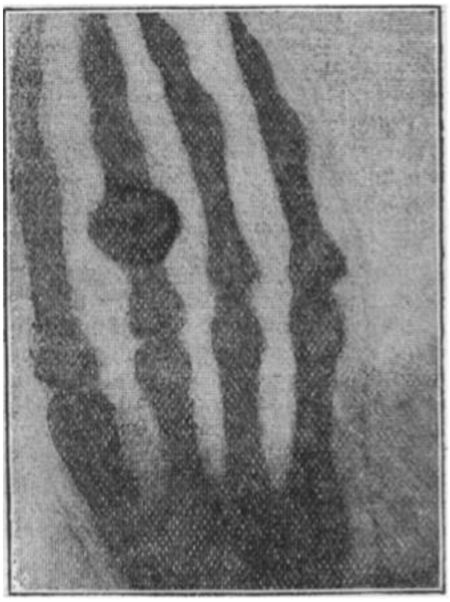

Figure 9 - First radiographic image recorded by Röntgen showing the bones and ring of his wife's hand.
Source: RÖNTGEN (64)

Since their discovery, X-rays have been largely applied on different fields of science. Among several applications, the use of X-rays for imaging is the most well-known, particularly for its large utility, prominently in security and medicine.

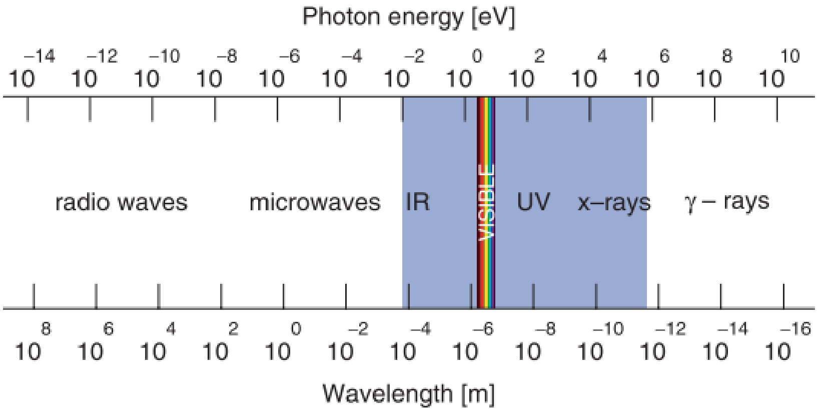

Figure 10 - The electromagnetic spectrum. The region marked in blue corresponds to the range of energies covered by synchrotrons sources.
Source: WILLMOTT (63)

Similar to visible light, the formation of image in X-ray microscopy depends on the type of interaction with the object. X-rays have considerably higher energy (or shorter wavelength) than visible light (Figure 10). This energy is higher than the binding energies of most electrons, except the tightly bound, core ones. Consequently, X-ray radiation is weakly absorbed and can be transmitted through materials which are opaque to visible light, allowing the interior of objects to be investigated. Still, the same phenomena described for electromagnetic radiation at the visible spectrum can also be observed in the X-rays regime, *e.g.* absorption, refraction, reflection, scattering and transmission.

An object can be defined by means of its complex index of refraction *n,* which describes the response of its electrons to the electromagnetic radiation. This index can be expressed as:

$$n = 1 - \delta + i\,\beta \tag{3}$$

Where δ is the refractive index and β is the absorption index. These terms depend on the energy E of the electromagnetic radiation, such that $\delta \propto E^{-2}$ and $\beta \propto E^{-4}$. They are important for the generation of contrast in X-ray microscopies and will be discussed in detail in the following sections.

1.2.2.2 PRINCIPLES OF TOMOGRAPHIC MICROSCOPY

The physical and mathematical basis described in this sections are based in the texts of Kak and Stanley 1999 (65) and Willmott 2011. (63)

The high penetrability of X-rays for the non-invasive 3D imaging of objects has been largely explored in material, biological and medical sciences in the technique called tomographic microscopy or computed tomography.

The word tomography comes from the Greek word *tomos*, which means “slice” e *grafo*, meaning “image”. Tomography can be generally defined as the generation of a three-dimensional image through the computational transform of several radiographic projections of a specimen obtained at different angles. When the spatial resolution achieved is in the order of microns, this technique receives the name of microtomography or micro-CT.

On this approach, the incident X-rays interacts with the object along its longitudinal section and the transmitted beam is recorded in a bidimensional detector. The detected signal corresponds to the intensity *I* of the radiation after being attenuated by the specimen, which can be described by the Beer-Lambert law as:

$$I = I_0 e^{-\mu z} \tag{4}$$

Where I_0 is the intensity of the incoming radiation, z is the penetration depth and μ is the linear absorption coefficient of the material.

The intensity of the transmitted X-rays can also be described considering the total attenuation along a path $L = M\,\Delta z$, and given by:

$$I = I_0\, e^{-\mu_1 \Delta z}\, e^{-\mu_2 \Delta z}\, e^{-\mu_3 \Delta z} \ldots e^{-\mu_N \Delta z} \tag{5}$$

$$= I_0 \exp\left(\sum_{k=1}^{M} \mu_k\, \Delta z\right) \tag{6}$$

For each pixel of the detector the projection p can be defined as the line integral of the object attenuation along a line L:

$$p = -ln\left(\frac{I}{I_0}\right) = \int_L \mu(\boldsymbol{z}).\, d\boldsymbol{z} \tag{7}$$

This function p is known as the Radon transform of the object μ. This transform is the mathematical basis for reconstructing a given quantity from its projections collected at different angles and was demonstrated theoretically by Johann Radon in 1917.

The tomographic reconstruction for retrieving the 3D distribution of the object consists in the inversion of the Radon transform. This process is based in the so-called "Fourier slice theorem", which states that the 1D Fourier Transform of the projection of a 2D object onto a line is equal to the 1D slice through the center of the 2D Fourier transform of that object (Figure 11).

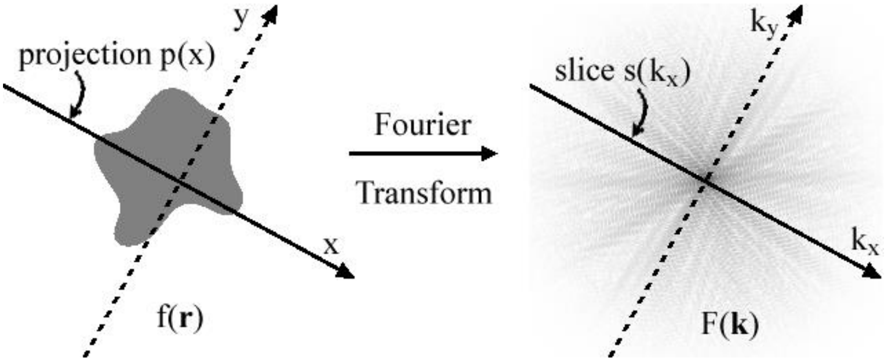

Figure 11 - Graphical representation of the Fourier slice theorem in 2D.
Source: ProjectionSlice.png (66)

These mathematical principles are used by computational algorithms to perform the tomographic reconstructions. The most common class of algorithms is called filtered back projection (FBP), which is based on fast Fourier transform algorithms (FFT) of the projections, filtering the oversampled regions in the frequency domain and then performing a backprojection. This last consist on summing over the image plane the inverse Fourier transforms of the filtered projections (Figure 12).

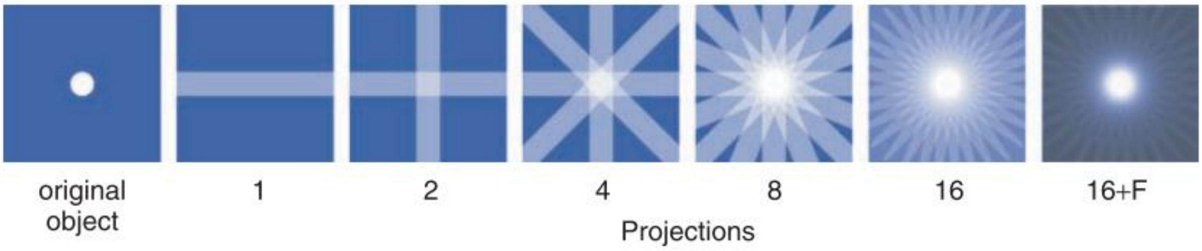

Figure 12 - Graphical illustration of the backprojection process used ion the tomographic reconstruction algorithms FBP. The star-like artefacts observed with the increased number of projections represent the oversamples regions which should be filtered at the frequency domain.
Source: WILLMOTT (63)

1.2.2.3 CONTRAST MODALITIES IN TOMOGRAPHIC MICROSCOPY

The principles of X-ray tomography described in the section 1.2.2.2 are based on the linear absorption coefficient μ, thus constituting a contrast method based in absorption.

The absorption coefficient of a given material is dependent on the atomic number Z of its elements as $\mu \propto Z^4$. Therefore, the absorption tomography presents good contrast for structures composed by materials with distinct densities and high Z numbers.

In geobiological samples, this property can be useful for the identification of porosities or minerals with significatively different densities. Fossilized materials have the original components diluted or substituted by the infiltrating minerals, hence being hardly distinguishable by absorption contrast tomography.

As described by the Equation (4, the complex refractive index n, which describes an object, comprises an absorption index (which relates to μ), but also a refraction index δ, which describes the decrement in velocity of the radiation passing through that medium. Considering two waves initially in phase and only one passing through the specimen, the term δ describes the phase-shift between these waves downstream the specimen. This phase-shift at typical hard X-ray energies can be three orders of magnitude greater than the absorption term and can be used as a contrast modality called phase-contrast.

The detection of the phase shift can be done in (partially) coherent synchrotron X-ray sources by the propagation of the scattered wave, which suffers interference producing diffraction features. This process will be described in detail in the section 1.2.3.2. At the distance known as Fresnel-diffraction regime, the scattered pattern still resembles the object, but presenting an edge enhancement or fringes. These can be used by reconstruction algorithms to obtain the phase maps, such as the single distance retrieval algorithm proposed by Paganin (67), which is largely used for homogeneous materials.

Phase-contrast applied to micro-CT revolutionized the study of fossils by achieving a high contrast even for fossilized structures with low density-contrast. This allowed the non-destructive and non-invasive analysis of internal features, preserved soft-tissues (Figure 1a, b, Figure 13), ultrastructural details of bones and teeth, and innumerable other important findings (8,68–70). This contrast modality clearly emerges as the most promising so far for obtaining information of the cellular features preserved in microfossils.

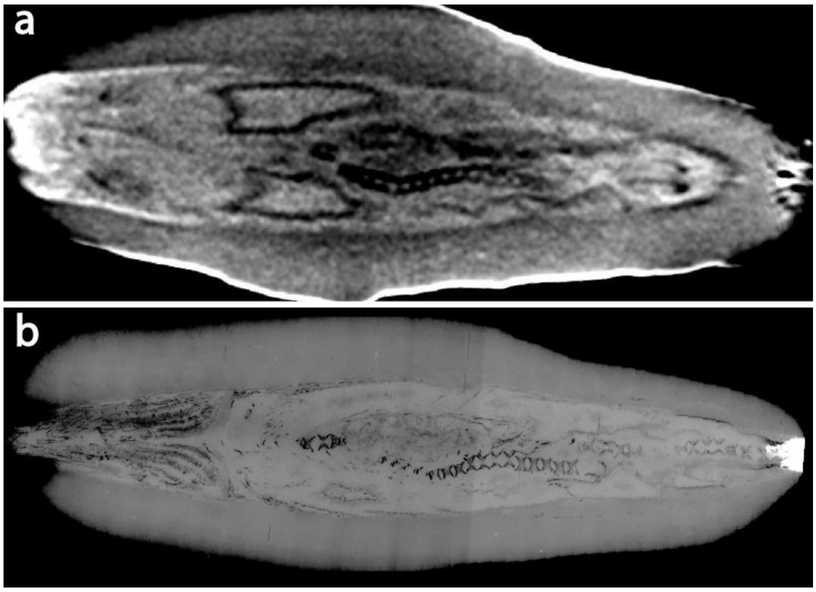

Figure 13 - Comparison of absorption and phase-contrast tomographic images of the same fossil fish. The difference in resolution should not be considered for this discussion. **a,** absorption contrast image showing mainly the bones of the vertebrae column and lateral structures which correspond to different minerals formed by the infiltration of fluids during the specimen degradation. **b,** phase-contrast image showing a vast range of preserved anatomical details from bones and also preserved soft-tissues.

Source: By the author

1.2.3 X-RAY COHERENT DIFFRACTION IMAGING AND PTYCHOGRAPHY

As explained in the section 1.2.2.3, absorption-based X-ray tomography encounters a limitation for the study of fossilized microbes due to their homogeneous density compared to the surrounding medium.

Therefore, for the investigation of micrometric-size, homogeneous density microfossils using X-rays, it gets clear that both phase-contrast and nanometric-resolutions are required. An approach which can satisfy these conditions and fill a gap in resolution and size of sample between Transmission Electron Microscopy and micro-CT is Ptychography, a type of X-ray microscopy based in Coherent Diffraction Imaging (CDI) (detailed in section 1.2.3.1) that has been developed in the past decades providing important advances in different fields from material sciences to biology (see Miao et al. 2015 for a review). CDI methods and Ptychography can reconstruct both the amplitude and phase components of objects and overcome the resolution limits imposed by X-ray optics. Moreover, by coupling the measurements to tomographic setups, 3D data can be obtained by the method called Ptychographic X-ray Computed Tomography (PXCT).

The following sections will discuss the basis of Coherent Diffraction Imaging and Ptychography, their physical principles and the reconstruction algorithms.

1.2.3.1 INTRODUCTION TO COHERENT DIFFRACTION IMAGING

In the X-ray regime, the limiting resolution for a microscope, as described by the Rayleigh criterion in the Equation (1, is no longer limited by the wavelength of the radiation, but to the quality of the X-Ray focusing optics. The inherent properties of X-Rays, such as its high transmissibility to most of materials and requirement of diffractive optics for a sub-micrometric focusing impose practical limitations for the fabrication of high-quality X-ray lenses.

D. Sayre first conceived the idea of extending the methods of X-ray crystallography for resolving non-periodic structures from their diffraction pattern (62-63), foreseeing a new type of “lensless” X-ray imaging which received the name of Coherent Diffraction Imaging (CDI). It took almost 50 years since Sayre’s first envisage for a successful implementation of this approach, in an array of 100 nm gold dots using soft X-rays. (74)

In a similar process to the image formation in visible light microscopy described in the section 1.2.1, the lenses of a microscope mathematically perform an Inverse Fourier Transform of the diffraction pattern of the object. The main difficulty of computationally performing this process is a well-known problem on protein crystallography called *phase-problem*. Several CDI techniques were developed in the last decade exploring different approaches for resolving the phase problem and focusing in different resolutions and sample properties (Figure 14) (see Miao et al. 2015 for a review).

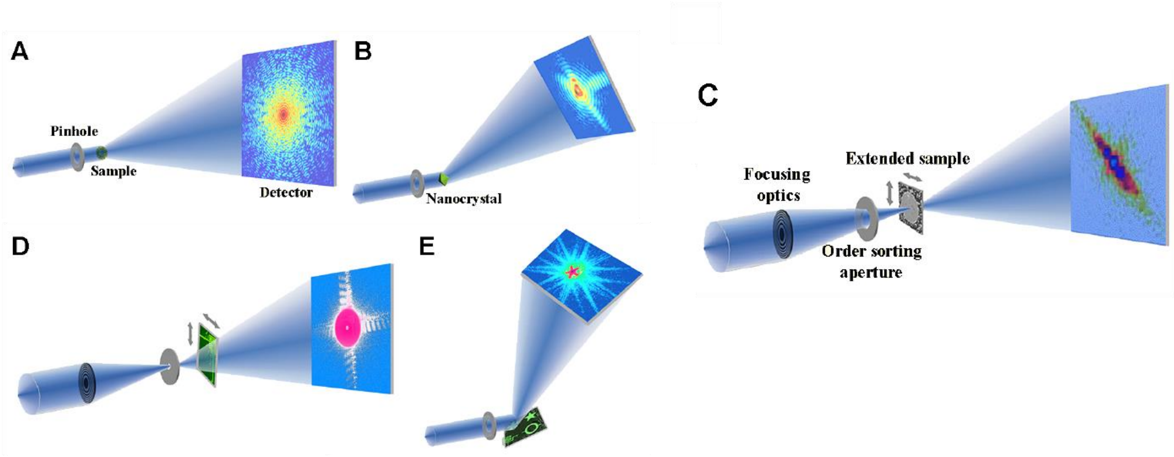

Figure 14 - Schematic representation of different CDI methods. **A,** Plane-wave CDI: a sample smaller than the beam is illuminated by a plane wave and a oversampled diffraction patterns is recorded. **B**, Bragg CDI: a nanocrystal is illuminated by a coherent beam and the diffraction pattern surrounding a Bragg peak is measured. **C**, Ptychography: a coherent beam is used for scanning an extended sample while diffraction patterns are collected from partially overlapping regions. **D**, Fresnel CDI: a defocused probe illuminates a sample and the Fresnel diffraction pattern is measured. **E**, Reflection CDI: A coherent x-ray beam illuminates a sample and the reflected light is collected with high numerical aperture.

Source: Adapted from MIAO et al. (71)

In order to discuss the fundamentals of CDI, a brief description of the principles of X-ray scattering and the phase-problem will be presented in the following sections. The physics and mathematics described are based on Willmott 2011, Als-Nielsen and McMorrow 2002 and Pfeiffer 2018. (54,65-66)

1.2.3.2 PRINCIPLES OF X-RAY SCATTERING

The general expression describing an incoming radiation propagated in the direction **k** and time *t* is given by:

$$E(\boldsymbol{r},t) = E_0 e^{i(\boldsymbol{k}.\boldsymbol{r}-\omega t)} \tag{8}$$

where E_0 is the amplitude of the electric field, **k** is a wave vector and ω is the angular frequency.

The scattering of an X-ray beam by an atom will be affected by the binding energy of its electrons. The distribution of charge associated to this energy can be modeled as an electron density $\rho(\mathbf{r})$ in function of the distance from the nuclei **r.** The scattered radiation field is composed by the scattering contributions of all the volume elements which are not scattering in phase and are contributing to this charge. The phase shift between the scattered wave from one volume element and a neighboring element can be described as:

$$\Delta\phi(\boldsymbol{r}) = (\boldsymbol{k}-\boldsymbol{k}').\boldsymbol{r} = \mathbf{Q}\,.\,\mathbf{r} \tag{9}$$

where **k** is the incident wave vector and k' is the scattered one. The difference between these vectors is **Q,** known as the *scattering vector.*

The scattering vector is a central parameter in the scattering process as describes the changes in energy during this process in relation to the scattering angle θ.

The total scattering of an atom is defined considering a volume element d**r** at **r** which will contribute by $-r_0\rho(\boldsymbol{r})d\boldsymbol{r}$ to the scattered field, being r_0 the classical radius of the electron. Considering also a phase factor $e^{i\mathbf{Q}.\mathbf{r}}$**,** we describe the total scattering as

$$-\,r_0 f^0(\mathbf{Q}) \;=\; -r_0 \int \rho(\boldsymbol{r}) e^{i\mathbf{Q}.\boldsymbol{r}}\, d\boldsymbol{r} \tag{10}$$

Where $f^0(\mathbf{Q})$ is the *atomic scattering factor* and describes the total scattering amplitude of an atom. The right side of the equation is a Fourier transform, showing that it is possible to retrieve the electron density of an atom by performing an inverse Fourier transform of its scattering factor.

At energies much below the binding energy of the core electrons, the X-rays will reduce the scattering length in a factor of f'. When the energy is much greater that the binding energies, the electrons can be considered as being free from atomic bounding influences. However, below a limit, we should consider that X-rays will be in some part absorbed, and the posterior re-emitted radiation will interfere with the scattered part, altering both its amplitude and phase. This effect can be corrected by adding to the atomic form factor f a component $f"$ which accounts the increasing phase lag in respect to the driving field as the photon energy approaches the absorption edge of an electron. Considering that the absorption is expressed in the electromagnetic wave equation as an imaginary term, the atomic scattering factor can be defined as complex term:

$$f(\mathbf{Q},\omega) \; = \; f^0(\mathbf{Q}) \; + \; f'(\hbar\omega) \; + \; if"(\hbar\omega) \qquad (11)$$

where $\hbar\omega$ comes from the definition of the energy of the electromagnetic radiation $\varepsilon = \hbar\omega$, showing the dependence of these factors with the incident X-ray energy.

The sum of the individual atomic scattering factors of an object is the so-called *structure factor* F_{hkl}, and, as an extension of the Equation (10, consists in a Fourier transform of the object. This means that, once the structure factor is retrieved, an inverse Fourier transform can provide the electron density distribution of an object.

However, the diffraction signal recorded in a detector corresponds to the scattered intensity, which is the absolute square of F_{hkl}, a scalar component. Since F_{hkl} is a complex number, we can describe its correlation with *I* as

$$\mathrm{I}_{hkl} = \; |\mathrm{F}_{hkl}|^2 = F_{hkl}F^*_{hkl} \qquad (12)$$

This means that, when trying to obtain the structure factor from the measured intensity, only its real part can be retrieved, and the imaginary part, namely the phase (see Equation (10), is lost. This is the principle of the so-called *Phase problem.*

1.2.3.3 PTYCHOGRAPHY RECONSTRUCTION

CDI techniques are based in measuring the intensity of the diffraction pattern in the far field using a coherent illumination. This coherence permits the retrieval of the phase, which is done by iterative algorithms, starting from a guess object and updating it based in constrains in the real and reciprocal space. In the reciprocal space, the constrain requires that the diffraction pattern recorded is oversampled. In the real space, the constrain is given by the spatial extent of the sample, meaning that the sample should be smaller than the micrometric-size illuminating beam, which represents a practical limitation for samples to be analyzed using this X-ray microscopy.

Ptychography is an imaging technique which allows one to overcome these limitations by acquiring oversampled diffraction patterns through a scanning of the sample and thus providing a sufficient over-sampling of the object with areas illuminated multiple times. The large amount of overlapped data allows a quick and robust reconstruction of both the object and the illumination function (probe), even for partially-coherent sources. This scanning approach also allows the imaging of laterally extended objects, which transformed this technique in an X-ray microscopy of great interest for all the modern synchrotron sources.

The basis of the methods for ptychographic phase-retrieval, or reconstruction, can be understood if we consider that the complex exit waves ψ in a position **r** after the sample can be described as a contribution from the object O and the probe P, given by:

$$\psi = P(\boldsymbol{r})O(\boldsymbol{r}) \tag{13}$$

As explained in the section 1.2.3.2, the measured diffraction intensities I_{hkl} are scalar components, which can here be described as the square Fourier transform of the exit wave ψ

$$I_{hkl} = |\mathrm{F}\{\psi(\boldsymbol{r})\}|^2 = |\mathrm{F}\{P(\boldsymbol{r} - \boldsymbol{r}')O(\boldsymbol{r})\}|^2 \tag{14}$$

Where P(**r** - **r'**) is the complex probe illumination translated by the scanning positions **r'**. The reconstruction algorithms aim to numerically find the complex-valued object O(**r**) such that all the measured diffraction intensities I_{hkl} match the calculated Fourier transform of the complex exit wave ψ. This condition describes what is referred as the Fourier constrain. The second part of the expression describes the overlap constrain, which states that ψ is represented by the multiplication of the object and illumination functions for all positions **r'**.

The first algorithm called ptychographic iterative engine (PIE) (77) was developed to find a solution for this problem based in a known probe, which experimentally represents a practical limitation since the illumination function is usually not known precisely. The algorithm was then updated to start with a guess probe and then update both probe and object. It and received the name of extended PIE, or ePIE. (78) Basically, the algorithm starts by calculating an exit wave using guess objects O (**r**) and probe P(**r**) functions. This guess is propagated to the Fourier domain and the calculated intensity is replaced by the measured data, while keeping the phase. The updated wave is propagated back to the real domain and used to update the probe and object functions based on the overlap constrain. This cycle is illustrated in the Figure 15.

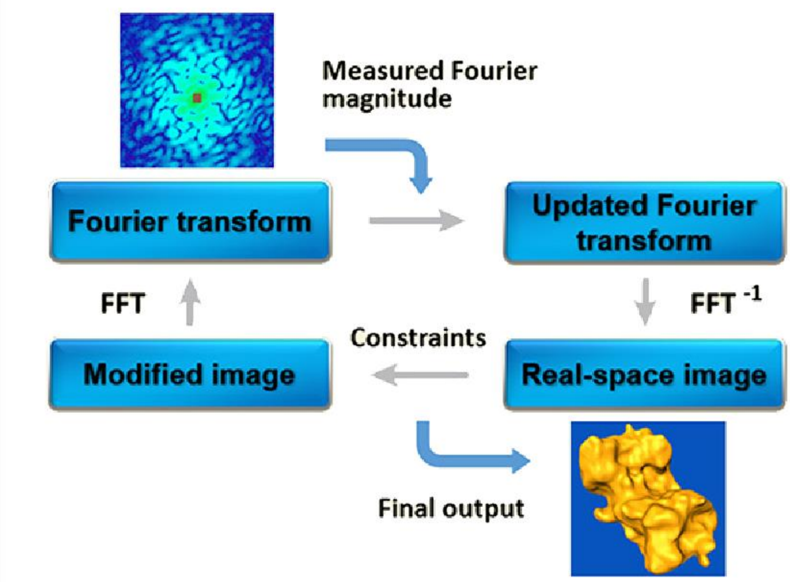

Figure 15 - Schematic representation of a cycle of a basic phase retrieval iterative algorithm for CDI methods. The algorithm starts with a guessed exit wave ψ which is propagated to the reciprocal space using a Fourier transform, and is then updated by substituting the intensity modulus by the measured data, while keeping the phase. This new ψ is propagated back to the real space and the overlap constrain is applied. This new real space ψ will be used in the next iteration of the algorithm.

Source: Adapted from MIAO et al. (71)

After PIE, several other algorithms have been developed for reconstruction or optimization of ptychography reconstructions, allowing significative improvements in the quality of the images and velocity of the reconstruction. Important to mention, the algorithms applied in this work were the Difference-Map (69-70), and Maximum-Likelihood Refinement. (81)

1.2.3.4 PTYCHOGRAPHIC X-RAY COMPUTED TOMOGRAPHY

The high resolution and phase contrast of ptychography was first explored in 3D by Dierolf et al. 2010 (82) using a combination of the ptychographic set up with a rotational tomographic stage and received the name of ptychographic x-ray computed tomography (PXCT).

By exploring the high phase sensitivity of ptychography in 3D, this technique generates quantitative electron density maps of extended specimens at the nanoscale, without any prior assumption such as negligible absorption or homogeneity. Similar to a conventional computed tomography, the 2D projections reconstructed from the ptychography data are used for the 3D reconstructions using standard tomography algorithms, such as Filtered-Back-Projection (FBP).

The capability of obtaining absolute quantitative electron density from the phase information is also an advantage of this approach over conventional tomography methods. From the electron density, the mass density can be calculated (83), and this information can be used for segmenting the different structures (84) and even for interpreting the results and.

1.2.3.5 RELEVANCE OF PXCT FOR THE STUDY OF MICROFOSSILS

For the study of Precambrian microfossils, we can summarize the following advantages of PXCT:

- The high phase-contrast allows microfossils of different compositions to be imaged, even the kerogenous structures that do not present high attenuation contrast;
- The nanometric resolution permits the investigation of the ultrastructure of the fossil cells, providing information relevant for the understanding of their morphology and taphonomy at the nanoscale. The integration of these information can allow more robust evaluations of biogenicity;
- The high penetrability of X-rays 3D information thus obtained are extremely important for completely resolving the micrometric-size specimens. This 3D evaluation is essential specially for the evaluation of controversial, poorly preserved or overlapping specimens;

- The quantitative electron density can provide a complementary geochemical information, which are valuable for challenging biogenicity and deciphering the taphonomic processes involved in the fossilization.

2 OBJECTIVES

The main objective of this thesis is to evaluate the potentials of ptychographic X-ray computed tomography as a novel method of nanopaleontology for the investigation of Precambrian microfossils. These ancient records of life are of complex evaluation, and a lot of controversy remains for the demonstration of biogenicity of several Archean structures described as fossilized microbes. This work aims the development of the approach for inspecting *bona fide* and putative Precambrian microfossils with PXCT for achieving resolution, contrast and sampling volumes which are not covered by other imaging techniques applied thus far. The morphological, geochemical and taphonomic information obtained will be integrated for refining the current the biogenicity criteria based in 3D quantitative nano-imaging.

2.1 SPECIFIC OBJECTIVES

- Development of the approach for the investigation of microfossils with PXCT. This includes the strategies and methodologies for sample selection and preparation, experimental setup, data treatment (tomographic segmentation, morphometric analysis, quantitative mass density estimation) and presentation of results;
- Evaluate the capabilities in contrast and resolution of PXCT for scrutinizing microfossils of different geochemical compositions (carbonaceous and mineralized);
- Evaluate the structures that can be distinguished on microfossils of different morphologies and composition and compare with what was observed by visible light microscopy;
- Perform 3D morphometric analysis for obtaining quantitative, morphological biogenicity criteria;
- Evaluate *bona fide* microfossils for elaborating a basis of the biogenic/taphonomic features observed that can be applied to evaluate

controversial structures. This includes micron and nanoscale evaluation of morphology, ultrastructure, geochemical composition, and traces of taphonomic alteration;

- Use the geochemical information obtained for assessing the taphonomic history of the rock and evaluate its consistency with the presence and preservation of the structures;
- Use the knowledge obtained from the *bona fide* specimens for evaluating the biogenicity of spheroids described as microfossils from the Barberton Greenstone Belt;
- Refine the biogenicity criteria at the nanoscale in 3D with PXCT.

3 MATERIAL AND METHODS

3.1 SAMPLES DESCRIPTION

For a proper evaluation of the strengths and limitations of PXCT in the study of Precambrian fossils, a set of samples composed by exceptionally well-preserved *bona fide* microfossils, poorly preserved structures, carbonaceous cell walls and putative early-Archean microfossils was selected.

A brief description of the samples and their geological context will be given in the following sections. All the samples belong to the collection of the Center for Molecular Biophysics (CBM), CNRS, Orleans, France, under responsibility of Dr. Frances Westall.

3.1.1 *BONA FIDE* MICROFOSSILS FROM THE GUNFLINT BIOTA (1.88 GA)

The Gunflint biota comprise the most remarkable Precambrian assemblage since it contains the oldest universally accepted microfossils from the Schreiber Beach Locality described by Barghoorn and Tyler in 1965. As described in the section 1, this diversity and exceptional preservation of the structures make this biota a references for evaluating the resolving capabilities of novel imaging techniques (49,61).

From this formation, we analyzed specimens from two Localities: Schreiber Beach and Mink Mountain.

3.1.1.1 GEOLOGICAL SETTING

The Paleoproterozoic Gunflint Iron Formation (1.88 Ga) is the middle unit of the Animikie Group. It is a 120-m-thick formation that extends for approximately 175 km, from Thunder Bay (Ontario, Canada) to northern Minnesota. The formation was interpreted as peritidal deposits, formed in shallow-water, marine evaporitic settings. (75-76) The upper and lower members record transgressive-regressive marine cycles.

Microfossil-bearing stromatolites are confined within two separate meter-scale intervals containing a diverse assemblage of stromatolite forms. The Gunflint formation hosts a diverse microbiota preserved in carbonaceous and iron oxide filaments and spheres within a microcrystalline quartz (chert).(31,87)

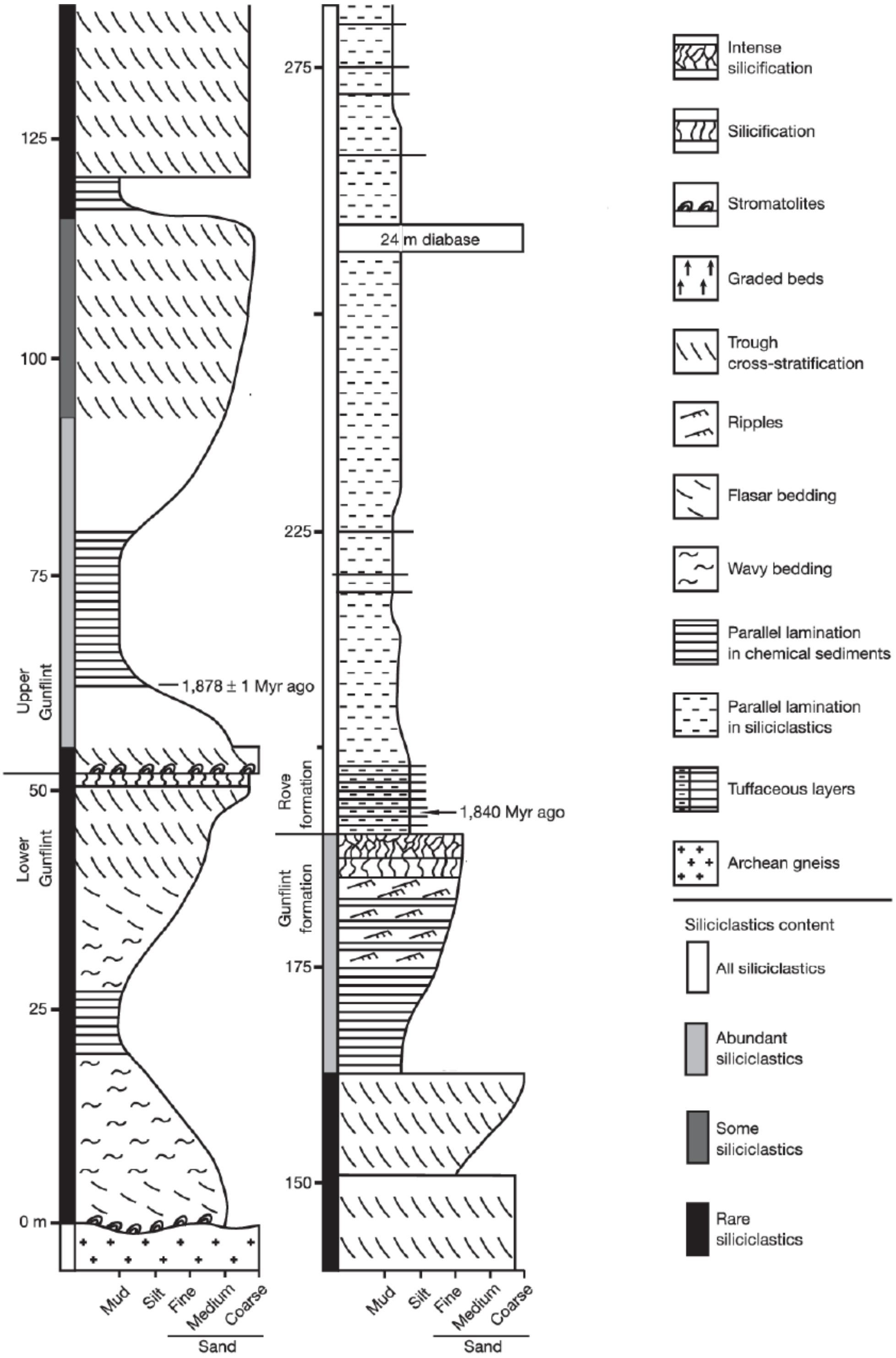

Figure 16 - Simplified stratigraphic representation of the Gunflint Formation.
Source: Adapted from POULTON et al. (88)

3.1.1.2 SPECIMENS SELECTED

Schreiber Beach

Schreiber Beach corresponds to the locality where best preserved specimens described by Barghoorn and Tyler 1965 are found. Previous nanoscale analysis described these fossils to be composed by kerogenous material (48,89) of low maturation state. (19) Different iron minerals have been described in specimens from this locality, such as pyrite (90), Fe-silicates and Fe-carbonates. (20)

A large diversity of morphologies was observed in the petrographic analysis. The specimens have a brownish color characteristic of kerogenous material and apparent variable cell-wall thickness, but details of their ultrastructure could not be distinguished due to the limit of resolution of the petrographic microscope.

Three regions of same thin section were selected and named GF1, GF2 and GF3. They contained several different morphologies including filaments of different thickness, spheroidal microorganisms of variable diameter and other complex morphologies. These specimens were distributed within the *z* plane and could be distinguished varying the focus on the petrographic analysis (Figure 17).

Sample identification: GF55

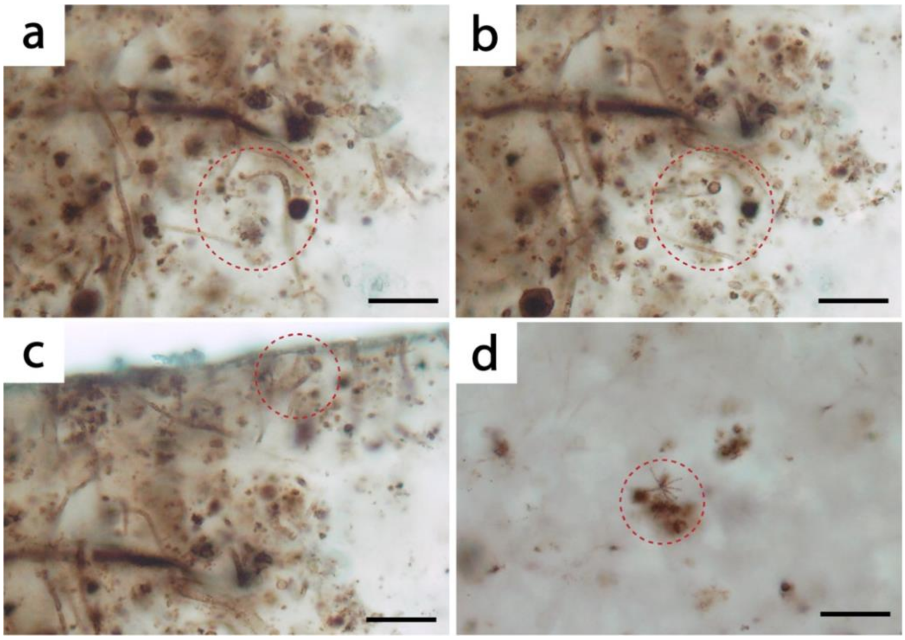

Figure 17 - Regions of Gunflint Schreiber Beach selected for the analysis. **a,b,** GF1 observed in two different depth focus. Several specimens of variable morphology are distributed in different depths. **c,** GF2 approximated region containing filaments and spheroids. **d,** GF3 containing one specimen of *eoastrion* and other spheroids. Scalebar 15 μm.

Source: By the author

Mink Mountain

The microorganisms of Mink Mountain are poorly preserved if compared to the specimens of Schreiber Beach. They have been described as carbon-poor specimens, substituted by iron-oxide, precisely secondary hematite after magnetite. (85,87) Zones rich in filamentous objects were observed to occur on the limbs of centimeter-scale domical and pseudocolumnar stromatolites. This was the only morphology observed in our samples and a region containing filaments of different length was selected (Figure 18).

Sample identification: 07CA22

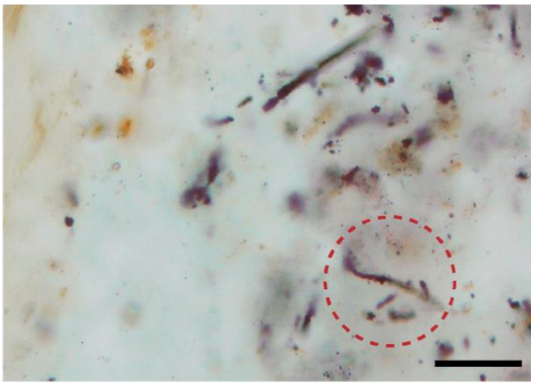

Figure 18 - Micrograph of iron-oxide coated filaments selected from the Mink Mountain locality of the Gunflint Formation. Scalebar 10 μm.
Source: By the author

3.1.2 CARBONACEOUS *BONA FIDE* MICROFOSSILS FROM THE DRAKEN FORMATION (700 - 800 MA)

3.1.2.1 GEOLOGICAL CONTEXT

Exceptionally well-preserved carbonaceous microfossils from the Draken Formation, Svalbard, Norway, were selected. This consists of a Neoproterozoic deposit with sediments forming a dolomitic conglomerate which includes silicified clasts rich in microfossils, stromatolites and oolites. (91) From the stratigraphic setting, it has been inferred that the depositional setting consisted of a quite shallow-marine environment, where the microbial mats accumulated protected from the open sea by some type of physical barrier. Turbulence periods probably occurred alternately, leading to stormmediated burial and subsequent early silicification, resulting in the fine preservation state of the microfossils encountered in this conglomerate.

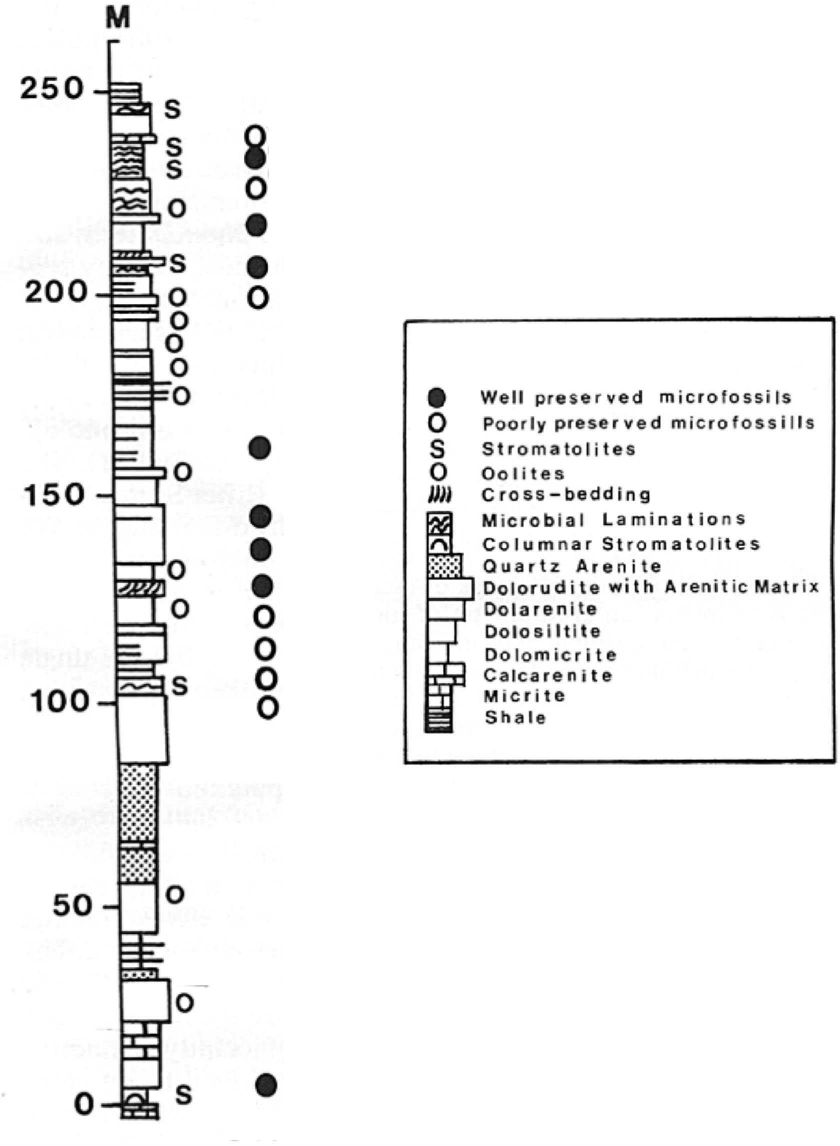

Figure 19 - Simplified stratigraphic representation of the Draken Formation.
Source: Adapted from KNOLL (92).

3.1.2.2 SPECIMENS SELECTED

The specimens selected for the PXCT analysis were described as allochthonous planktonic microbes (91) and are identified as the genus *Myxococcoides*. Specimens were found isolated or in colonies, and one of each type was selected.

Sample identification: 14SJ02

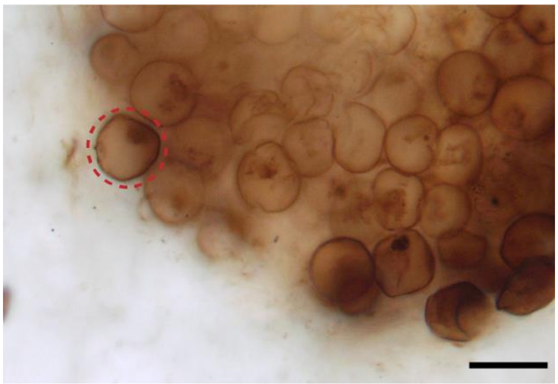

Figure 20 - Micrography of the selected colonial specimen (DK1) identified as *Myxococcoides sp.* of the Draken Formation. Scalebar 20 µm.
Source: By the author

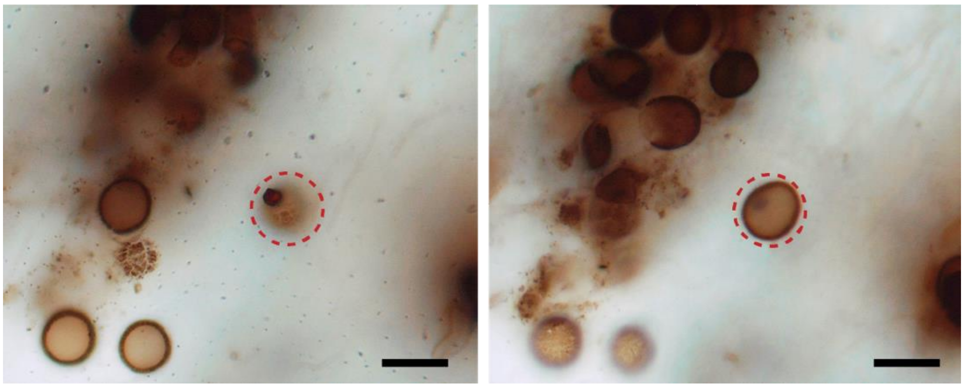

Figure 21 - Micrographs in different focus planes of the selected isolated specimen (DK2) identified as *Myxococcoides sp*. of the Draken Formation. Scalebar 20 µm.
Source: By the author

3.1.3 PUTATIVE MICROFOSSILS FROM THE BARBERTON GREENSTONE BELT (3.45 GA)

The Barberton Greenstone Belt (BGB) comprise one of the only two well-preserved groups of early Archean rocks on Earth and represents an important window to the emergence and evolution of life on Earth. A variety of traces of early life have already been described in different units of this geological sequence (see (22,93) for reviews). They are summarized in figure (Figure 23).

We are focused on the evaluation of the spheroidal structures of approximately 1 µm of diameter, interpreted as coccoidal bacteria (56) based in size, shape, paired morphology that resemble cell-division and colonial distribution. Westall et al. 2001 (56) investigated these structures in high-resolution using SEM after acid-etching the samples, and revealed, for the Hoogenoeg Fm., some rod-shaped structures that could also represent bacillar bacteriomorphs. (Figure 22). The etching procedure, however, can also introduce crystallites artefacts in the samples, adding controversy to their interpretation according to Altermann 2002. (94) This controversy was also extended to biogenicity of the spheroids, which according to this author, strongly resemble fluid inclusions.

The reliance on morphology for a biological interpretation is problematic for these structures, which correspond to a morphotype that is very challenging to be distinguished from diagenetic features.

These samples are therefore well-suited for testing the capabilities of PXCT for assessment of biogenicity. The results obtained in the *bona fide* microfossils from other formations could also serve as a basis of the characteristics and types of biogenic features that can be searched in the samples from BGB using this approach.

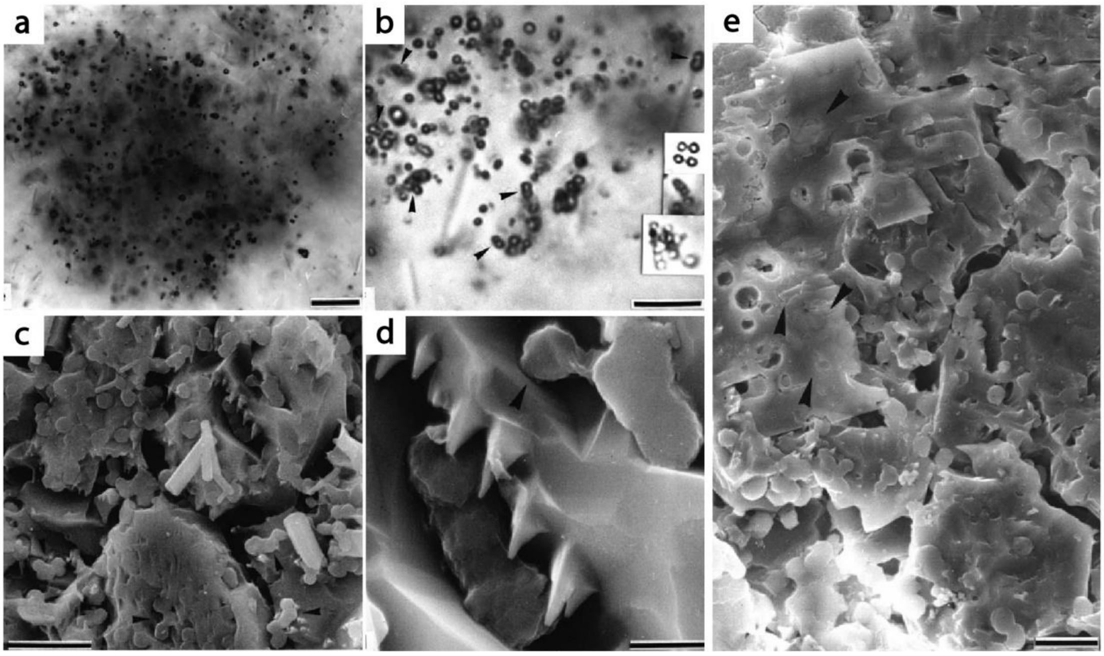

Figure 22 - Spheroidal structures from Kromberg Formation described as coccoidal microfossils (56). **a,b,** Petrographic micrographs showing the colonial habit and distribution in groups of two or more spherules. Scalebar 10 μm. **c,** etched samples analyzed by SEM. Cluster of spherules are visible together with acicular minerals. Scalebar 5 μm. **d,** Detail of image c showing a linear association of three spherules. Scalebar 0.5 μm. **e,** cluster of spherules partially embedded in secondary calcite. Scalebar 5 μm.

Source: Adapted from WESTALL et al. (56)

3.1.3.1 GEOLOGICAL CONTEXT

The Hoogenoeg (3.472 – 3.416 Ga) and Kromberg (3.416 – 3.334 Ga) Formations are sequential units of the Onverwacht Group of the Barberton Greenstone Belt (Figure 23).

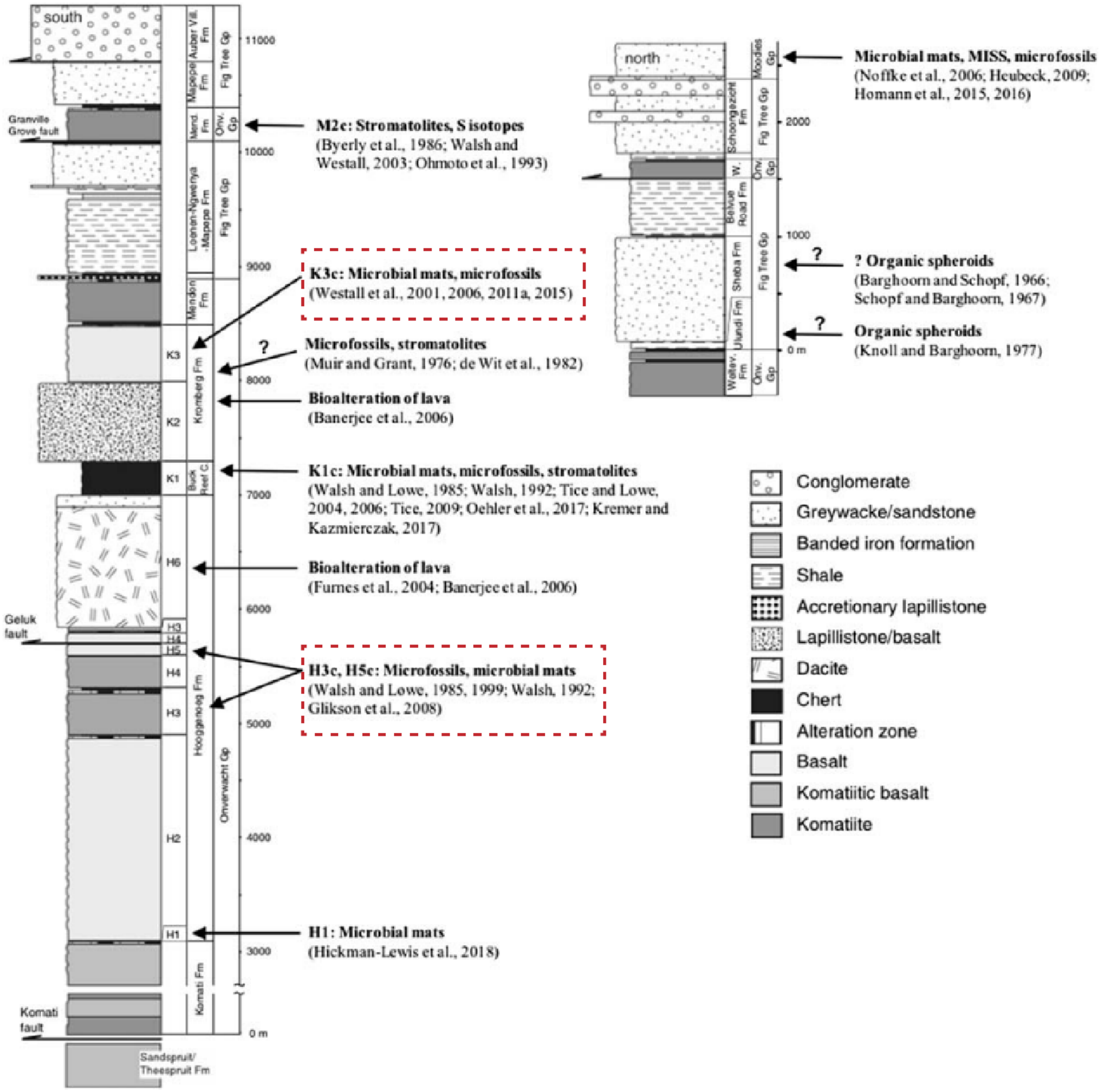

Figure 23 - Generalized stratigraphic representation of the Barberton greenstone belt with the traces of life of life that have been described in the different groups. The red boxes indicate the provenance of our samples.

Source: Adapted from HICKMAN-LEWIS et al. (93)

The Hoogenoeg Formation consists of basalt and volcanic rocks (komatiite) with interbedded chert horizons. (22,93) It has been interpreted as an intercalation of volcanic pulses with quiescent periods of sedimentation. The Kromberg unit is composed by cherts alternated by basalts and sandstone horizons. Our samples are from the Josefsdal Chert, a sedimentary unit interpreted as shallow-water environment and subdivided in in facies that represent with a regressive-transgressive sequence of deposition terminated by renewed volcanism. (93)

3.1.3.2 SPECIMENS SELECTED

We selected samples from the same sets analyzed by Westall et al. 2001. For each formation, two spots in spheroids-rich regions were selected (Figure 24). They will be referred as samples KB1 and KB2, HG1, HG2.

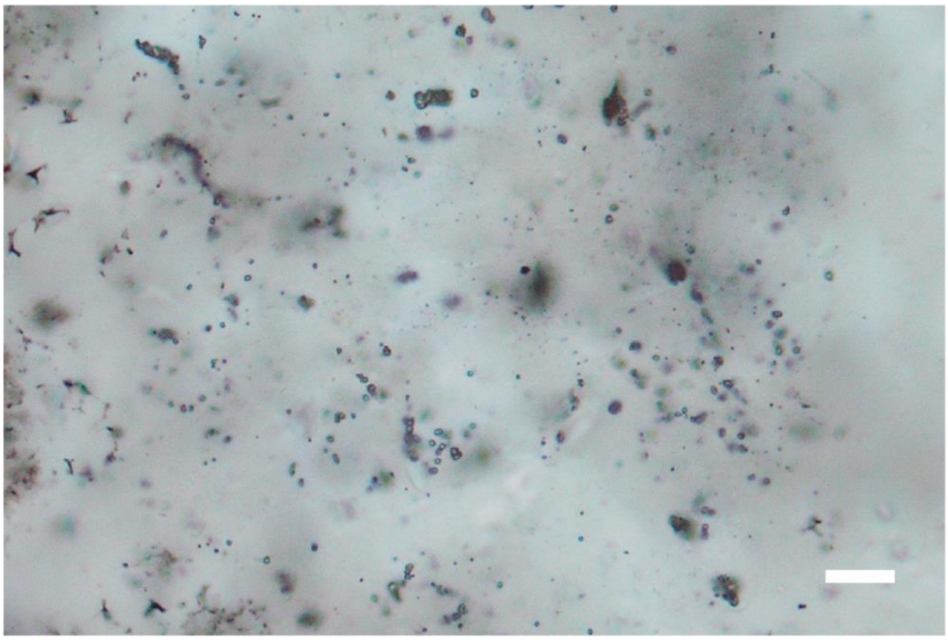

Figure 24 - Example of spheroid-rich region of the sample from the Hoogenoeg Formation were the FIB-milled pillars were extracted. Scalebar 10μm.
Source: By the author

Hoogenoeg:

Sample identification: MW37-7

Kromberg:

Sample identification: SA-1

3.2 SAMPLE PREPARATION

This work consists in the first application of PXCT to microfossil, and therefore the development of a sample preparation protocol consists in a crucial part of this project.

Aiming the best quality of data possible, the definition of the best shape for the samples should take in account some characteristics inherent from the experimental method.

First, for the tomographic measurements, samples need to be rotated 180 degrees while remaining in the field of view. For fulfilling this requirement, and maintaining a relatively homogeneous depth during the rotation, while avoiding sharp edges that could potentially create diffraction artefacts, the best geometry possible is a cylinder.

For defining the size of this cylinder, one needs to take in account that each tomographic projection of PXCT consists in the measurement of several superposed spots, and consequently the scan time scales linearly with the volume of the sample and in the fourth power with the aimed resolution. Therefore, we defined the diameter of the samples as 15 to 20 μm, for considering this an adequate sampling volume for containing one or several microfossils, depending on their size, while still achieving feasible scan times and good spatial resolution for the limited beamtime that we have in a synchrotron experiment.

The first challenge was to ensure that each cylinder contained the structures of interest. For being able to cut and extract samples with high a precision, cylindric pillars were prepared by FIB-SEM. The height of these pillars varied depending on the time necessary for the milling of the rock and is, in average, equal to their diameter.

The protocol for defining the sampling region is illustrated in the Figure 25 and consist in the following steps:

- Samples have been previously prepared as petrographic thin sections of 30 μm thickness and without cover glass.
- Petrographic analyses were performed for selecting the specimens and regions of interest. An important criterion was the selection of specimens close to the surface to ensure they would be inside the extracted pillar.

- The region of interest was photographed using transmitted light, which is the type of illumination that allows the detection of the microfossils.
- The same area was also photographed using reflected light, an illumination that provided surface information.
- These images were overlapped in order to correlate the structures of interest with topographic features that could be detected in the SEM. When the sample had no surface features, a diamond marker was used to create fiducial marks to be used as reference.
- Based in the correlation of topographic information, these regions of interest were localized in the SEM. "Zooming" series of images were recorded for allowing the FIB-SEM operator to localize the regions.

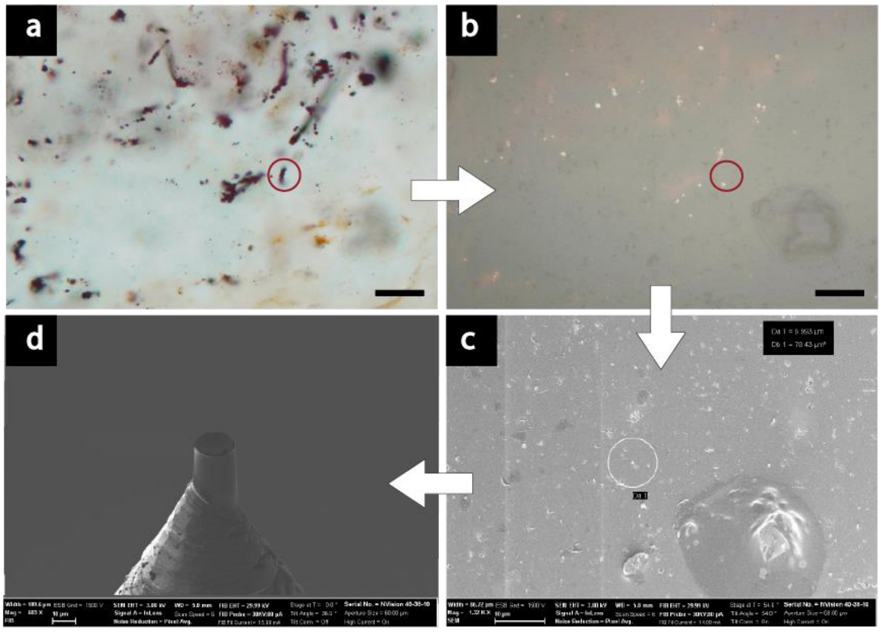

Figure 25 - Example of the protocol for preparing the cylindric samples for PXCT. **a**, Visible Light micrograph showing the structures of interest (red spot) using transmitted light and **b,** the same field of view observed by reflected light. **c,** SEM image showing the same spot observed in **a** and b. **d**, SEM image of the resulting pillar after the FIB milling and mounting in an OMNY pin (95). Scalebar: 20 µm.

Source: By the author

The preparation of cylindric pillars is not a common protocol for FIB-SEM laboratories since this is not the standard geometry used for other approaches. Most of our samples were prepared at ScopeM, Zürich, Switzerland, due to their experience with this preparation, specific for PXCT experiments. The procedure was conducted by Dr. Joakim Reuteler using a Zeiss NVision 40 Gallium.

Two samples were prepared by Dr. André Rossi from the LABNano, at the Centro Brasileiro de Pesquisas Físicas. This was the first time that this type of sample was prepared in this laboratory, and due to limits in the angle range of the microscope stage (TESCAN LYRA3), the samples could not be prepared as perfect cylinders. The implications of this limitation are discussed in the section 4.2.4.

The pillars were mounted on PXCT pins designed for the setup of cSAXS beamline, the flOMNI tomographic pins. (95)

3.3 PXCT MEASUREMENTS

The PXCT measurement were performed in two rounds of experiments at the cSAXS beamline of the Swiss Light Source (SLS) at the Paul Scherrer Institut, Villigen, Switzerland. These experiments were part of the proposals 20171702 and 20181078, of which I was the author and principal investigator and comprised a total of 24 shifts (8 days) of beamtime.

The cSAXS (X12SA) is the coherent Small-Angle X-ray Scattering beamline of the SLS. It has an energy range of 4.4 – 17.9 keV, and beam size range of 25x10 μm^2 to 1.5x0.8 mm^2. We used a photon energy of 6.2 keV because it corresponds to the optimum flux of the beamline (~2x10^{12} photons/sec at E = 6.2keV, 400mA ring current). The measurements were performed using the flOMNI setup. (96) The sample was placed downstream of the focal spot, and the beam at the sample position had a diameter of approximately 4 µm. The scan points were positioned following a Fermat spiral trajectory (97) with a step size of 1.2 µm and consequently 70% of overlap, and an exposure time per point of 0.1 s. The ptychographic projections were reconstructed in an area of 300×300 pixels of the Pilatus detector with pixel size of 172 μm^2 (experiment 20171702, samples GF1, GF2, DK1, MM, KB1 and HG1) and of 400x400 pixels of the Eiger detector with pixel size of 75 μm^2 (experiment 20181078, samples GF3, KB2, HG3, DK2), both placed 7.362 m downstream of the sample. We used 600 iterations of the Difference Map (DM) algorithm (80) followed by 400 iterations of the Maximum Likelihood (ML) refinement. (81) For tomography, 1100 projections equally spaced over a 180-degree angular range were recorded. The phase of the reconstructed projections was used after post-processing alignment and removal of constant and linear phase components (88-89), and a modified filtered backprojection algorithm was applied for the tomographic reconstruction. The final 3D resolution of each set of data was determined by Fourier shell correlation (FSC) (100) with the ½-bit threshold criterion. (101)

3.4 IMAGE TREATMENT

To separate virtually the different materials present in the tomographic data, the process of segmentation was applied on the images. It consists in generating different masks (*labels*) for each material of interest in all the tomographic slices (Figure 26). These can be then used for the generation of 3D surfaces and data reduction (section 3.5

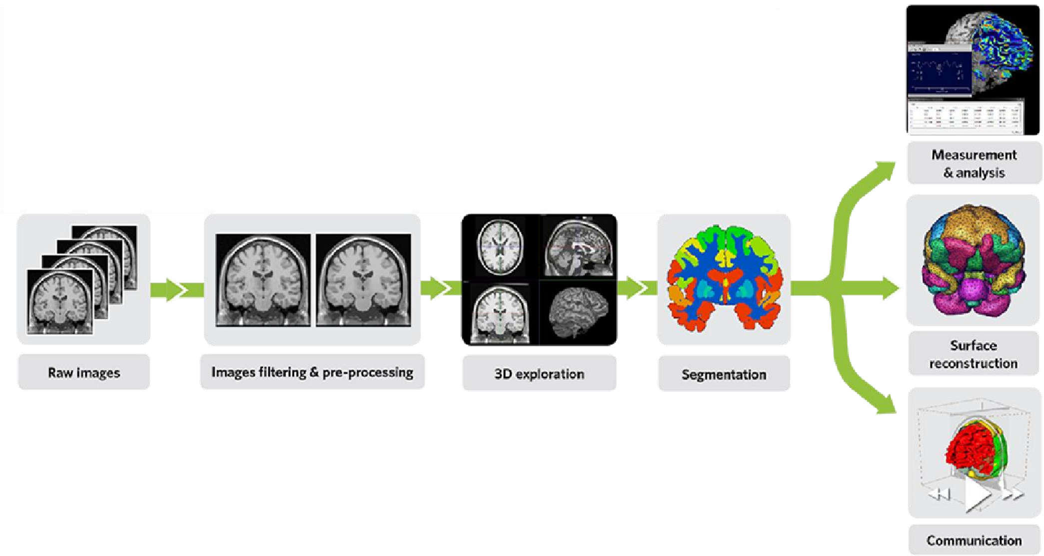

Figure 26 - Scheme of the process of segmentation for tomographic data.
Source: AMIRA-AVIZO SOFTWARE (102)

The analysis, treatment and segmentation of the tomographic data were done with the software Avizo 9.5 (Thermo Scientific).

The strategy for the segmentation varied depending of the inherent characteristics of the data, such as the size and shape of structures present, contrast between structures and matrix, presence of noise and/or reconstruction artefacts. The intensity of the pixels was the major criterion for the segmentation due to the quantitative information of electron density. To keep the quantitative information for the pixel intensity of each feature, we did not apply any filter in the images. The structures were segmented mostly using a combination of *threshold* and *magic wand* tools. For the *threshold*, they were first separated in different *labels* based on the intensity histogram, observing which range of intensity better included the pixels of each material. Then, all the slices were evaluated to identify structures or regions that were not segmented due to artefacts such as partial volume effects. These were added to the respective *labels* using the *magic wand*. The *watershed* tool was also used for the data presenting several different material phases, followed by a manual refinement. For this, after the thresholding strategy, the *watershed* was applied, separating all the existing phases in *labels,* and therefore requiring less manual refinement with the *magic wand.*

From the segmented data, surfaces were rendered for analyses and inspections in 3D. Both the 2D tomographic slices and the 3D segmented surfaces were used for the inspection of features. Morphometric analyses were performed using the *measurements* tool and the *label analysis.* For diameter calculation, we applied the function *EqDiam,* which computes the equivalent diameter of the sphere with the same volume of the structure.

For all mass density analysis, the histograms of the segmented materials were evaluated to ensure that the label consisted of only one material phase, and the segmentation was refined in case they were not. The contributions of each material are expected to have a normal distribution in the intensity histogram. (84,102) The removal of pixels in the border, which are composed by a mixture of materials (explained in detail in section 3.5.1), is important for providing the true electron densities values. For decreasing the contribution of such border pixels, the segmented selections were shrunken by 1 to 3 pixels. This procedure was performed iteratively, and the intensity histogram was checked after each compression for evaluating the shape of the histogram distribution. This process was complemented by the function *smooth labels* that was applied with a kernel size of 3 pixels. This function identifies the probability of each pixel to belong to the material or to the exterior based on the intensity of the neighbour pixels within the kernel size. The kernel size was defined based in the fact that the pixel size is smaller (by less than 2 times) than the spatial resolution achieved for all data.

3.5 ELECTRON DENSITY EXTRACTION AND MASS DENSITY QUANTIFICATION

For the quantification of mass and electron densities, the first step is to identify the range of pixel intensities for each material. The high contribution of silica in the intensity histograms of the full volume hinders the identification of the minority phases. Therefore, the segmented data represents an alternative for obtaining more precise intensity values for each material.

The segmented material *labels* were exported as TIFF masks which were used for the extraction of the intensity histogram using the software FIJI. Gaussian functions were fit to the histogram using the software MagicPlot 2.8 (Magic Plot Systems, LCC). These gaussians were used to obtain the center of the pixel intensity distribution of each material and its range of distribution, taken as the full width at half maximum (FWHM) of the curve.

The pixel intensity values of these tomograms provide the real part $\delta(\mathbf{r})$ of the complex refractive index of the sample, $n(\mathbf{r}) = \delta(\mathbf{r}) + i\beta(\mathbf{r})$ (described in section 1.2.2). The electron density $n_e(\mathbf{r})$ was retrieved from the $\delta(\mathbf{r})$ values using the relation $n_e(\mathbf{r}) = 2\pi\delta(\mathbf{r})/\lambda^2 r_0$, where r_0 denotes the classical electron radius and λ the wavelength of the probing radiation, as described in detail in Diaz et al. 2012. All the retrieved electron density values were normalized by the subtraction of the electron density of air.

The mass density was estimated based on the electron density using the formula $\rho = n_e A/N_A Z$, where A is the molar mass, Z is the number of electrons and N_A is Avogadro's number. (83) We used the A and Z of the candidate minerals when known. For kerogen as a candidate, we used the average composition of $C_{175}H_{102}O_9N_4S_2$, estimated by Ungerer, et al. 2015 (103), which results in the ratio of A/Z = 1.92 g/mol and is in agreement with typical values for this ratio in other biological compounds. (84) The ratio of A/Z has been shown to be 1.8 ≥ 2 for materials composed mostly of light atoms. (84) We observed that, for minerals of higher density, (*e.g.* iron oxides: hematite (5.24 g/cm^3) and maghemite (4.87 g/cm^3)) the resulting ratio A/Z is equal to 2.1. For materials of disputed affinity, we used the strategy of starting the calculations with a given ratio (between 1.9 and 2.1 depending upon the electron density) and when obtaining candidates, optimizing the results using the A/Z of the candidates. The calculated mass densities were compared with mineral candidates using the density values found in the mineral database *Mindat.org*.

3.5.1 CONSIDERATIONS OF PARTIAL VOLUME EFFECT FOR QUANTITATIVE ANALYSIS

As described in sections 1.2.3.4, the reconstructed PXCT images provide a quantitative electron density maps of the specimens. The capacity of retrieving true $\delta(\mathbf{r})$ values from the images depends on the spatial resolution and the size of the structure of interest.

In the intensity histogram retrieved from a reconstructed tomogram, the x axis represents the intensity of a pixel, which can be converted in $\delta(\mathbf{r})$, and the y axis represents the counting of pixels with that given intensity. In the interface between an object and its surrounding medium, there is a region where the pixels are composed by more than one material, and their resulting grey value represents an averaged intensity. This can also happen for the presence of non-resolved porosities, *i.e.* smaller than the spatial resolution. This artefact is called partial volume effect and is caused by and dependent on the limit of resolution (93-94) In the histogram, this effect can be seen as a tail in the curve distribution (Figure 27).

Nonetheless, when the objects of interest have small dimensions, *i.e.,* in the order of the spatial resolution, they might have a proportion of voxels (3D pixel) within the region of partial volume effect higher than of voxels contained within the area with the true electron density values for that material. If we consider a spherical particle of radius R, we can describe this effect in terms of the volume V and surface area A_S. For obtaining a higher counting of voxels with true electron density values, this particle should have a number of voxels in the volume (n_V) higher than within the surface of the material (n_A). Considering that the voxel width is the spatial resolution l, the relation $n_V > n_A$ can be define as:

$$\frac{4\pi}{3}\left(\frac{R^3}{l}\right) > 4\pi\left(\frac{R^2}{l}\right) \tag{1}$$

$$R > 3l \tag{2}$$

This states that, for a material to have a histogram with a distribution of pixel intensity consistent with its true electron density, its minimum width in any plane should be higher than 6 times the spatial resolution (diameter of a sphere of radius 3).

Some structures such as the carbonaceous cell walls of organic-walled fossils are commonly compressed or discontinuous due to recrystallization of quartz crystals. This means that, in some planes, these structures present thicknesses smaller than the minimum required for the quantification of their true electron density values. The distribution of intensity values of these materials is observed as a partial volume effect tail in the curve of the silica matrix (Figure 27).

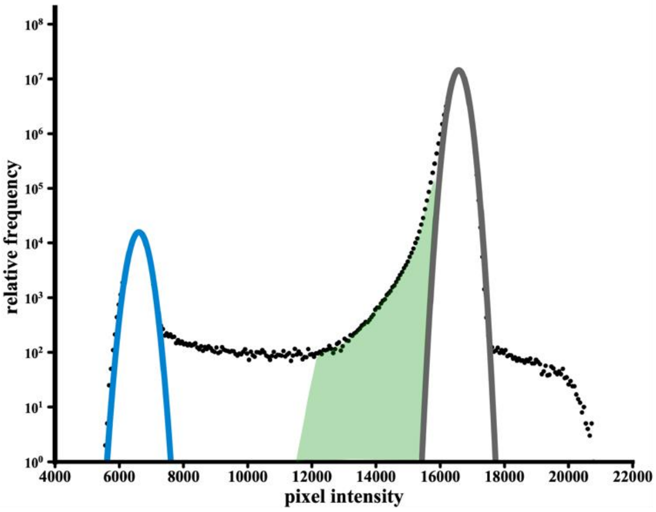

Figure 27 - Histogram of pixel intensity of the sample DK1. The air (blue gaussian) and silica (grey gaussian) curves have a normal distribution. The kerogenous material should be found within the green region but has no distinguishable curve due to strong partial volume effects from the surrounding silica.

Source: By the author.

For the materials where this phenomenon is observed and the mass density cannot be precisely estimated, it is only possible to obtain the minimum or maximum electron density, depending on the density of the surrounding material. For example, since the kerogenous structures are immersed in a silica matrix of higher density, the partial volume effect shifts the intensity to higher values. From the minimum intensity values of the segmented structures, we can have an estimation of the minimum electron and mass density of this material, which could, in principle, provide a preliminary information about it.

Another implication of this effect is that eventual porosities below this limit of size can also lead to misinterpretations of electron and mass densities. Therefore, previous knowledge about the sample mineralogy and degree of porosity is important for the correct interpretation of the results.

4 RESULTS AND DISCUSSION

4.1 MINK MOUNTAIN LOCALITY OF THE GUNFLINT FORMATION

The sample from Mink Mountain was expected to have the best contrast due to the presence of iron-oxides as minerals involved in the preservation of the filaments. (85,87)

The specimens analyzed were interpreted *Gunflintia sp*. Barghoorn 1965 based on morphometric similarity to formerly described specimens from other localities of the Gunflint Formation. (20,31)

The 3D spatial resolution calculated by FSC was 52.5 nm and the pixel size 28.53 nm. The mass densities calculated based in the retrieved electron density and the candidate compounds for this samples are shown in Table 1.

4.1.1 DESCRIPTION OF THE MORPHOLOGICAL FINDINGS

The filaments have a shape consistent with the morphology of *Gunflintia sp*, with an average diameter of 1 μm and variable length. They are immersed in matrix with a mass density of 2.69 ± 0.08 g/cm^3, consistent with quartz (Table 1) as expected from previous studies. (85) Besides the iron oxides already recognized by visible light microscopy (orange in Figure 28 c,d), the filaments are also composed by an irregularly shaped material of low density which was not detected by visible light microscopy (green in Figure 28).

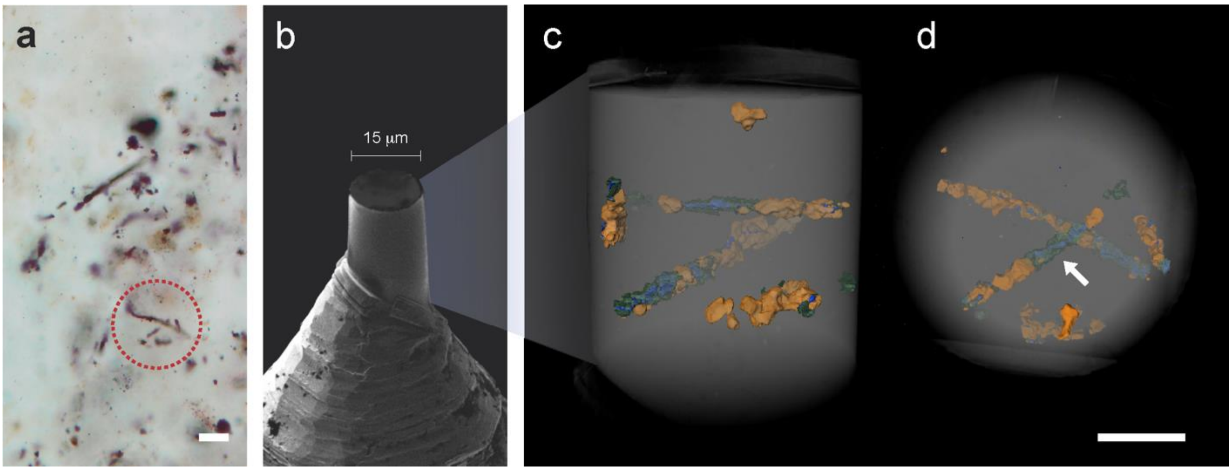

Figure 28 - **a,** Photomicrograph of filamentous microfossils apparently preserved as a red-brown iron oxide by visible light microscopy. The circle indicates the region selected for PXCT analysis. **b,** SEM micrograph of pillar sample prepared by FIB-SEM attached atop the OMNY pin. **c,d,** 3D renderings (side and top views, respectively) of the PXCT data showing the distribution of the fossil filaments in the interior of the pillar. The view in **d** corresponds to the same orientation as the outlined region shown in **a.** The white arrow indicates one of the kerogenous regions (green/blue) invisible in optical microscopy in **a.** The structures in orange represent the only visible features resolved by optical microscopy and correspond to euhedral[10] and anhedral[11] maghemite crystals. Scale bars 5 µm.
Source: By the author.

The electron density distribution of this irregular material consists of a broad curve that suffers from partial volume effects. A separated fit was done in the segmented material to allow a more precise estimation of its mass density (Figure 29).

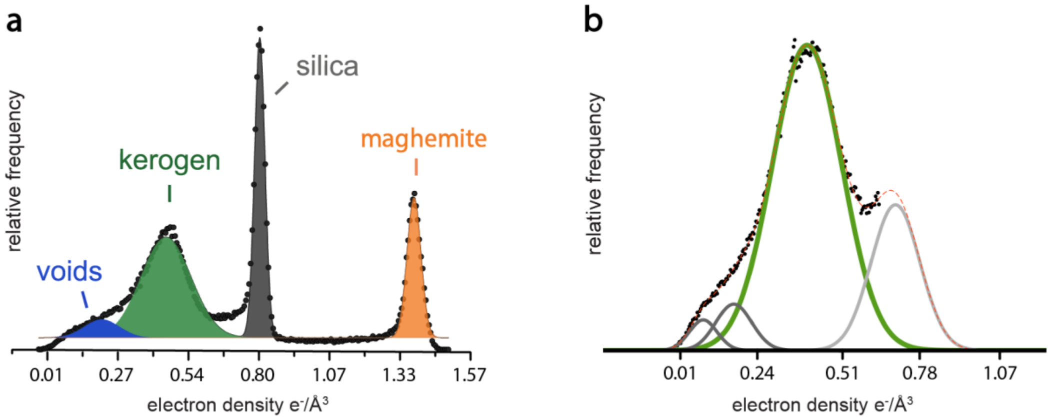

Figure 29 - **a,** Histogram of electron density and Gaussian fits for all materials. **b)** Fit done for kerogen (green) using the histogram obtained from the segmented data for a more precise estimation. The partial volume effects are considered as mixtures of gaussians in the interfaces with silica (light grey) and voids (dark grey).
Source: By the author.

---

[10] Well-formed minerals with sharp, easily recognized faces.

[11] Minerals with no well-formed crystal faces.

The calculated density value is 1.43 ± 0.45 g/cm^3, consistent with the range for density of kerogen (1.19 g/cm^3 to 1.77 g/cm^3) and indicating the prevalence of kerogen of high thermal maturation. (107–109) The presence of more than one curve of lower electron density indicates that unresolved porosities might comprise minor phases of possibly lower density kerogen. The irregular shape can be explained by the displacement caused by Ostwald ripening of silica crystals during late diagenesis. (109) The thermal maturation of kerogen increases its density and induce the formation of pores or microcracks filled with hydrocarbon. (110-111) These cracks are observed inside the kerogenous mass (blue in Figure 28 and Figure 30). They have dimensions at the limit of the spatial resolution, and their electron density values are within the partial volume effect tail of the kerogen curve.

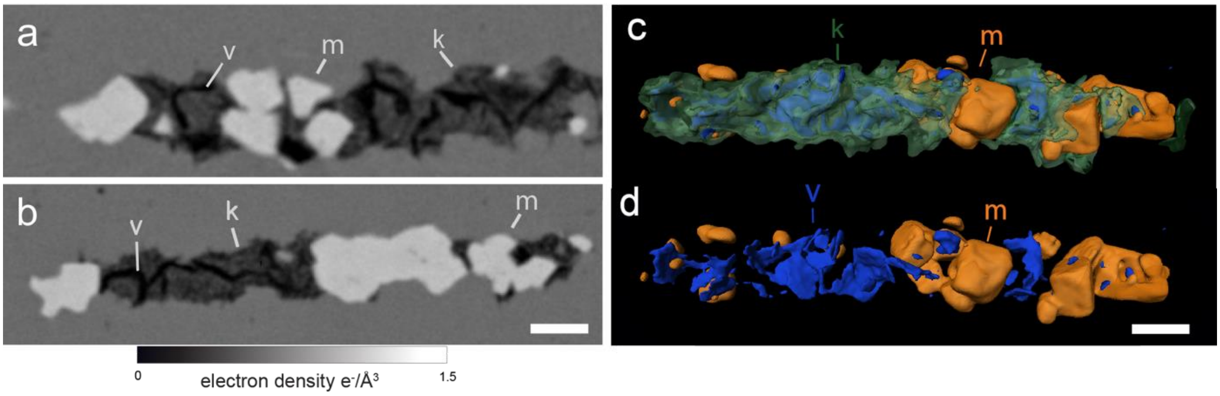

Figure 30 - **a,b,** Details of tomographic virtual slices showing two different fossil filaments within the silica matrix. They are mostly composed of an irregularly distributed kerogenous material (k). Fracture voids (v) are visible within the kerogen, indicating a high maturity and brittle behavior. The irregular aspect of the kerogen probably results both from Ostwald ripening of the impregnating silica and brittle deformation with void formation. Higher density maghemite crystals (m) are present as euhedral and anhedral crystals. **c,** 3D detailed segmentation views of a filament showing maghemite crystals with cubic and octahedral morphologies, and the kerogen (semi-transparent green) with interior fracture voids. **d,** internal view of the kerogenous region present in **c** showing the distribution and shape of the fracture voids (blue). Scale bar 1 μm.

Source: By the author.

The iron oxides are distributed heterogeneously along the filaments and the calculated density is 4.83 ± 0.08 g/cm^3. Although this mineral has been previously described as secondary hematite (85,87) this density is inconsistent with the density of this mineral also with and magnetite (Table 1). It is, however, consistent with the presence of the less common iron oxide maghemite (γ-Fe_2O_3). Our nanometric spatial resolution allows virtual 3D rendering of the euhedral crystals and reveals their octahedral and cubic morphologies, further corroborating this interpretation.

4.1.2 MASS DENSITY QUANTIFICATION AND GEOCHEMICAL INTERPRETATION

Table 1 - Phases of compounds identified from the samples of Mink Mountain locality of the Gunflint Formation based in the calculated mass densities.

Candidates	Mass density (g/cm^3)	Reference material	Reference mass density (g/cm^3)
Silica	2.69 ± 0.06	Quartz	2.65
Kerogen	1.43 ± 0.45	Mature kerogen	1.25 - 1.77
Maghemite	4.83 ± 0.08	Hematite	5.24
		Magnetite	5.18
		Maghemite	4.87

Reference minerals source: www. mindat.org (112)

Source: By the author

4.1.3 TAPHONOMIC IMPLICATIONS

The presence of kerogen of high-density with the presence of fracture voids supports previous studies that estimated high diagenetic temperatures of 210–230°C for this locality. (19) The persistence of these fractures further indicates that kerogen metagenesis occurred post-diagenetically, after the infiltration of fluids, such as the iron-rich groundwater that probably percolated the rocks when they were still porous. (87) These soluble ferrihydrites (iron oxide-hydroxides) probably adhered to the carbonaceous material, further compressing it while growing into larger crystals of maghemite. The heterogenous distribution of these maghemite crystals, the presence of small crystals adhered to the kerogen and the lack of crystals completely surrounded by kerogen (Figure 30) supports this interpretation over the biogenic hypothesis for this iron oxide. (85)

The identification of maghemite rather than hematite, which was further supported by magnetic analysis (Extended data 4,5 from Appendix), also provides a new comprehension of the taphonomic processes involved in the preservation of microfossils from this locality and highlights its uniqueness taphonomy of microfossils when compared with the typical preservation of carbonaceous microfossils from other localities. Maghemite can be formed directly from iron hydroxide (ferrihydrite) precursors in environments with high amounts of organic ligands and high P/Fe ratios. Conversely, when ligand concentrations are low, the metastable maghemite phase is not formed and haematite is the product of ferrihydrite transformation. (101-102) This indicates that the presence of organic material – in this case of biogenic origin – and its maturation with release of organics drove a localized taphonomic pathway of the iron oxides at the micron-scale. This is markedly different from the taphonomy of the formation in general, where the organics were present in lower concentrations resulting in haematite as the dominant mineral and hindering the detection of maghemite by conventional techniques, such as bulk X-ray diffraction. (85)

4.1.4 DISCUSSION ON BIOGENICITY CHARACTERS

Despite the fact that the kerogenous material is not defining the cell walls of the filaments such as in other localities of the Gunflint Formation (20), the diameter of the kerogenous component is homogeneous at the micron-scale in all observation planes and along the full extent of the filaments, which is consistent with a biotic morphology. The density of this organic compound is also an important biogenic character, since it can exclude the possibility of crystalline graphite or the condensed Fischer Tropsch-type carbonaceous material formed in hydrothermal settings. Those are abiotic carbonaceous material that commonly lead to controversial interpretations of putative biogenic structures. (24-25,40,103) Moreover, the thermal maturity of the kerogen supports its singenicity with the host rock, discarding hypotheses of more modern contaminants.

4.2 SCHREIBER BEACH LOCALITY OF THE GUNFLINT FORMATION

The spatial resolution was obtained for GF1, GF2 and GF3 are, respectively: 58.8 nm, 46.7 nm, 56.0 nm. GF 1 and GF2 have pixel sizes of 28.53 nm and GF3 of 35.11 nm. Some artefacts due to sample preparation were observed for the samples GF1 and GF2 and will be discussed in detail in section (4.2.4).

Only one phase of material, less dense than silica, was observed to be composing the fossil specimens of the three samples. Although iron minerals have been previously described in specimens from this locality (20,90), no other mineral with density higher than silica was observed in any of the samples. If present, any of these minerals should be smaller than our obtained spatial resolutions and could not be resolved by PXCT.

4.2.1 DESCRIPTION OF THE MORPHOLOGICAL FINDINGS

Sample GF1

Several microfossils of different morphologies could be distinguished (Figure 31) within the sample. The morphotypes that can be distinguished are: six thin filaments (0.9 > 1.5 μm) and one thick (~ 4 μm) (see Table 2 for morphometric details), at least eight small spheroids (~ 1μm), two medium size spheroids (~2 to 3 μm) and one complex structure composed of one large spheroid surrounded by smaller spheroids.

An interesting aspect to notice is that, when observed from the lateral view, the filaments seems to display a common orientation towards an up-diagonal direction (Figure 31) relative to the sample. This orientation, similar to the axis of the microscope depth focus, is difficult to be evaluated by petrographic analysis. The orientation of filaments is a characteristic typical of photosynthetic community, and its absence for the filaments of Gunflint Formation has already been used as an argument against their photosynthetic nature. Although the orientation of biofabrics can be evaluated in macroscopic and microscopic analysis, irregularities caused by the three-dimensionality of the mat might happen at local scales, and when directed towards the microscope depth focus, might not be perceived. The orientation of all the six filaments in our sample is in agreement with the hypothesis of a photosynthetic community.(116)

As listed in section 1.1 a preferential orientation of filaments for being indicative of the formation of biofabrics is also considered an additional biogenic character. When the structures are not parallel to the plane of the petrographic thin section, 3D images would be required for observing this type of configuration. The evaluation of a relatively large area, *i.e.* covering a large number of specimens, is also necessary for probing such orientation patterns. This micron-scale orientation arrangements would be difficult to be probed by sole petrographic analysis as this would require the specimens to be (at least closely) oriented parallel to the thin section plane or within the focus depth of the lens, and impossible with electron microscopies.

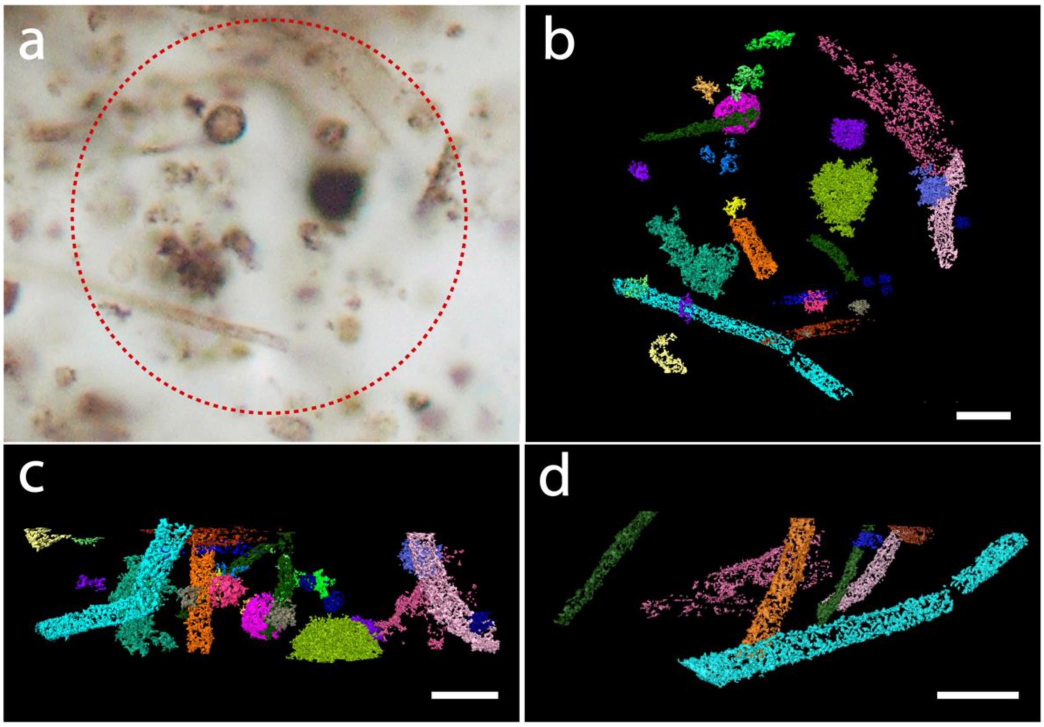

Figure 31 - Results of sample GF1. **a**, petrographic image of the area sampled. **b**, sample approximately in the same orientation of **a** showing that different specimens could be distinguished, some perpendicular to the observation plane, making their identification by petrographic analysis more difficult. **c**, lateral view of the sample showing the distribution of the specimens within the rock that has approximately 10 μm of high. **d,** only filaments rendered in 3D for showing their orientation towards an up-diagonal direction. Scalebar 5 μm.
Source: By the author.

The cell walls of the microfossils present a high degree of discontinuity. In 2D slices it is possible to see that they commonly show a “saw-tooth” morphology (Figure 34a,b, Figure 32a,c). These characteristics were observed in previous TEM studies and can be interpreted as a result of the rearrangement of the carbonaceous material by the recrystallization of amorphous silica into quartz crystals. (32-33) If the thickness of the cell walls is constricted by the quartz crystals to values below our obtained spatial resolution, they are not resolved and could also have led to the appearance of discontinuity.

For the filamentous specimens, the observed results display a good similarity with the 3D images of FIB-SEM analysis (32,49) which also showcased the discontinuity in the cell walls. With FIB-SEM, Wacey et al. 2012 also described hints of septation on filaments that could also be artefacts resulting from the gap between the FIB slices, thus hindering the identification of the specimen analyzed destructively. In our analysis, five filaments were distinguished in the sample GF1 (Figure 32,Figure 33), none of them containing internal traces of septa, but some containing periodical constrictions indicative of septation (Figure 32c). Is important to notice, still, that the discontinuous texture of the cell wall, when observed in 2D cross-sections close to the surface of the specimen, display a morphology that resemble septa (Figure 33c) and is very similar to the septation pattern observed in some specimen with petrographic analysis (see filament observed in Figure 5H for an example).This could lead to a misinterpretation on a 2D evaluation, for instance with a TEM slice or even a petrographic analysis. The presence of septation is a biogenicity character of filamentous fossils, and has been important for the interpretation of Archean structures such as the putative fossil filaments from Apex Chert (Figure 6). (25,46)

In terms of taxonomic affiliation, sheath-like filaments with no septation are classified as *Siphonophycus,* while the septate ones are classified as *Gunflintia.* (31-32,105) Morphometric analysis of the filament's widths (Table 1), revealed the presence of at least four morphometric distinguishable species.

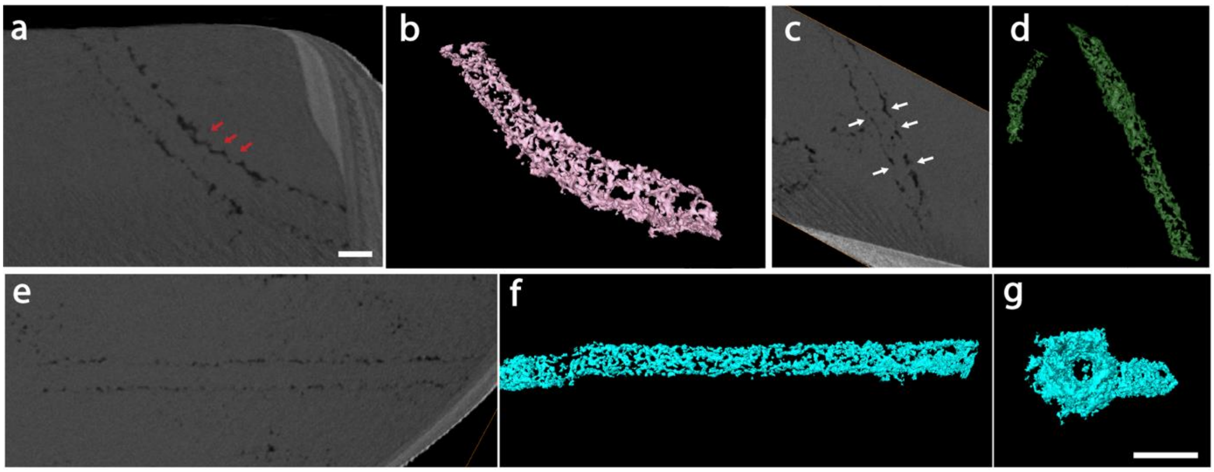

Figure 32 - Filaments present in the sample GF1. **a**, a “saw-tooth” morphology is visible in the filament (red arrows) that has a width of 1.50 ± 0.13 μm and is rendered in 3D in **b**. This pattern suggests a taphonomic alteration but traces of septation cannot be discarded. **c,** Thinner filament, with 0.90 ± 0.11 μm of width showing traces of a constriction pattern indicative of septation (white arrows). **d,** 3D rendering of the filament shown in **c** and a second similar one in the back of the plane (looking thinner due to the perspective). The septation and width is consistent with the genus *Gunflintia*. **e**, **f**, Filament with 1.23 ± 0.05 μm of width and no trace of septation, which is confirmed in the hollow view observed in the transversal section in **g**. The lack of septation is suggestive of the genus *Siphonophycus.* All images are in the same scale, except for **g.** Scale bar 1 μm.

Source: By the author.

Table 2 - Width (in μm) of filaments from Gunflint Schreiber Beach obtained by morphometric analysis of the PXCT data.

GF 2	GF1				
	green (Fig. 32c,d)	light blue (Fig.32f,g)	orange (Fig. 33)	light prink (Fig.32a,b)	dark pink (Fig. 31)
0.99 ± 0.05	0.90 ± 0.11	1.23 ± 0.05	1.42 ± 0.16	1.50 ± 0.13	3.98 ± 0.34

Source: By the author

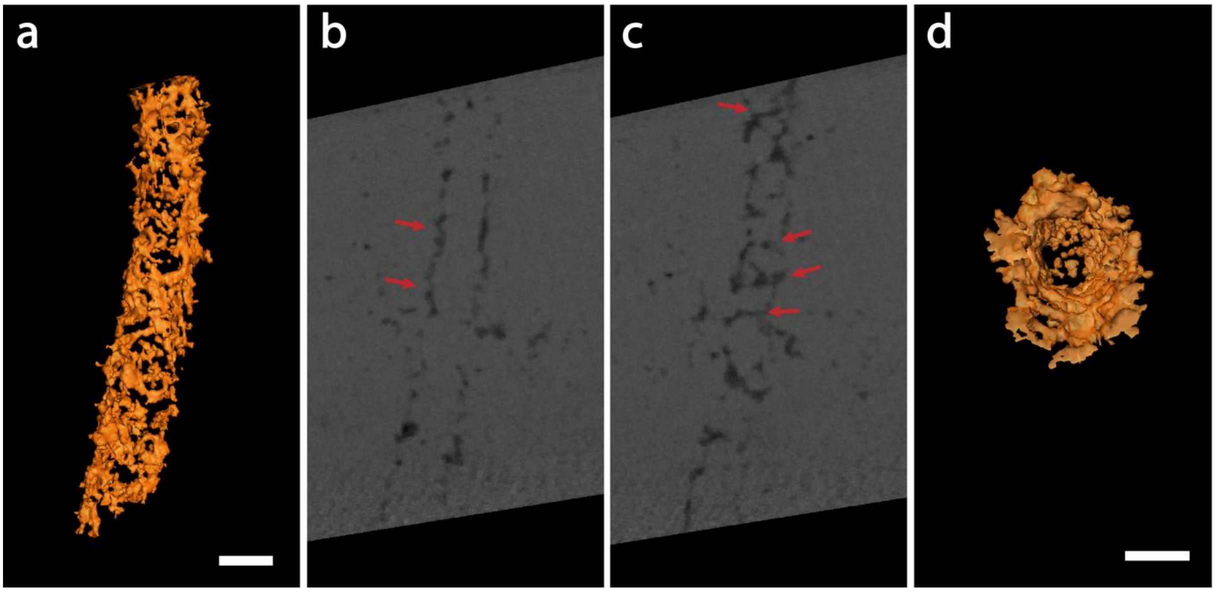

Figure 33 - Filament from sample GF1. **a,** 3D rendering showing a non-continuous, irregular wall. **b,** detail of a longitudinal section in the center of the specimen showing an irregular patter with saw-tooth-like morphology (red arrows), but no inner traces of septation. **c,** longitudinal section close to the edges showing a "septa-like" pattern (white arrows), similar to what is commonly observed in petrographic analysis. d, transversal section showing a hollow space with traces of carbonaceous material. Scalebar 1μm.
Source: By the author.

From the spheroidal specimens classified as *Huroniospora,* the best preserved one is showed here in detail in Figure 34. It has a diameter of 3.4±0.2 μm and when observed in 2D it presents the already mentioned "saw-tooth" morphology typical of kerogen displacement during quartz crystallization. The 3D rendering revels a structuration of the kerogenous material forming an wall reticulation similar to the species described in Figure 5 as *Huruniospora macroreticulata.* This wall reticulation was first observed by visible light microscopy and used to argue against a cyanobacteria origin. (116) Further TEM analysis denoted the features of kerogen displacement by quartz and reinterpreted these features as diagenetic alteration. (20) Our 3D results show that the holes in the wall have different sizes and are irregularly distributed across the spheroid, corroborating this interpretation.

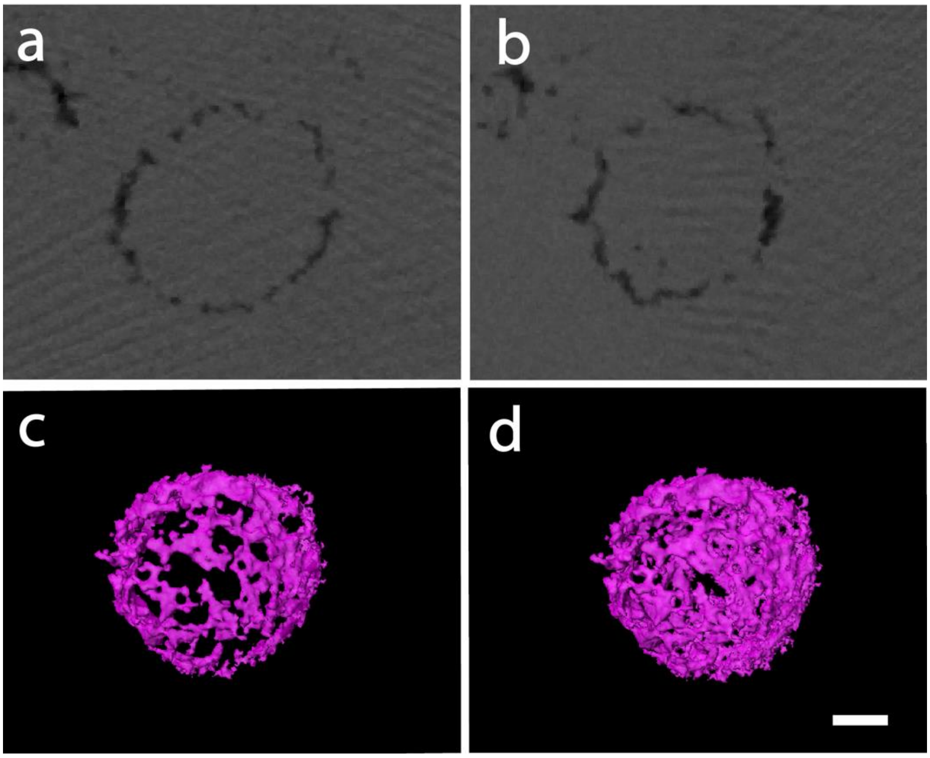

Figure 34 - Microfossil identified as *Huniospora.* **c,** 3D rendering after removal of the structures in the back of the fossil to make it easier the observation of the cell wall structure. The reticulation pattern is similar to what is observed in the specimen of *Huroniospora macroreticulata* of Figure 5 G. **d,** the complete view of the specimen shows the irregularity of the holes, corroborating the diagenetic hypothesis. Scalebar 1 μm.
Source: By the author.

One microfossil was in the bottom of the sample and only about half of its full diameter was imaged (green in Figure 31c). It is composed by a large spheroid (~3 μm) surrounded by smaller (< 2 μm) tubercle-like spheroids of variable dimensions (Figure 35). This pattern of association of spheroids is similar with the morphology of the genus described as *Eosphaera* (31) (see Figure 5 A,B), although our specimen's diameter is significatively smaller (~ 8μm versus 30 μm described). These species are the most ancient complex microfossil and has no extant comparable form. It has been evaluated in detail by FIB-SEM(49), which also confirmed the presence of a thinner (~ 100 nm) outer wall surrounding the spheroids. The specimen we have analyzed presents no traces of external wall. The possible explanations for this observation are: the thinner wall was present and has been lost during the fossilization process; the wall is present but is thinner than the obtained spatial resolution (58.8 nm) thus could not be resolved; or this specimen is not an *Eosphaera,* but a different genus that comprises smaller specimens lacking outer walls. To the present date we do not know if it belongs to an already described group or if it comprises a new genus.

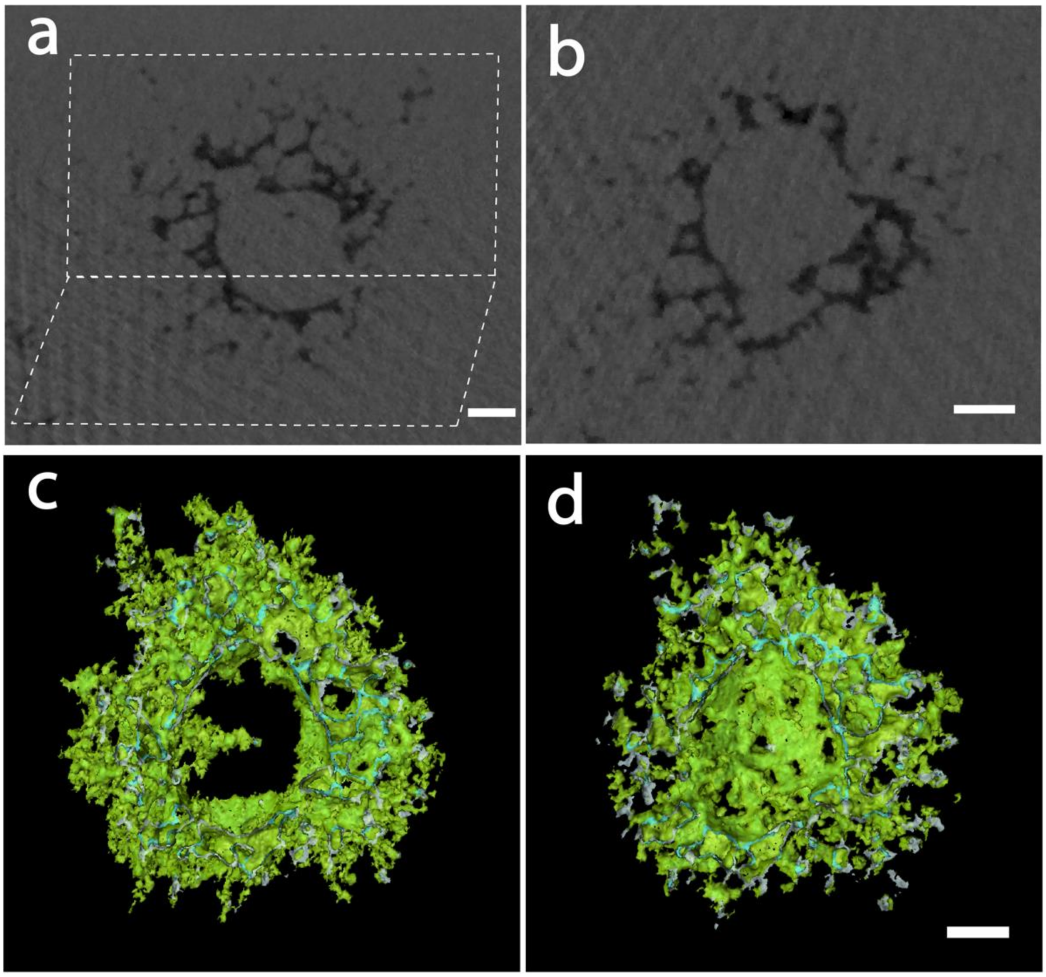

Figure 35 - Microfossil with a structural pattern similar to *Eosphaera* **a,** intersection of 2 tomographic images in different planes (indicated by the dashed lines) showing the presence of tubercular small spheroids of different sizes in both planes. **b**, detail of the distribution of tubercular spheroids surrounding the larger one. **c**, 3D rendering of a section of the specimen for showing its hollow aspect forming a larger spheroid. **d**, 3D rendering of the complementary part presented in **c** showing the "bottom" of the specimen, with the closing of the spheroid. Small wholes represent the areas where the tubercular spheroids are attached. The darker green in **c,d** shows the interior faces of the 3D surface exposed by its sectioning. Some spheroids can be distinguished, but their discontinuous walls generate a "cloudy" appearance in 3D. Scalebar 1 μm.

Source: By the author.

Sample GF 2

The sample GF 2 was prepared not with a perfect cylindrical shape and had traces of platinum, which was used for the attaching of the rock in the tomographic pin. This resulted in image artefacts, discussed in detail in section 4.2.4.

Several regions with sparse concentration of kerogen were observed within the sample, but most of them with a high a degree of discontinuity, making it difficult their identification. Only one filament could be completely reconstructed in 3D (Figure 36), but fragments of other filamentous specimens were also distinguished (rendered in green). Similar to the specimens from sample GF1, the filament observed is also oriented towards an up-diagonal direction.

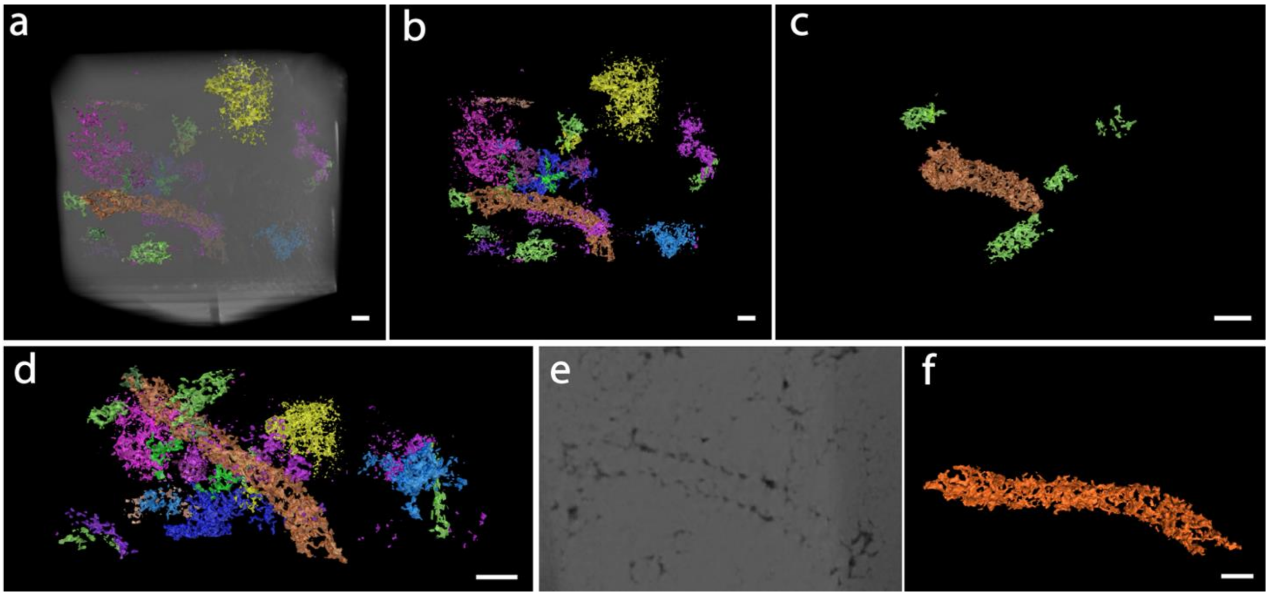

Figure 36 - PXCT results for sample GF2. **a,b** top-view of the square-like sample with fossils distributed inside. A filament is distinguishable, but the other specimens present a high degree of wall discontinuity, hindering their interpretation. **c**, detail of the filament complete (orange) and traces of incomplete smaller filaments (green). **d,** lateral view of the sample showing the filament oriented up-diagonally and the other incomplete, indistinguishable specimens. **e,** 2D section of the filament rendered in 3D in **f**, showing the saw-tooth morphology and no internal septa. Scalebar 1 μm.

Source: By the author.

Although this sample is a spot from the same region as sample GF1, the microfossils cannot be well visualized, probably due to sample preparation artefacts, highlighting the importance of this process for the quality of the obtained results.

Sample GF3

The results of sample GF3 showed a sampling shift in relation to the area of interest (Figure 37). This was probably caused by misalignment of the visible light and SEM micrographs during the selection of the spot to be FIB-milled.

All the specimens were localized at the edge of the pillar and were thus sectioned. This sectioning, plus the discontinuity of the kerogenous materials, made it difficult the identification of the specimens and their proper evaluation. No additional information was obtained on this sample.

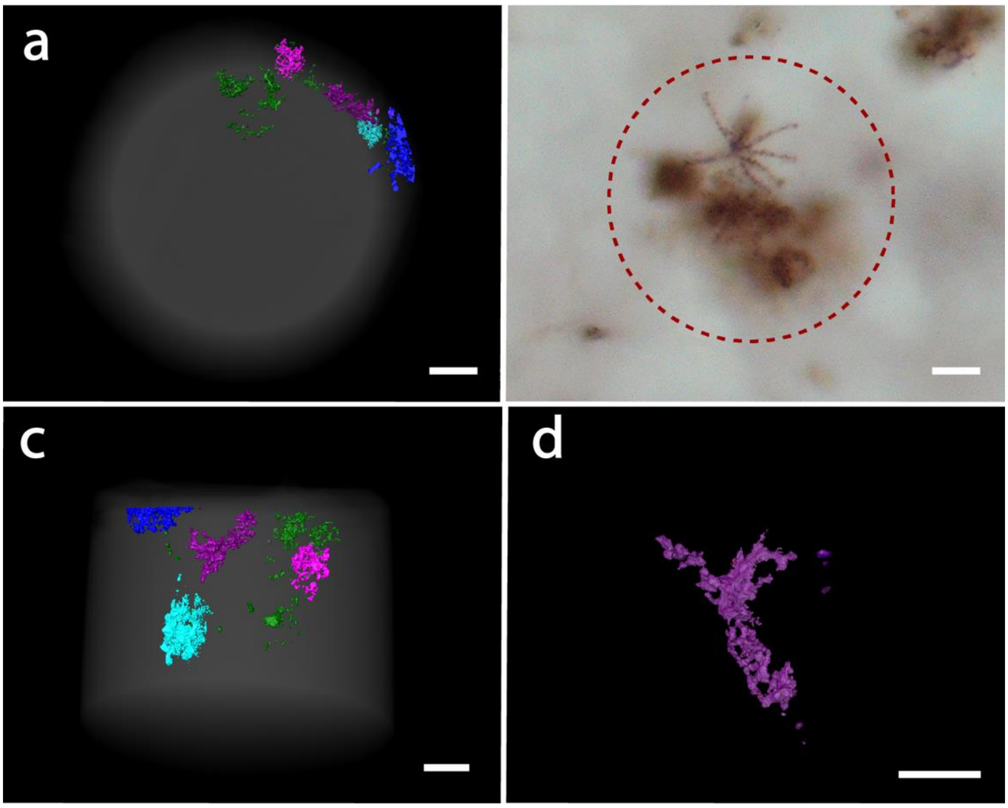

Figure 37 - Result of Sample GF3. **a, b,** top view of the sample showing the specimens distributed in the corner of the pillar. The sampling area is shifted in comparison with the desired area show in **b**. The sectioning of the microfossils and their discontinuous morphology hinders a proper identification. **c,** lateral view of the sample showing the specimens depth distribution. **d,** microfossils showing projected structures with some resemblance with *eoastrion* (star-like specimen shown in **b**). Scalebar 3 μm.

Source: By the author.

4.2.2 MASS DENSITY QUANTIFICATION AND GEOCHEMICAL INTERPRETATION

The segmented material of sample GF1 was used for the calculation of the mass density of the kerogenous material. Although most of the fossils were composed by thin features, the shrinking and smoothing procedure allowed the removal of the mixture phases and the quantification of the material in the center of the larger masses of kerogen, where the histogram showed no partial volume effect. Materials within the region affected by sample artefacts where not used for the analysis.

The mass density obtained for kerogen is 1.51 ± 0.21 g/cm^3, a density consistent with kerogen of high thermal maturation, and inconsistent with any iron mineral, which, as previously explained, could be expected to be involved in the fossilization of these structures, and also with abiotic carbonaceous materials as amorphous graphite. The possibility of influence of silica towards a higher density range cannot be fully excluded due to the small diameter of the carbonaceous structures. However, even the lowest densities within the estimated range is still consistent with mature kerogen (*i.e.* higher than 1.25 g/cm^3 (109)).

Table 3 - Phases of compounds identified from the samples of Schreiber Beach locality of the Gunflint Formation based in the calculated mass densities.

Candidates	Mass density (g/cm^3)	Reference material	Reference mass density (g/cm^3)
Silica	2.67 ± 0.09	Quartz	2.65
Mature Kerogen	1.51 ± 0.21	Kerogen	1.19 - 1.77

Reference minerals source: www. mindat.org (112)

Source: By the author

4.2.3 DISCUSSION ON BIOGENICITY CHARACTERS

The results obtained for Gunflint Schreiber beach are important for the discussion of the type and variety of biogenic characters that can be accessed with PXCT. Several characteristics observed on these *bona fide* microfossils comprise biogenicity criteria which can be explored in the evaluation of other structures:

- discrimination of filaments orientation within the micron-scale. This characteristic is indicative of biofabrics and can support biogenicity claims;

- discrimination of surface textures of filaments that in 2D images resemble septa. The presence of septation is a biological character for filamentous structures and the misreading of surface textures can lead to erroneous biogenic interpretations;

- morphometric analysis of width (and additionally other of volume, shape and cell-wall width that are also possible) can be made in 3D, providing more robust results for the whole specimens;

- discrimination of biological textures from taphonomic alterations such as kerogen reorganization is important for distinguishing *bona fide* microfossils from common artefacts of rearrangement of abiotic carbonaceous material, such as volcanogenic pseudo-fossils (41);

- mass density quantification allows the discrimination of kerogen from denser materials as abiotic amorphous graphite. The maturity of kerogen can also be important for distinguishing it from immature kerogen later contaminations;

4.2.4 SAMPLE ARTEFACTS

The samples GF1 and GF2 were the only ones that had residues of platinum from the FIB manipulation and attachment on the tomographic pin. The residues influenced considerably the quality of the final images (Figure 38). The fact that this material has a density considerably higher than the rock (more than 19 g/cm^3) lead to the generation of tomographic reconstruction artefacts in the images. This can be clearly seen as a darker region in the bottom of the samples that is perfectly correlated to the height of the platinum residues. In sample GF1 from the top view it is possible to see white and dark stripes irradiating from the platinum at the border of the sample (Figure 38b).

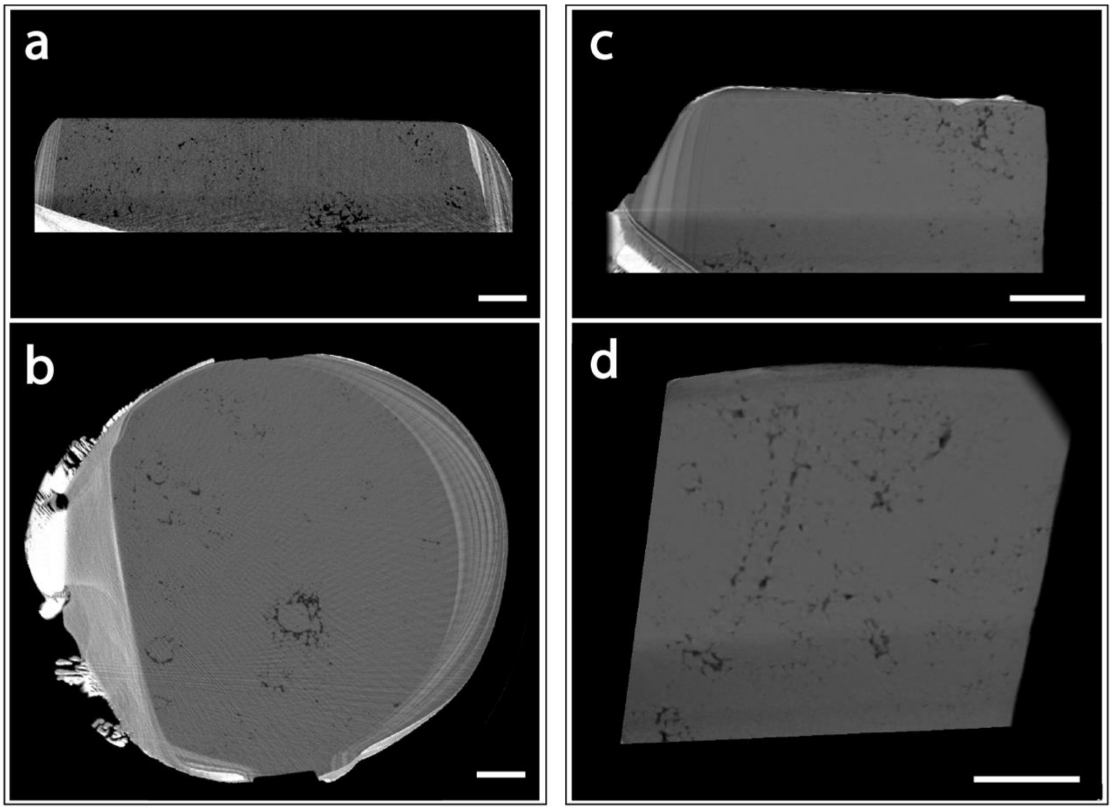

Figure 38 - Artefacts from sample preparation. **a**, Lateral view of samples GF1 showing the influence of the platinum outside the sample that generates a darker region within it. **b,** top-view showing the stripes artefacts irradiating from the platinum. **c,** Lateral view of sample GF2 showing the same darker region of **a** caused by the outer platinum. **d,** diagonal section of GF2 showing the filament and other indistinguishable fossils within the sample, some within the darker region. Scalebar: 3 μm.

Source: By the author.

The geometry of the samples is also an important aspect. The sample GF1 presented irregularities in the circular shape due to a displacement of the sample during the milling. This irregularity can be seen as round stripes surrounding the sample

(Figure38a,b). The light color of the stripes is probably due to the accumulation of gallium used for the FIB milling in these rims created in the sample. Although this artefact did not propagate through the sample, it added difficulties for the segmentation of features. For sample GF2, there are no visible artefacts resulting from the square-like morphology. The worse quality of the images, and difficult evaluation of fossils if compared to the fossils on sample GF1, which was extracted in the same region, could suggest a negative influence of this geometry for the final images.

These results highlight the importance of the sample preparation for the obtainment of good quality of data.

4.3 DRAKEN FORMATION

The 3D resolution obtained for sample DK1 and DK2 was 62.5 and 51.0 nm and the pixel size 28.53 nm and 35.11 nm respectively. The two samples revealed microfossils with walls composed of only one material phase but with significative morphological differences. No sub-cellular structures were observed despite the high-resolution achieved, confirming their low potential of preservation compared to the cell wall. For sample DK1, the material observed in the petrographic images, which might correspond to collapsed cytoplasm, was not sampled and could not be deeper investigated (Figure 39).

4.3.1 DESCRIPTION OF THE MORPHOLOGICAL FINDINGS

Sample DK1

The volume extracted by FIB-SEM was revealed to be shifted in comparison with the desired area selected by visible light microscopy (Figure 20).

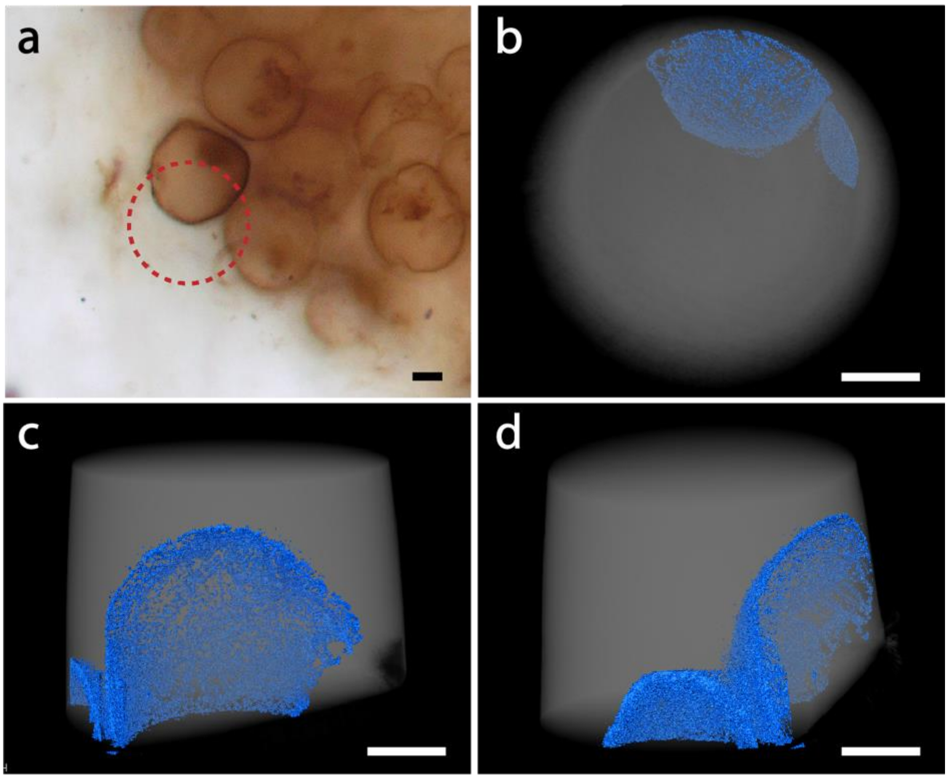

Figure 39 - Sample DK1, microfossils from Draken Formation. **a,** Photomicrography of the colonial specimens by visible light microscopy, with the circle indicating the region that was sampled by FIB-SEM, shifted in relation to the desired region shown in Figure 20. **b,** 3D rendering of the sample DK1 with the specimens in the same orientation as seen in **a. c,d,** Lateral views of the specimens, located in the bottom corner of the rock sample, and only partially sampled. Scalebar 5 μm.

Source: By the author.

This shift was probably due to a misalignment of the visible light and SEM micrographs during the selection of the spot to be FIB-milled. Inside the cylinder it is possible to identify parts of the cell walls of two specimens identified as *Myxococcoides* (Figure 39).

The sample is composed basically of two material phases. The matrix has a density of 2.68 ± 0.06 g/cm^3, consistent with quartz (2.65 g/cm^3). The fossils are composed by non-continuous lower-density cell walls with the intra-cellular space completely filled by silica. Previous studies have described that these cell walls are composed of kerogen. (18,117) This structure has a thickness of 191 ± 25 nm, and no apparent ornamentation or ultrastructure. This thickness is homogeneous in all observation planes. Granules with the same intensity of the kerogen that comprises the cell walls can be observed distributed all over the sample, also within the intracellular space. This can represent collapsed cytoplasm and/or remains of cellular degradation.

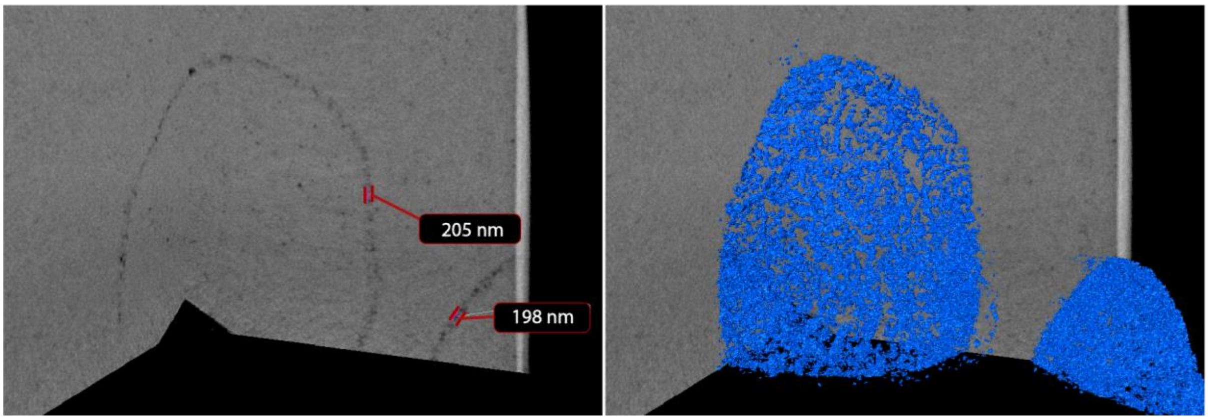

Figure 40 - Sample DK1. **a**, Morphometric analysis of the cell wall showing a width of 191 ± 25 nm and **b,** 3D overview of the cell walls showing the non-continuous preservation of the kerogen which comprises these structures.
Source: By the author.

The small dimensions of these kerogenous structures lead to a strong partial volume effect (Figure 41) which hinders the quantification of their mass density. This problem is described in detail section 3.5.1

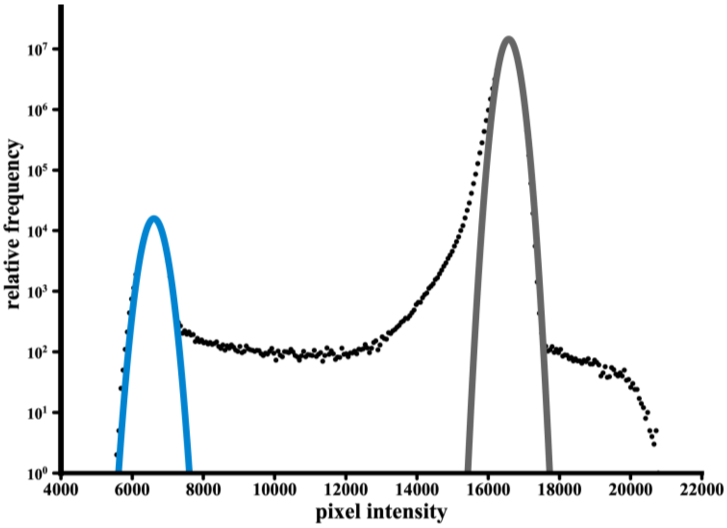

Figure 41 - Histogram of pixel intensity of DK1 with gaussian fits corresponding to air (blue) and silica (grey) phases. The kerogen phase is not visible due to the partial volume effect observed in the left side of the silica curve (see Figure 27).
Source: By the author.

The minimum value of mass density estimated for this material is 1.5 g/cm^3. This is within the density of mature kerogen (1.35 g/cm^3 to 1.77 g/cm^3).(107,109) Foucher and Westall 2013 described the presence of amorphous (opaline) silica associated with the kerogen on specimens from this locality. This microcrystalline form of silica is described as precipitating onto the organic molecules. This process can explain the fragmentation of the cell wall in small granules. Moreover, since the density of this material is lower than of crystalline silica (*i.e.* quartz), and higher than kerogen, the mixture of the carbonaceous cell wall with opaline silica could also be contributing to the strong partial volume effect observed in the histograms of this sample (Figure 41).

Sample DK2

The isolated specimen DK2 was completely immersed in the cylinder of rock. A crystal of higher density was present above the cell and comprising its wall, and in contact with the surface of the rock (Figure 42).

The specimen has a clear spherical form of approximately 15 μm of diameter but is slightly compressed in the lateral direction in respect to the cylindric sample (Figure 42d). The only biological structure preserved is the cell envelope, but granules probably from degraded cytoplasmatic material are also present. (Figure 42f). Similarly to the sample DK1, is its composed by non-continuous fragments of a low density material, consistent with previous descriptions of kerogen. (18,118). f). Similarly to the sample DK1, is its composed by non-continuous fragments of a low density material, consistent with previous descriptions of kerogen. (18,117)

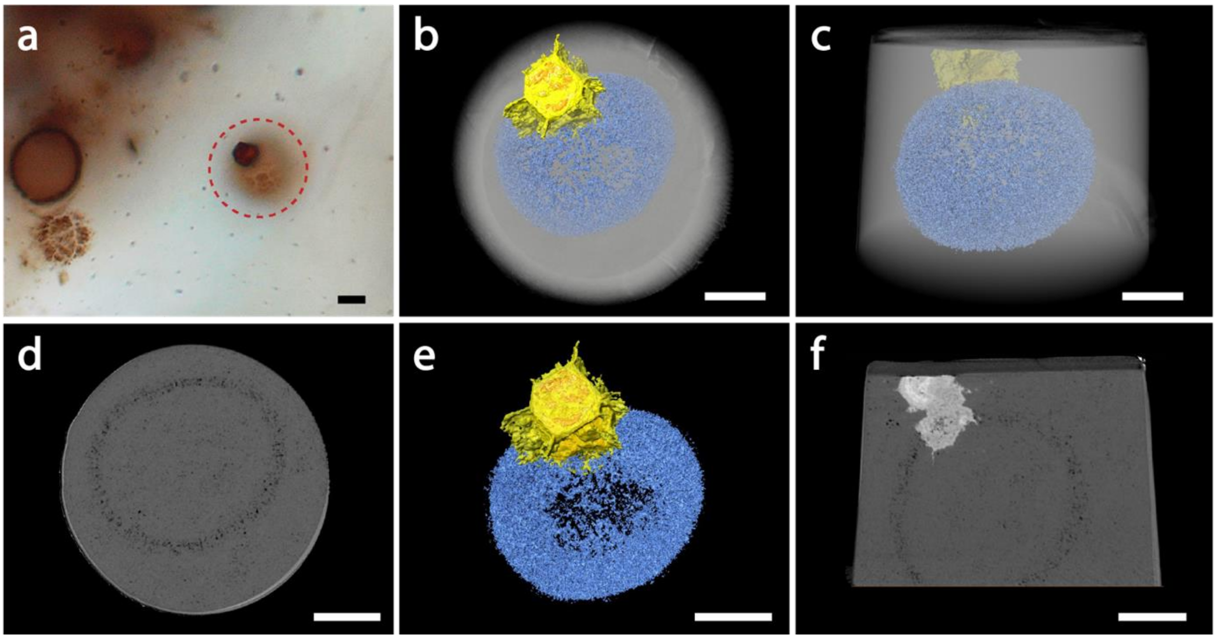

Figure 42 - Sample DK2. **a**, Petrographic visible light micrography showing the texture of the cell wall and the crystal in the top. **b,c,** 3D renderings of the cell within the rock pillar, top and lateral view respectively. **d**, 2D slice showing the top view of the fossil wall composed of discontinuous, micro-structured kerogen. **e**, same view of image **b**, but without the rock volume for showing the discontinuous texture of the cell wall in 3D. **f,** 2D slice showing the lateral view of the fossil and localization of the high-density crystal. The kerogenous wall is distinguished within the crystal. Scalebars 5 μm.

Source: By the author.

The ultrastructure of the cell wall of this specimen differs significantly from the specimens of the sample DK1. Morphometric measurements revealed a cell wall thickness of 1.1 ± 0.1 µm. This thick cell wall and granular appearance are consistent with the interpretation of Knoll 1982 as the species *Myxococcoides cantabrigiensis.* Although this structure is fragmented and granular at the nanoscale, it is possible to observe in some regions that there is a structural organization forming linear features oriented radially (Figure 43).

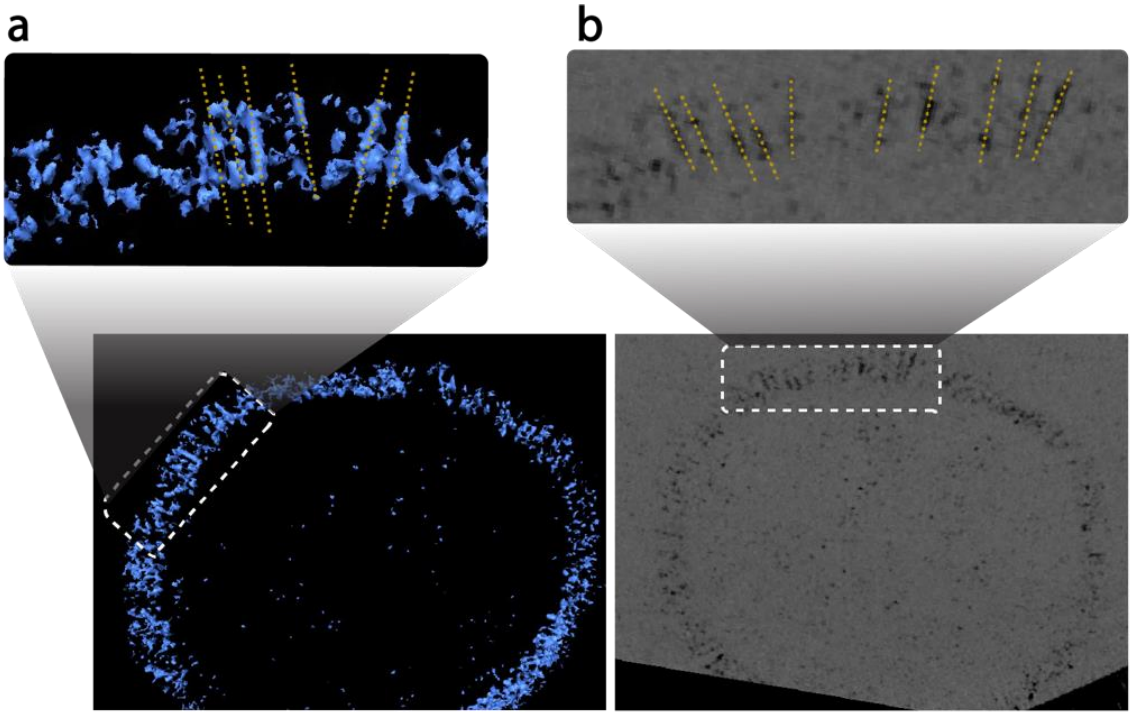

Figure 43 - Details of the cell compartment of the sample DK2 showing the presence of aligned structures oriented radially. Yellow dashed lines are used for highlighting these structures and indicating their orientation for **a,** 3D rendering of a region of the segmented cell compartment and **b, a** tomographic slice.

Source: By the author.

Previous works have debated if the preserved envelope of *Myxococcoides cantabrigiensis* corresponded to a cell wall or extracellular sheath (91,118), and they have used thickness measurements and granular morphology for a cell wall interpretation. Our results of morphometry and 3D granular texture corroborate these interpretations. Moreover, the revealed ultracellular orientation represents an additional support to this interpretation since extracellular sheaths have smooth textures with no expected structuration. (118)

4.3.2 TAPHONOMIC IMPLICATIONS

Sample DK2

The crystal visible in the visible light micrography was also observed in the PXCT images (Figure 42). This crystal lies above the cell wall and has a higher intensity, and consequently density, than the silica matrix. It is composed by at least 3 recognizable phases. Isolated crystals of pyrite are commonly found related to specimens from this locality (18,91). However, the estimated density and morphology of this crystal are inconsistent with the interpretation of pyrite.

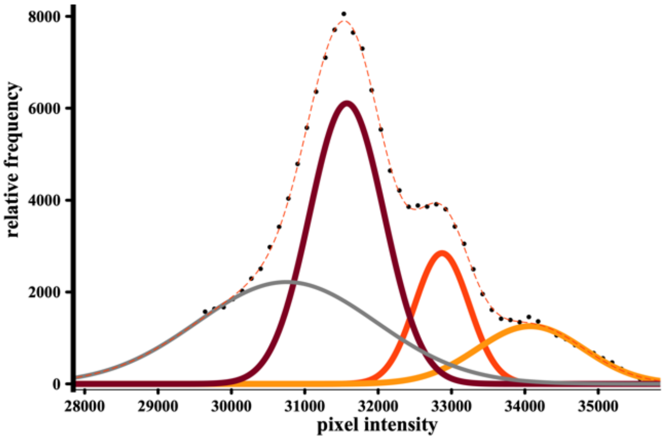

Figure 44 - Intensity histogram and fitting of the crystal showing three material phases (colored gaussians). The grey curve represents the partial volume effect occurring in the region of the borders of the mineral. The bordeaux curve represents the phase 1, the orange curve represents the phase 3 and the yellow, broad curve, probably includes the phase 2 and the higher density material of phase 3 (see Table 4).

Source: By the author.

The mineral phase referred as phase 1 (Figure 45a) is the one in direct contact with the fossil (blue renderings in Figure 45,Figure 46), engulfing part of the cell envelope. It is still possible to see the kerogenous features within it supporting the hypothesis that the microorganism might have produced the precursors for the formation of this mineral or that the organic structure partially degraded served as a nucleation site for its growth. The estimated mass density of this mineral is 3.30 ± 0.09 g/cm^3. It is composed by euhedral crystals with heterogeneous texture. The irregularities in the surfaces of this mineral might represent signals of dissolution. A mineral described in this formation which could be a candidate for this phase is hydroxyapatite, which has a density of 3.10 - 3.21 g/cm^3.

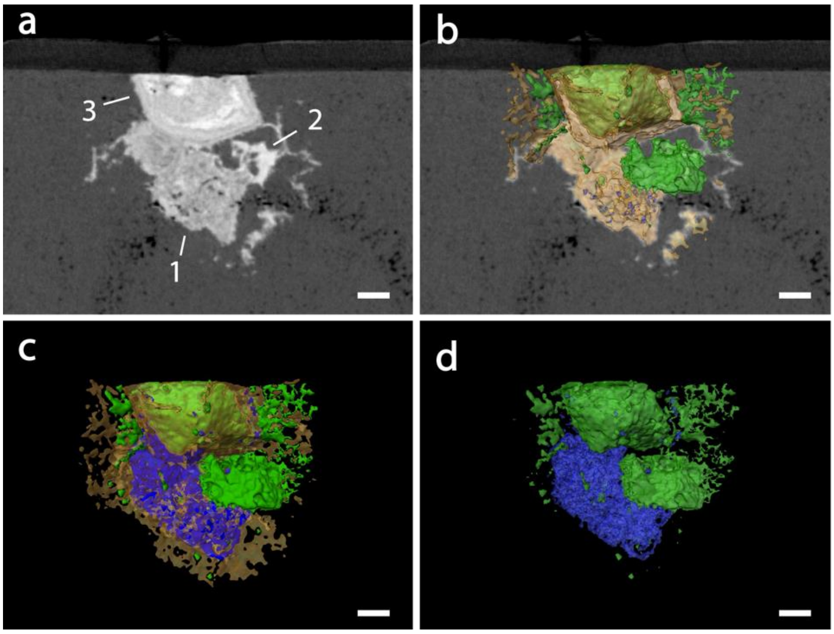

Figure 45 - Detail of the crystal showing the three mineral phases (numbered in a). All images correspond to the same observation plane. The Phase 1 is engulfing the cell wall, and has a heterogenous density, forming a spongy material (blue). The Phase 2 is the white material above the Phase 1 and has a more homogeneous and denser composition, with large euhedral porosity which could have been formed by the crystallization of quartz grains. This phase is rendered in green. The Phase 3 corresponds to the material at the top. It is composed by higher intensity nuclei which have linear growth marks and covered by a material less dense than the nuclei which is rendered in yellow. Since these nuclei have the same density than the Phase 2, it is also rendered in green. Ramifications in the crystals could represent remains of infiltration veins. Scalebar 1 μm.

Source: By the author.

The second identifiable phase is a small crystal of homogeneous intensity which lies between the other two phases. It has an estimated mass density of 3.61 ± 0.10 g/cm^3 and present large pores. These pores have sharp edges with trigonal morphology such as quartz crystals. This euhedral aspect of the porosity could indicate that this mineral phase was formed encompassing some amorphous silica, which posteriorly crystalized into quartz prior to the final crystallization of this mineral.

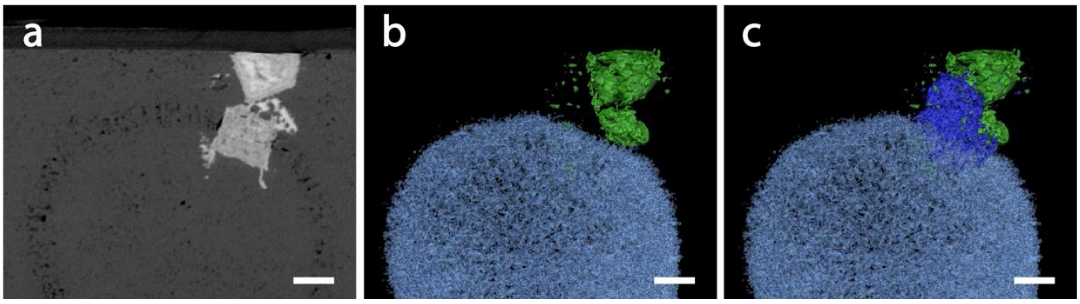

Figure 46 - Detail of crystal composed by 3 phases. Only the Phase 1 (blue in **b** and **c**) is in contact with the organic cell wall. Scalebar 2 μm.

Source: By the author.

The third distinguishable phase is the mineral closer to the surface. It is composed by nucleus with a mixture of lighter and darker materials which alternate forming layers similar to growth lines. The outer layer is more evident and darker than the rest of the mineral. Observing from the top orthogonal plane (Figure 47a), this mineral has a hexagonal shape, with variable vertices sizes. The 3D rendering shows surfaces of different dimensions, with no distinguishable polyhedral morphology (Figure 45c). This is probably because this mineral was formed by the junction of at least two growing nucleus, as can be seen in the (Figure 47a), where two separated nuclei can be distinguished, one having defined vertices forming a hexagonal shape. These nuclei are composed by a denser material with an average mass density of 3.61 ± 0.10 g/cm^3, similar to the density of the mineral phase 2. The outer layer, darker, has a mass density of 3.47 ± 0.05 g/cm^3. From the vertices of this mineral phase, thin webs of material irradiate. This material could represent remains of infiltration fractures.

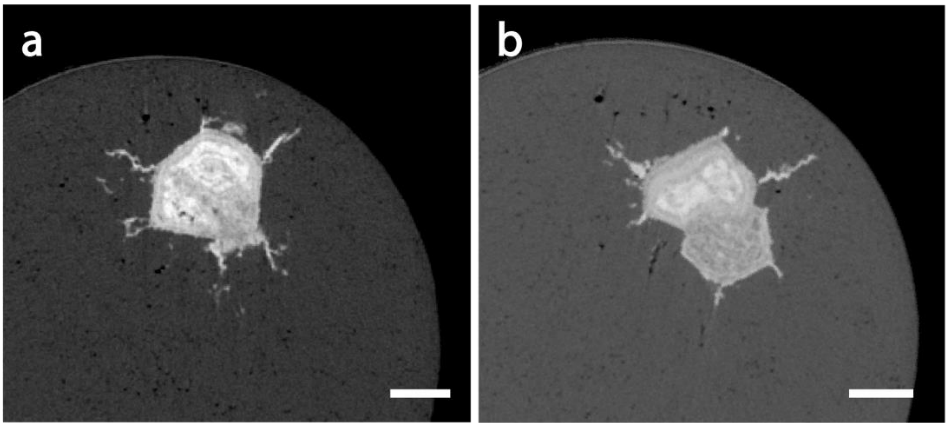

Figure 47 - Top view of the sample DK2. a, Two nuclei of high intensity can be identified within the crystal named as phase 3. One of these nuclei presents growth lines defining a hexagonal shape. b, View of the phase 3 with the two nuclei showed in a now merged. This mineral lies above the mineral phase 2, which has a heterogenous and lower density texture. Scalebar 2 □m.
Source: By the author.

The complex morphology and composition of this mineral hindered its clear interpretation until the present moment. Signs of post-diagenetic alteration, such as the growth lines, infiltration fracture remains, and euhedral crystal porosities illustrates the complexity of the taphonomic processes that happened in this formation. The identification of the mineral phases and their possible implication to the understanding of taphonomy of Draken Formation are future perspectives of this work.

4.3.3 MASS DENSITY QUANTIFICATION AND GEOCHEMICAL INTERPRETATION

Table 4 - Phases of compounds identified from the samples DK2 of Draken locality based in the calculated mass densities. The histogram of the corresponding phases is shown in Figure 44.

Material	Mass density (g/cm^3)	Candidate material	Reference mass density (g/cm^3)
Matrix	2.63 ± 0.03	Quartz	2.65
Phase 1	3.30 ± 0.09	Apatite (?)	3.10 - 3.21 g/cm^3
Phase 2	3.61 ± 0.10	(?)	
Phase 3	3.47 ± 0.05 3.61 ± 0.10	(?)	

Reference minerals source: www. mindat.org (112)

Source: By the author

4.3.4 DISCUSSION ON BIOGENICITY CHARACTERS

The biogenicity of the microbiota of Draken Formation is well accepted given its exceptional state of preservation and diversity. The features observed by PXCT consist of good representatives of features expected to be present in several Precambrian microfossils, *i.e.* silicified microbes with only a cell envelope preserved. Moreover, spheroidal structures represent a very simple morphology, challenging their attestations of biogenicity. For this type of structures, some characteristics observed in the cells from Draken are important biogenicity indicators which can be explored for other, possibly earlier structures:

- Presence of a distinguishable cell envelope or cell wall composed by a material less dense than silica, consistent with kerogen;
- Texture of the cell wall consistent with partially degraded organic material;

- Thickness of the cell wall biologically consistent;
- Thickness of the cell wall homogeneous in all 3D observation planes;
- Size, volume and shape of the putative microbe biologically consistent in 3D;
- Presence of ultracellular structuration of the cell walls.

The morphology and ultrastructure of the cell wall of these fossils also provides novel information important for the identification of the specimens and their paleoecology.

The difference in thickness and ultracellular organization of the cell wall of specimen DK1 in relation to the specimen DK2 clearly indicates that these correspond to different species of the genus *Myxococcoides.* The species *Myxococcoides cantabrigiensis* could be directly attributed to DK2 due to the characteristic thick (~ 1 μm) cell wall of this group. The ultrastructural organization of kerogen with a radial orientation, however, has not been observed so far. This feature can further be used to refine the taxonomic diagnosis of specimens attributed to this group, as long as helping on the interpretation of the group itself. The group *Myxococcoides* presents a disputed taxonomic affiliation between cyanobacteria and unicellular algae, and is so far considered an *incertae sedis.* (81-82)

Another possible interpretation possible for the wall differences between the specimens DK1 and DK2 is related to ecological habits of these species. The specimens DK1 present a colonial organization, which can provide a physicochemical protection against turbulences or changes in the medium. Meanwhile, the isolated specimens of *Myxococcoides cantabrigiensis* of sample DK2 are more susceptible to the conditions of the surrounding environment. A thicker cell wall could offer more protection and resistance to this specimen.

These results comprise important insights into morphological and ultrastructural differences that could be preserved in the Precambrian fossil record and can support the interpretation of isolated or colonial spheroidal structures.

4.4 BARBERTON GREENSTONE BELT

The following resolutions were obtained for the samples of BGB: HG1: 49.0 nm, HG2: 70.2 nm, KB1: 64.7 nm and KB2 58.7 nm. HG1 and KB1 have pixel sizes of 28.53 nm and HG2 and KB2 of 35.11 nm.

The PXCT images from the samples of BGB revealed a complex picture for both Hoogenoeg and Kromberg samples. Some features and minerals were present in both Formations, and their differences and similarities in the different samples provided clues for their interpretation.

4.4.1 DESCRIPTION OF THE MATERIAL PHASES

The material phases observed are summarized in Table 5 and are described below.

- Low density (dark), blob structures with a wide range of dimensions, from our detection limit (the spatial resolution and contrast with the surrounding matrix) up to few micrometers. They are commonly arranged in a parallelly paired disposition and are rendered in purple in the 3D images. The inner face of the pairs is regularly flat, while the outer varies in shape (Figure 54,Figure 48). Two hypotheses could explain this disposition: this material coated a tabular mineral post diagenetically; or initially single blobs were split in two parts by the secondary precipitation of a tabular mineral within them. The careful inspection of all the samples allowed the discovery of few blobs with a "horseshoe" morphology (Figure 48c, Figure 49b) suggestive of a recent disruption of the blob or even presenting a crystal of higher density inside (Figure 48d). These findings support the hypothesis of a primary origin of this material in respect to the secondary tabular minerals. The small size of most of these features hinder their electron/mass density quantification, but mass densities down to 0.32 ± 0.12 g/cm^3 were estimated within the larger ones (Table 5), suggesting that this material represents a non-solid phase. Their distribution, which in some cases outlines fractures (Figure 50), suggest that these blobs could be remnants of the material that filled these fractures. We interpret this material as of fluid inclusions.

- Tabular crystals slightly denser than silica, with morphology similar to minerals from the mica group of phyllosilicates and rendered in dark green in the 3D images.

Although present in all the samples, they vary in quantity, size and width, being larger in the Kromberg than in the Hoogenoeg samples (Figure 52Figure 54,Figure 55,Figure 57). The length of the crystals ranges from our detection limit up to ~ 8 μm. Some of the larger crystals present in samples from Kromberg are coated by a thin layer of a dark material, probably remains of the fluid inclusions described above. This finding supports the hypothesis that crystals of this tabular mineral probably grew within the blob materials, originating the paired features. When these minerals are of small dimensions and surrounded by the paired, dark features, they cannot be distinguished due to partial volume effect. The estimated mass density (~ 2.8 g/cm^3) and morphology is consistent with several minerals from the mica groups. The ones with consistent densities and already described in these formations are: muscovite (2.77 - 2.83 g/cm^3), biotite (2.8 – 3.4 g/cm^3) and chlorite (clinochlore 2.60 – 3.02 g/cm^3). (56,119) Calcite was also described to occur in veins of the BGB. (119) It can also present tabular morphology and has a density of 2.71 g/cm^3, close to the values observed.

The hypothesis for the formation of the low-density paired features and tabular minerals are outlined in Figure 51.

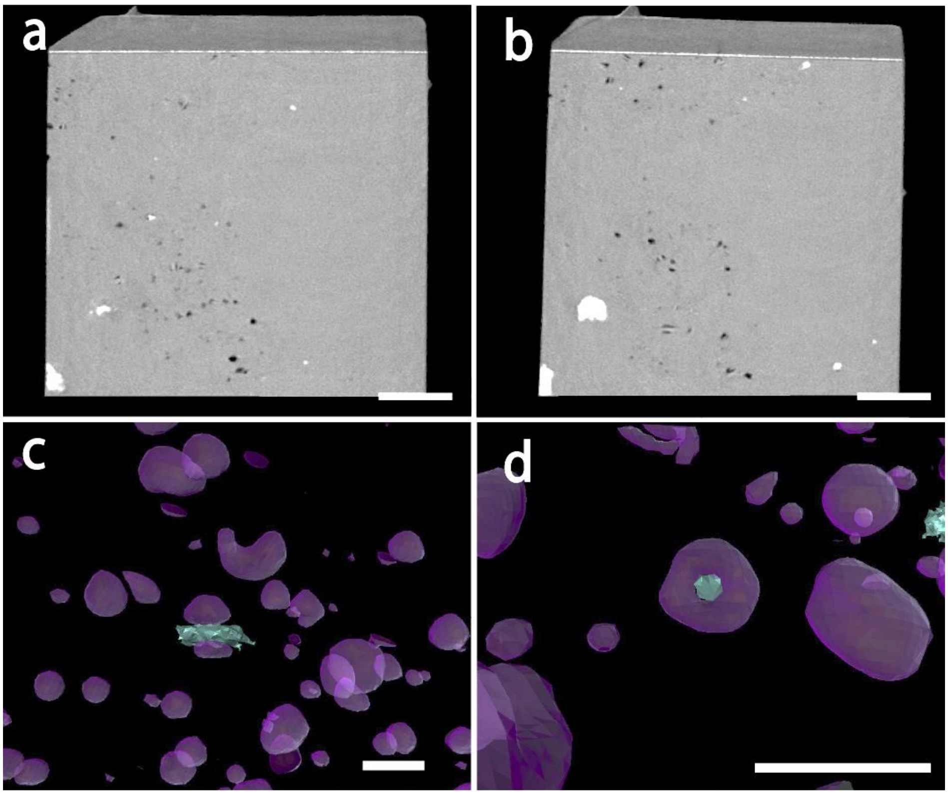

Figure 48 - **a,b,** Lateral views of sample HG1 showing some denser (white) anhedral crystals and the dark, low-density blob structures of different dimensions, commonly disposed in pairs parallelly. The top of the sample shows the layer of carbon used for the protection during the FIB-milling and the thin layer of gold used for the SEM microscopy. Scalebar: 2 μm. **c,** Details of blobs showing a "horseshoe" morphology and a paired disposition with a crystal of the tabular within. **d,** detail of a blob with a small crystal immersed within it. These morphologies suggest that the tabular crystals precipitate within the blobs of low-density material. Scalebar 0.5 μm.

Source: By the author

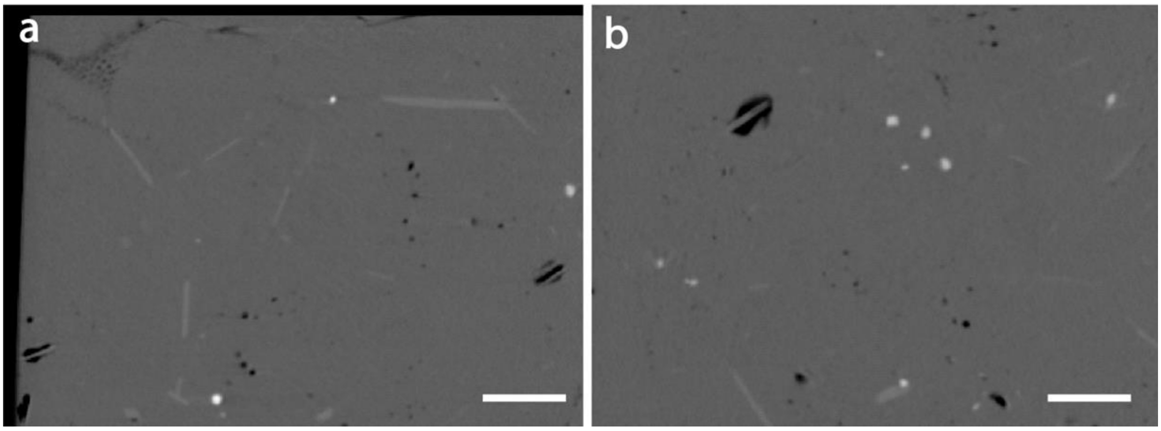

Figure 49 – Details of sample KB2 **a,** different materials distributed within the matrix, including tabular minerals (light grey) of variable lengths, denser (white) spheroid-like non-hollow crystals, and low-density blobs (black/ dark grey), with variable shapes and sizes, including in parallel pairs and triple parallel distribution. In the top left of the image, this dark material is arranged forming a discontinuous layer of blobs, suggesting that these blobs could be remnants of the material that filled fractures. **b,** one large blob (upper left) outlining the morphology of tabular crystal but not completely disrupted by it. This supports the hypothesis that the growing of tabular minerals within these blobs generated the parallel pair observed in all the samples. Scalebar: 1 μm

Source: By the author

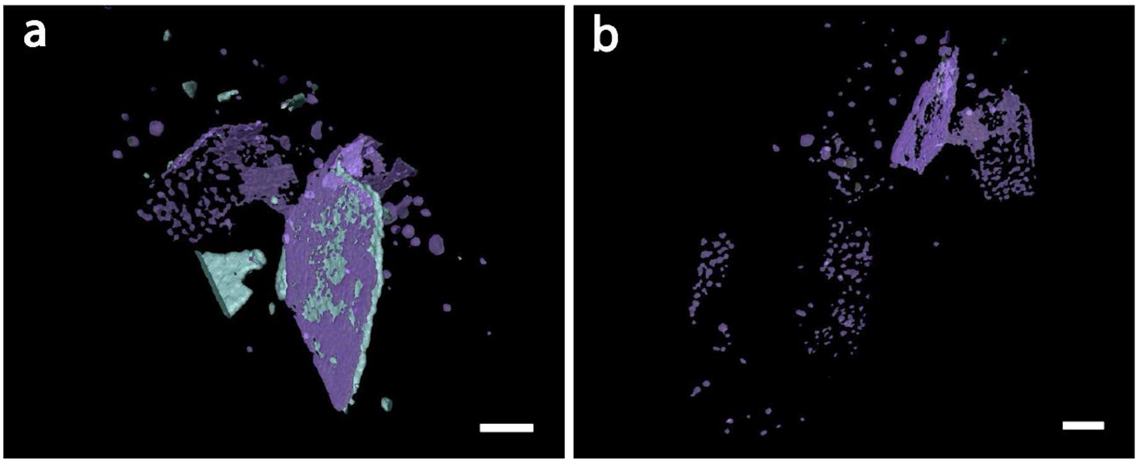

Figure 50 - **a,** Detail of sample KB1 showing the low-density material that is found in blobs and parallel pairs (purple) coating the tabular crystal (dark green). The disruption of layers of the low-density material creates small blobs. **b,** Detail of only the low-density material with a high degree of discontinuity, forming blobs oriented in layers. These patterns supports the hypothesis these represent remains of the material initially filling fracture. Scalebar: 1 μm

Source: By the author

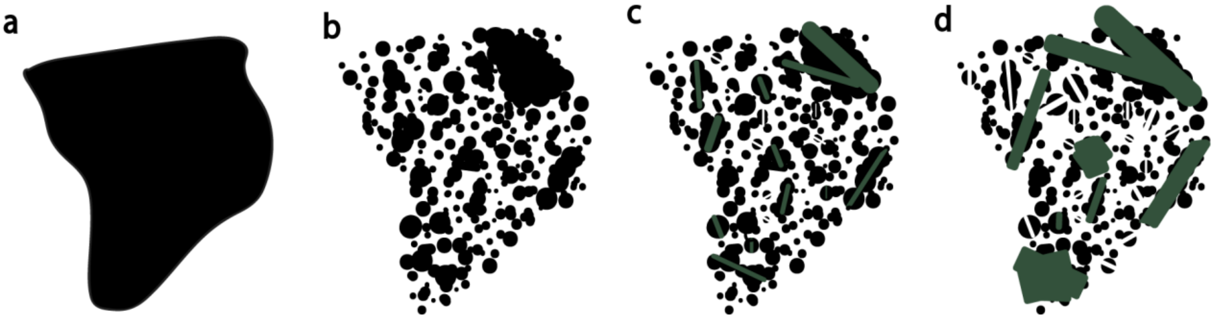

Figure 51 – Schematic representation of the formation of the low-density material disposed in blobs and parallel pairs, interpreted as fluid inclusions, and of the tabular minerals. **a,** initial fracture filled by fluid, **b,** diagenetic alteration of the filled fracture isolates blobs of fluid inclusions. **c,** tabular minerals starts to precipitate within the blobs. **d**, tabular minerals grow, pushing the fluid away or consuming it. Crystals of small dimensions cannot be distinguished in the images due to partial volume effect and generate the parallel pair distribution of the fluid inclusions. Some of the larger crystals still present remains of the fluids, which are seen as a coating on the crystal larger face.

Source: By the author

A material of higher density (white pixels) has been observed for all samples and probably represent the spherules interpreted as coccoidal microfossils. A closer inspection showed that it was actually composed of two different phases:

- Lower density, anhedral minerals completely filled (not hollow), rendered in orange in the 3D images. Commonly with a spheroidal shape and arranged in groups of two or more, present a mass density around 3.60 g/cm^3 for all samples except HG1, where its density is 3.34 ± 0.06 (Table 5).

- Higher density, euhedral mineral, completely filled. Commonly of octahedral morphology, also found in groups of two or more. Rendered in yellow in the 3D images. Presents a mass density of around 4.44 g/cm^3, and was found only in samples from Kromberg Fm. The morphology and density is consistent with chromite (Cr-spinel), described in this formation in previous studies. (119)

Sample HG2 had a composition slightly different from the rest and also presented other material phases:

- Tabular-to-rod-shaped crystals with variable length (hundreds of nm up to 1 μm). The mass density of 2.98 ± 0.04 g/cm^3 is consistent with the mineral tourmaline, previously described in this formation. (56)
- One object with density of 1.82± 0.21 g/cm^3 and a morphology compatible with the interpretation of a volcanic glass shard.

Table 5 - Phases of compounds observed from the samples of Barberton Greenstone Belt, their respective mass densities (g/cm^3) and candidate minerals

Morphology	KB1	KB2	HG1	HG2	Candidate
Paired	0.32 ± 0.12	0.66 ± 0.30	1.10 ± 0.18		Gas/fluid
Volcanic glass	-	-	-	1.82 ± 0.21	Volcanic glass shard
Matrix	2.68 ± 0.07	2.64 ± 0.03	2.65 ± 0.05	2.66 ± 0.03	Quartz (2.65)
Tabular	2.81 ± 0.07	2.79 ± 0.03	2.55 ± 0.05	2.79 ± 0.03	Mica (2.6-3.4) Calcite (2.71)
Rod-shaped	-	-	-	2.98 ± 0.04	Tourmaline (2.9 – 3.1)
Spheroid	3.63 ± 0.09	3.60 ± 0.05	3.34 ± 0.06 3.58 ± 0.9	3.63 ± 0.05	Titanite (3.48 – 3.6)
Octahedral	4.50 ± 0.11	4.42 ± 0.10	-	-	Chromite (4.5 – 4.8)

Reference minerals source: www. mindat.org (112)

Source: By the author

As shown in Table 5, the sample HG1 presented different pattern of densities compared to other samples, with lower values for the tabular and spheroidal minerals. Inside some spheroids, small inner nuclei of higher density were found presenting a density of 3.58 ± 0.9, consistent with the spheroids present in the other samples (**Erro! Fonte de referência não encontrada.**c,d).

4.4.2 DISCUSSION OF THE MORPHOLOGICAL FINDINGS

Kromberg samples

Both samples KB1 and KB2 presented several of the denser crystals (rendered in orange and yellow in the 3D images) that were probably interpreted as putative coccoidal bacteria in the petrographic analysis.

The proportion between the lower-density spheroidal crystals and the higher-density octahedral crystals changed between both samples (Figure 52Figure 54). Some of these crystals are more perfectly spheroidal, but some, specially the smaller, present more irregular morphologies. Dispositions in pairs, similar to dividing cells, can be observed in both samples(Figure 53b,c,Figure 54b,d), but are relatively rare if compared to the amount of octahedral crystals found with this disposition (Figure 52b,c, Figure 53b).

It is important to mention that spheroids with diameter below six times the spatial resolution (*i.e*, 388.2 nm for KB1 and 352.2 nm for KB2) suffer from considerably partial volume effect as explained in section 3.5.1. This means that these small structures segmented as spheroidal crystals could actually present true densities compatible with the octahedral mineral mixed with silica. Therefore, spheroidal structures below this limit were not considered for the morphometric analysis and their evaluation in the images should consider this precaution. For the octahedral minerals this precaution can be relaxed, since there is no observed material denser than these. Therefore, we do not need to consider that they might represent a small denser phase mixed with silica, and every feature within its range of density can be safely interpreted as belonging to the same material.

Table 6 – Range of diameters (nm) observed for the spheroidal and octahedral crystals

	spheroidal	octahedral
KB1	396.3 - 434.7	89.2 - 761.3
KB2	355.6 - 562.4	107.4 - 608.4

Source: By the author

The morphometric analysis (Table 6) shows that the octahedral minerals are bigger the spheroidal minerals. The analysis of the variation range of diameter of the spheroids is constricted by the lower limit imposed by partial volume effect. Still, the structures have a maximum diameter of 562 nm and variation range minimum of 207 nm can be observed. This range does not exclude a biological interpretation. The octahedral crystals are present in a wider variation range (672 nm) of dimensions, a characteristic inconsistent with a biological origin for these structures.

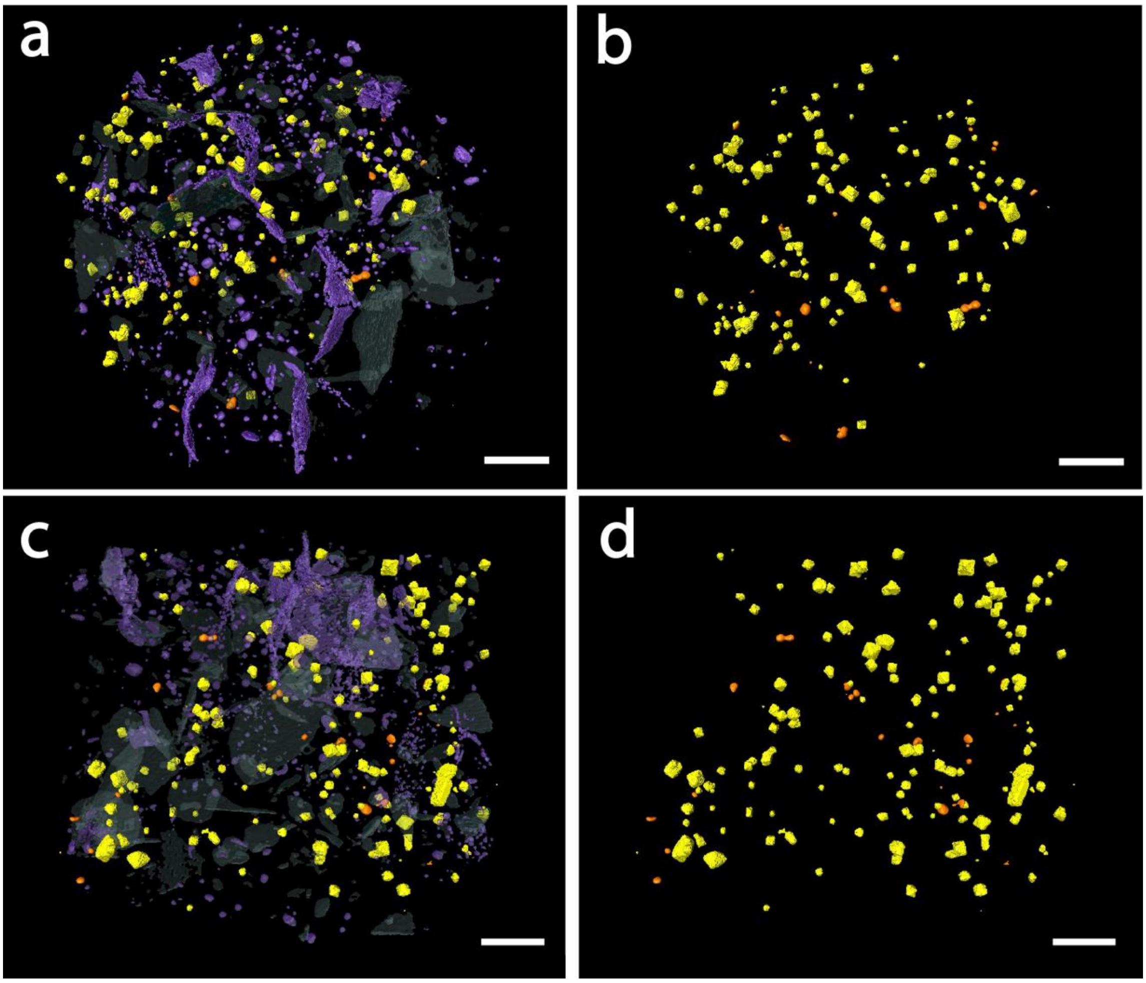

Figure 52 - 3D overview of the sample KB1. Blob structures are rendered in purple, tabular mineral in dark green, spheroidal in orange and octahedral in yellow. Top view: **a,** All materials present in the sample. The low-density material can be observed in blobs and layers. **B,** Only spheroidal and octahedral crystals. The octahedral crystals are more abundant, can be seen in groups of two or more and reach larger dimensions than the spheroids. **c,d,** Lateral views of the sample with different minerals rendered in 3D. Scalebar: 2 μm.

Source: By the author

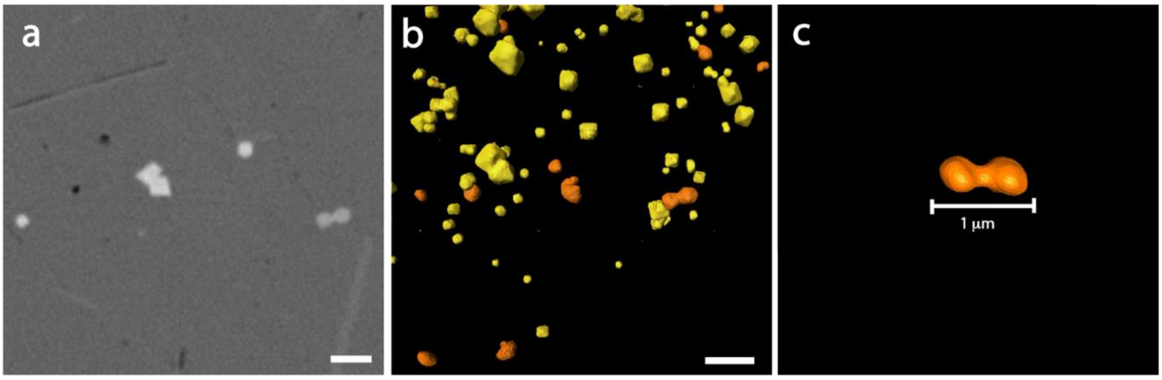

Figure 53 -Detail of sample KB1. **a,** tomographic slice showing the different intensity and shape of the higher density crystals. A pair of lower density spheroids is seen at the left of the image while higher density (white) crystals at the right can present euhedral morphologies. A tabular mineral with a coating of the dark, lower density material is seen in the top-left. **b,** 3D rendering showing the two different types of crystals, with the octahedral presenting more variety of dimensions. Both minerals can be seen in groups of two or more. **c,** detail of the pair of spheroids, resembling dividing cells. Scalebar 1 µm

Source: By the author

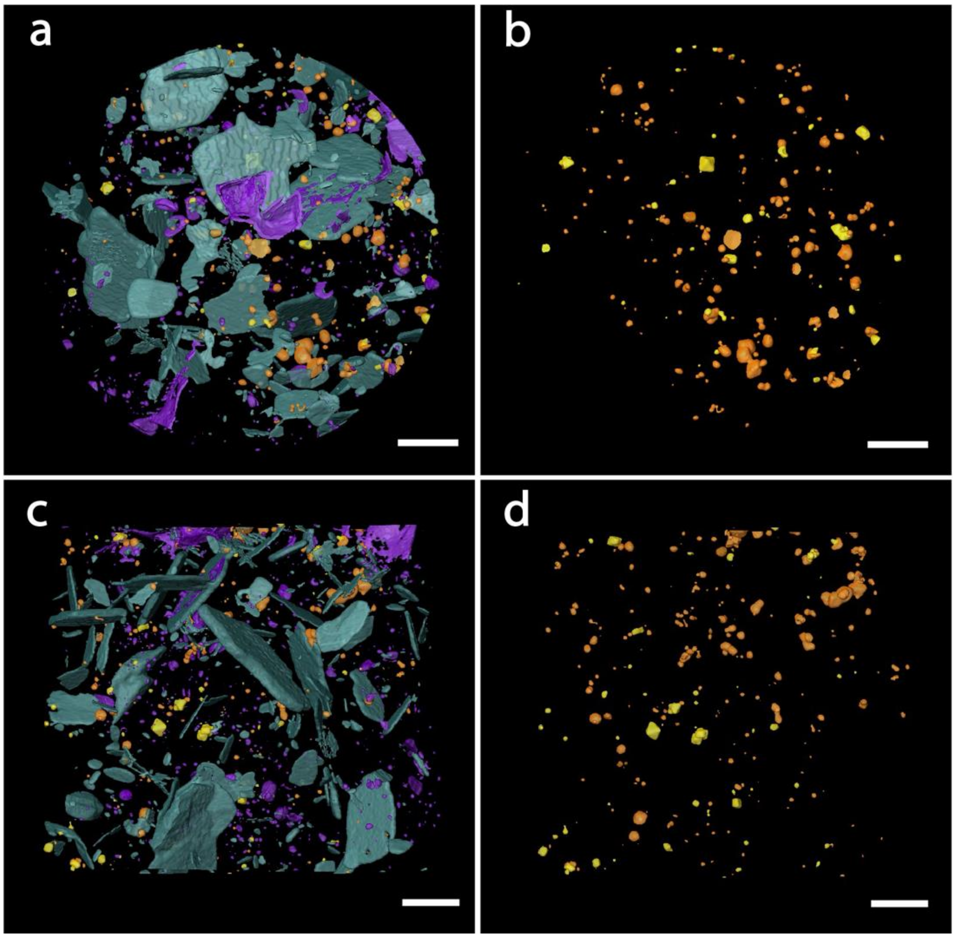

Figure 54 – 3D overview of sample KB2 on top (**a**,**b**) and lateral views (**c**,**d**) showing the disposition of the spheroids (orange) octahedral crystals (yellow), tabular minerals (dark green) and low-density blobs/paired features (purple). This sample present more spheroidal crystals and less octahedral than sample KB1, but the smallest spheroidal could represent octahedral crystals misinterpreted due to partial volume effect. Scalebar 2 µm

Source: By the author

Hoogenoeg samples

The samples from Hoogenoeg present some differences if compared to the ones from Kromberg. The tabular minerals from HG samples are smaller than the ones from KB. There is no higher density crystals similar to the octahedral crystals from Kromberg, and only one crystal with corresponding density was observed, but presenting tabular shape (Figure 56d,e). The structures similar to spheroids are present but rare bigger and present more irregular shapes than the spheroids from Kromberg. It is not possible to discard the possibility that the structures analyzed morphometrically also comprises more than one nuclei of crystals that grew, joined and formed the larger and irregular features.

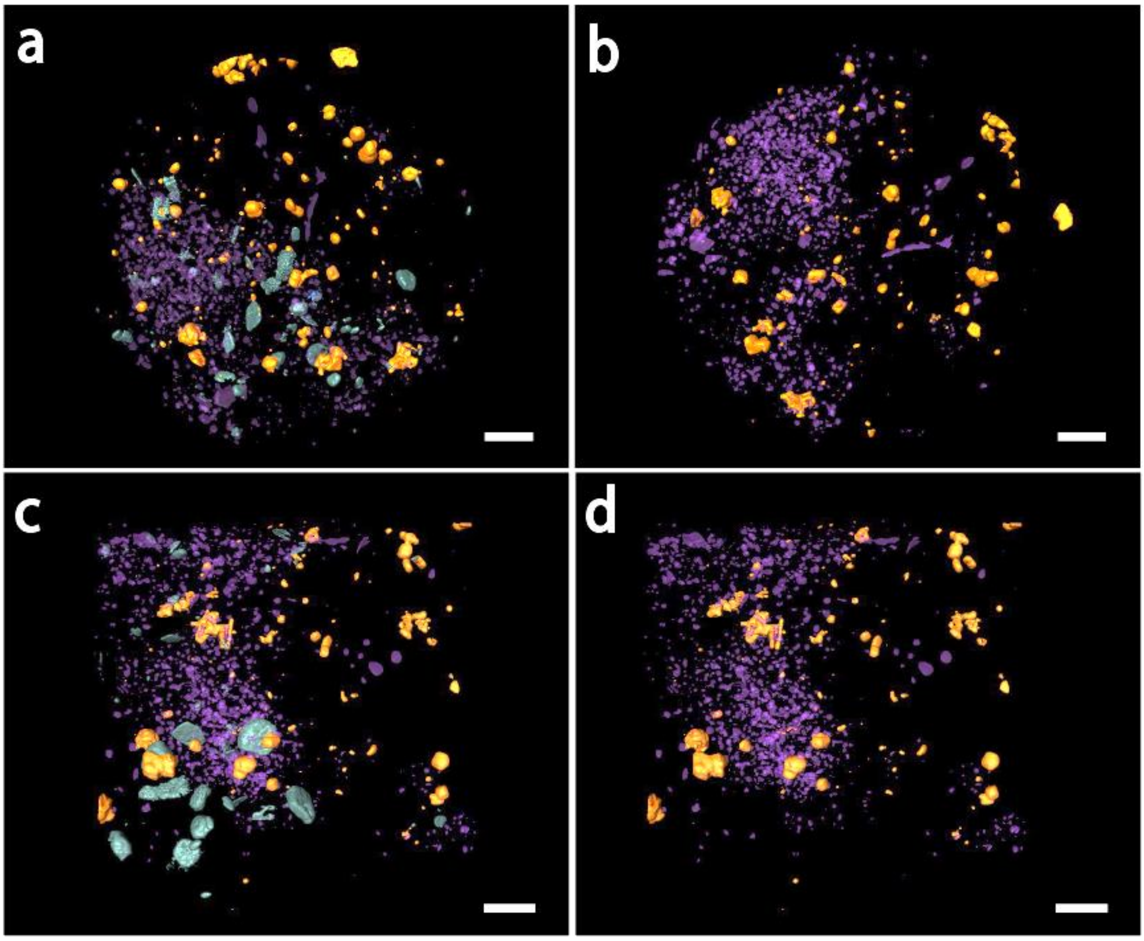

Figure 55 – 3D Overview of sample HG1 in top (**a**,**b**) and lateral views (**c**,**d**) showing the disposition of the spheroids (orange), tabular minerals (dark green) and blobs/paired features (purple). **a,c** distribution of all materials showing a spatial correlation of the distribution of tabular minerals with the blobs. **b,c,** distribution of spheroids and blobs presenting no spatial correlation. Scalebar: 2 μm

Source: By the author

In the sample HG1 (Figure 55), the low-density material is concentrated in one half of the rock pillar. It is possible to observe some spatial correlation of the tabular minerals, which are restricted to the region of the blobs. This supports the interpretation of the origin of the tabular minerals to be linked to the presence of this low-density material. No spatial correlation is observed by visual inspection for the spheroids.

Table 7 - Range of diameters (nm) observed for the spheroidal crystals.

	spheroidal
HG1	296.0 – 961.0
HG2	430.5 – 1240.3

Source: By the author

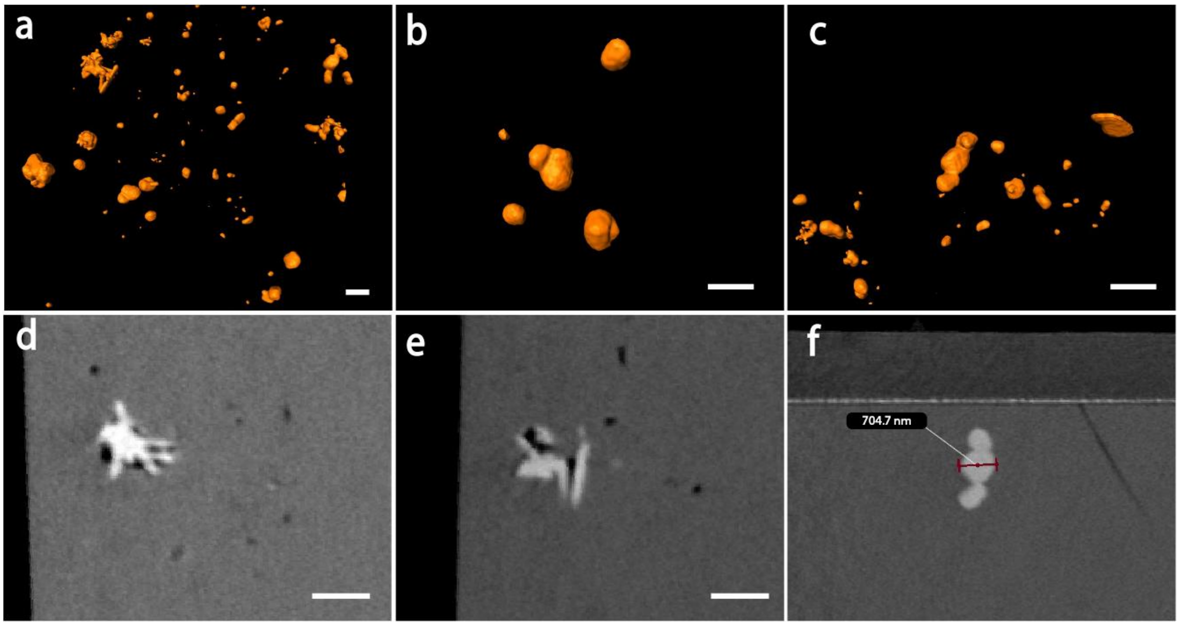

Figure 56 – 3D rendering and tomographic images of spheroids of sample HG1. **a,** Overview of the different morphologies of the crystals **b,** spheroidal crystals with small protuberances of smaller crystals growing **c,** irregular crystals including three joined. **d,e,** tomographic slice of crystals of slightly higher density with tabular morphologies, surrounded by dark material. **f,** three connected spheroids. Scalebar: 1 μm

Source: By the author

The sample HG2 presented a very particular composition, different from all other samples from the BGB. The first remarkable difference is that the tabular and spheroidal minerals present a lower density if compared to all other samples, including HG1. Small crystals with the expected density (based in the other samples) are found within or in contact with some of the spheroids. This suggests one explanation for the difference in densities observed in minerals in this sample: these minerals were formed by a secondary alteration of other materials, and the measured density could be corresponding to a mixture of the primary and secondary phases.

The mineral with tabular-to-rod-shaped morphology, with density consistent with tourmaline, is present with a spatial correlation to the spheroids (Figure 57b-e). These could represent the rod-shaped features observed in previous studies and interpreted as of putative biological origin. (56)

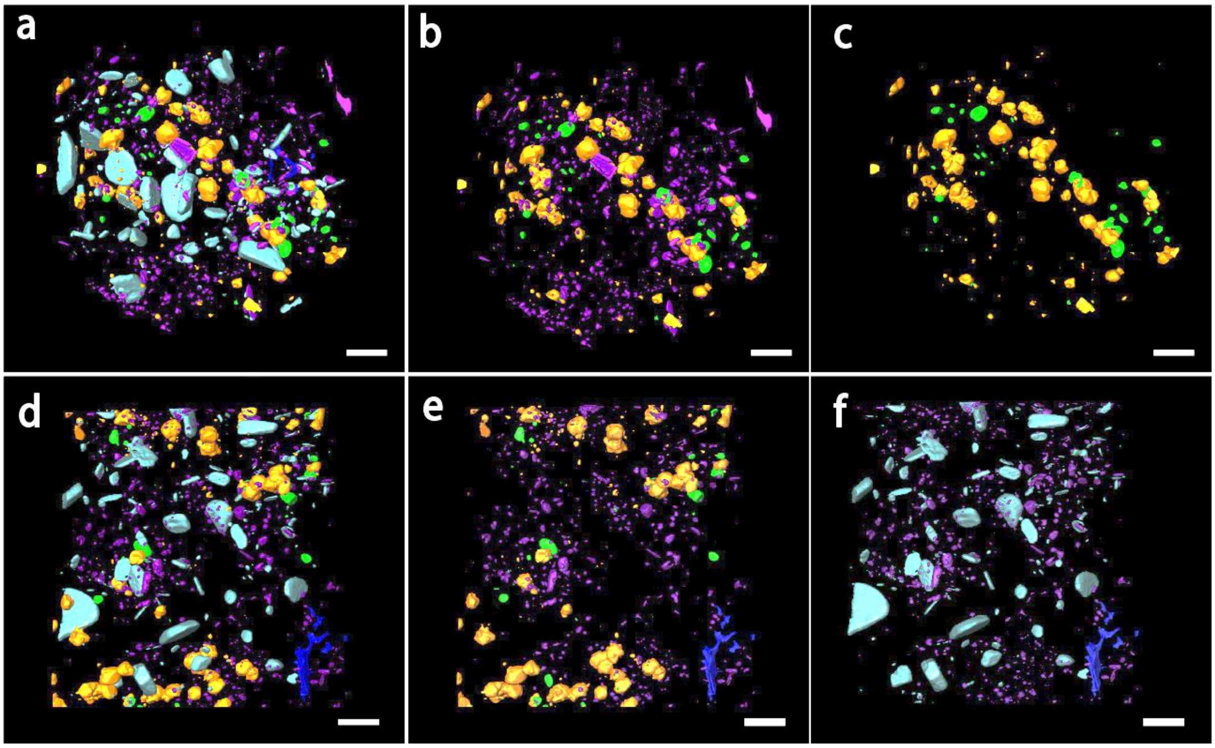

Figure 57 - 3D Overview of sample HG2 in top (**a**,**b**,**c**) and lateral views (**d**,**e**,**f**) Scalebar: 2 μm
Source: By the author

The last material, only found in the sample HG2 is the object with morphology similar to a volcanic glass shard (blue in Figure 57-58). The presence of this material, with lower density and fragmented aspect raise some clues about the origin of the spheroids. Fine-grained titanite has been described preserving traces of alteration of volcanic glass by microorganisms in rocks from Hoogenoeg and Kromberg Formations. (120) When inspected in detail with dark contrast, a minority of the spheroids and octahedra from both KB and HG samples present traces of a dark contour, commonly as a shadowing due to its thin thickness and the mixture with silica (**Erro! Fonte de referência não encontrada.**). This could be remnants of the original material prior to the secondary formation of these crystals, in a process similar to the one described for the tabular minerals (Figure 51). The original material could be volcanic glass shards, fluid inclusions, some lower-density mineral or even microfossils remains. However, due to the small thickness and scarce occurrence, no further interpretation could be attained without additional spectroscopic analysis.

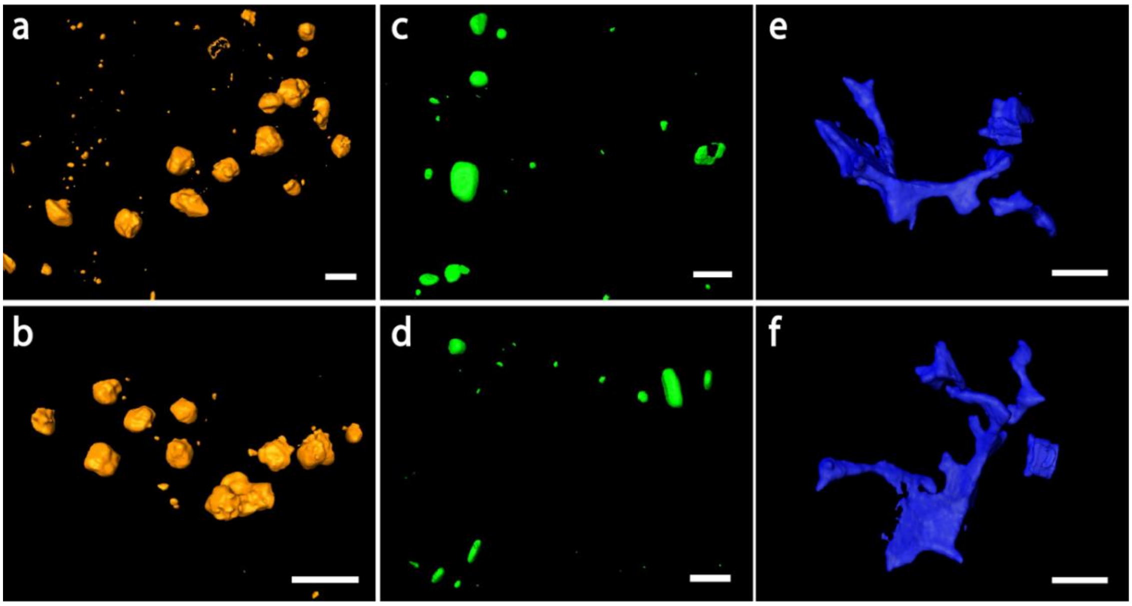

Figure 58 – Detail of features from sample HG2. **a,b,** Spheroidal structures with irregular aspect, some appearing to be joined crystals. **c,** Rod-shaped crystals, slightly tabular when seen in lateral view in **d. e,f,** Object interpreted as a volcanic glass shard. Scalebar 1 µm

Source: By the author

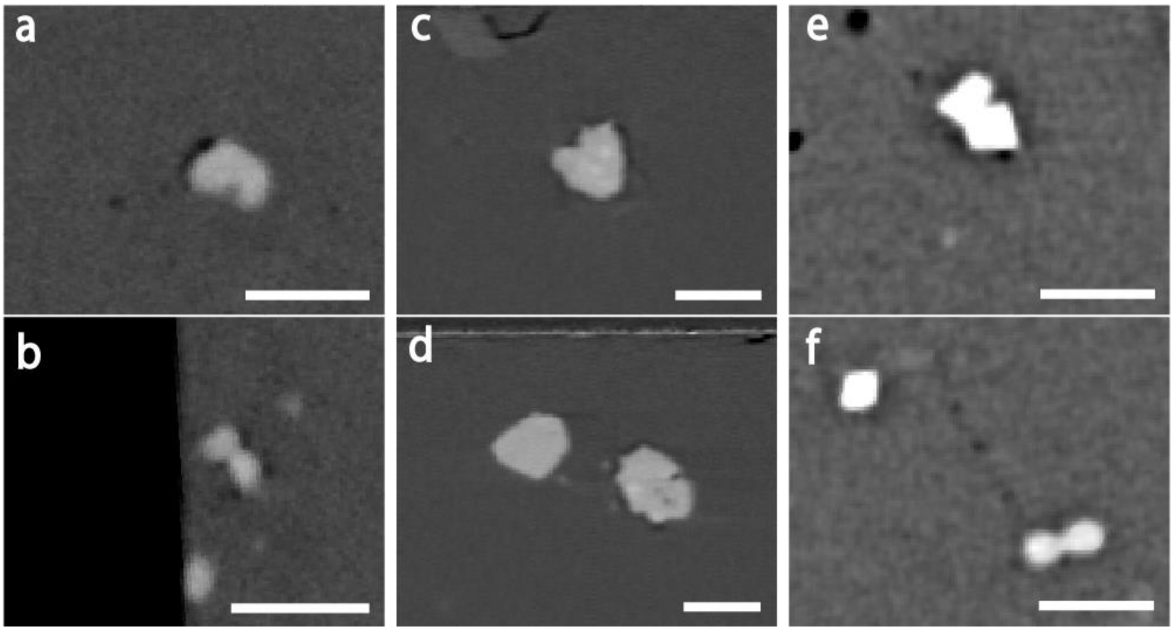

Figure 59 - Details of spheroids (**a-d, f**) and octahedral minerals (**e**) surrounded by a dark layer or shadowing. This could be remnants of the original material prior to a secondary crystallization of these minerals. **a,b** Sample HG1, **c,d** HG2, **e,f,** KB1. Scalebar: 1 µm

Source: By the author

4.4.3 DISCUSSION ON BIOGENICITY

The first characteristic of all the structures that could be considered candidates for putative bacteriomorphs, that is remarkably different from the characters observed for the *bona fide* microfossils from younger samples, is the absence of structures with hollow, cell-wall-like morphologies. Condensed masses of kerogenous material, such as the pattern observed for sample from Gunflint Mink Mountain were also not observed. The dark shadowing observed for some spheroids and octahedral crystals, are also too small to sustain the interpretation of possible cell-wall remains.

Although the disposition of structures in aligned groups could point to the interpretation of cell divisions, this pattern is observed both for the spheroids and for the octahedral crystals from the KB samples. This demonstrates that this type of distribution cannot be unambiguously interpreted as a biogenic character, since the octahedral crystals present morphologies and ranges of size inconsistent with biogenic interpretations.

Morphometric analysis of the spheroids also showed a wide variation of diameter, for the HG samples, which alongside with their irregular morphology, suggest the fusion of two or more anhedral crystals. This is also a characteristic pointing to an abiotic origin for these structures. Since the minimum diameter could not be estimated for the KB samples, this interpretation cannot be extended to those samples.

Considering the classical biogenicity criteria listed in section 1.1 and the biogenic characters observed with PXCT for the other younger *bona fide* microfossils analyzed, we cannot support a biogenic interpretation for the any of the structures observed in the samples from the Kromberg and Hoogenoeg Formations of the Barberton Greenstone Belt.

CONCLUSIONS AND PERSPECTIVES

The results of Ptychographic X-ray Computed Tomography allowed biotic and abiotic structures to be revealed *in situ* within the host rock, providing a unique insight into their nanostructure and micron-scale context without invasive methodological interferences. The results obtained and presented in this thesis comprise novel information for all the samples analyzed, including about aspects of morphology, ultrastructure, geochemical composition, fossilization processes, taphonomic history, traces of taphonomic alteration, and characters for taxonomic identification. These results have led to the elaboration of one manuscript showing the potentials of the approach for the fossils of Gunflint Formation, currently in the process of submission. Two more manuscripts are planned from this set of data: one for exploring the ultrastructural information and paleoecological implications for the fossils of Draken Formation; and one for the taphonomic findings and biogenicity implications of the samples of Barberton Greenstone Belt. The large number of novel findings from different fields of knowledge within paleobiology opens a lot of possibilities that will probably demand further and deeper analyses and interpretations on this data.

The main novelties observed for the samples of each geological unit can be summarized as the follow:

Gunflint Formation

- We observed remarkable different preservations patterns between the filaments from the Schreiber Beach and Mink Mountain localities. For the Mink Mountain, despite the identification of maghemite crystals, the ultrastructural arrangement of the kerogenous material, not delineating the cell walls of the specimens, represents a preservation pattern not recognized so far, and that could have been interpreted as of abiotic origin if observed in other controversial specimens.

- The formation of maghemite in the Mink Mountain specimens suggests a local taphonomic pathway for the iron oxides at the micron scale that, so far, was only described experimentally. The formation of maghemite as a proxy of maturation of organics could also be further explored as a potential biosignature.

- For the Schreiber Beach specimens, the evaluation of ultrastructural features in 3D allows the discrimination of biogenic textures of the cell walls from taphonomic alterations. This can prevent abiotic features such as holes from kerogen displacement caused by secondary crystallization of quartz to be misinterpreted as possible septation.
- Filaments that seem to not present any orientation when analyzed in 2D might have a preferential orientation towards the petrographic slice plane, only distinguishable in 3D. The orientation of filaments can provide additional biofabrics information.

Draken Formation

- Discrimination of ultracellular patterns of the cell walls that were not observed so far. They can help in the taxonomical identification of the specimens and can represent biogenic characters especially important for spheroidal microfossils of simple morphology.
- Cell wall width homogeneity in all 3D planes, also an important biogenicity indicator, especially for simples morphologies.
- Observation of a crystal with a complex structure and that can provide clues of the taphonomic history of the rock.

Barberton Greenstone Belt

- We observed several materials within their geological context, such as fractures, fluid inclusions, volcanic glass and other minerals that provided a picture of the taphonomic history of the rocks.
- We showed that the structures interpreted as coccoidal microfossils comprise two different mineral phases, which are not hollow and present a large variability of size ranges. None of them seem to present membranes or envelopes, nor kerogenous material.
- We could not sustain a biogenic interpretation for any of the features observed in those samples.

In general, the development of the approach for inspecting microfossils with PXCT was successfully developed, and the problems observed, such as the artefacts of sample preparation, provided important references for the aspects that can be further improved. The precision of the sample preparation with the FIB-milling is an important step for this type of analysis. Synchrotrons offer the user a limited time for the execution of experiments and PXCT measurements are time consuming (up to more than ten hours depending on the composition of the sample and the aimed resolution). Therefore, it is important to certify, prior to the experiments, that the sample pillars contain the structures of interest. Two of our samples showed to be shifted in relation to the area of interest, making only part of the fossils to be analyzed, and in one case hindering their proper interpretation. This was probably due to the fact that the correlation of visible light and SEM micrographs was done manually. For a higher precision in the FIB milling of the areas of interest, a correlative microscopy system would be ideal. As discussed more deeply in section 4.2.4, another important procedure for sample preparation is to avoid materials of high density such as platinum in the sample mounting, or to remove all the traces from the region to be imaged, to avoid image artefacts.

In terms of the limitations in contrast, which is a critical aspect for the X-ray imaging of carbonaceous fossils, PXCT allowed us to distinguish the kerogenous material that compose the cell envelopes of different microfossils, such as the ones from Draken and Gunflint Formations. When the structures had small dimensions, *i.e* close to the limit in spatial resolution, partial volume effects from the mixture of two material phases decreased the contrast between the structure and the silica matrix. Still, even some small features, such as the wall envelopes of the specimens from Draken Fm., the final contrast was sufficient for resolving the structures and allowing qualitative 3D analysis and morphometric measurements, and also the visualization of ultrastructural details. However, the quantitative estimation of electron density is limited for these small features. Nevertheless, it is important to stress that the quality of the images, including the capacity of resolving the carbonaceous features is strongly dependent of the quality of the sample preparation, as noted for the samples of Gunflint Fm. and discussed in section 4.2.4.

Comparing our results with FIB-SEM nano-tomography, which is currently the sole 3D nanoscale imaging available for studying Precambrian microfossils, we achieved comparable spatial resolution, considering that the resolution of this electron microscopy approach is practically limited by the slice thickness. PXCT has the advantage of being non-destructive and to provide a resolution/voxel size isometric in 3D (*i.e.* the same in all planes, different from the FIB-SEM). The FIB-SEM has the advantage of allowing elemental maps to be obtained using EDS detectors. The quantitative contrast of PXCT, which allows the mass density estimation, represents a complementary way of assessing the geochemical composition of the materials in 3D, concomitantly with the morphology. Still, the mass density information, even correlated with the morphology, could not resolve all the structures and minerals, especially considering that the minerals can be pseudomorphs of secondary origin or be present in the form of anhedral crystals. Another important limitation is the fact that the possible presence of porosities or features in the order of the spatial resolution can generate partial volume effect and lead to wrong estimative of mass density. In any case, a previous knowledge of the materials and minerals described in those rocks and expected in the sample are also required for the interpretation of these results. Nonetheless, as the sample remains intact, further spectroscopic analysis can be performed to allow these ambiguities to be resolved.

Even considering this weakness, the mass density estimations still represents a crucial characteristic of PXCT for the investigation of microfossils, their taphonomic history and biogenicity. This is especially important for allowing the discrimination of kerogen from other compounds and minerals and even from other carbonaceous material of higher density, such as amorphous graphite. This compound can be formed abiotically and be interpreted as biogenic kerogen, as pointed by Brasier et al. in the debate regarding the biogenicity of the Apex Chert structures. (25,48) Still, it is important to stress that the mass density quantification is limited by the size of the structure and the spatial resolution obtained, as discussed in section 3.5.1, which can be especially critical for the thin and discontinuous materials that form the cell envelopes.

For simple life forms such as Precambrian cells, morphology alone can be an ambiguous indicator of biogenicity. The application of PXCT for the investigation of such structures have shown to allow the correlation of several other aspects, such as micro-scale geological and population contexts and geochemical information. These, integrated with nanoscale morphological and ultrastructural information, represent a promising approach for future investigations of Precambrian microfossils.

FUTURE PERSPECTIVES OF SYNCHROTRON IMAGING FOR PALEOBIOLOGY

The recent developments in synchrotron sources brings also good perspectives for the field of paleobiology. The novel 4th generation sources such as MAX IV in Sweden, Sirius in Brazil, and the upgraded sources ESRF-II in France, APS-U in the USA and Spring8-II in Japan are opening up new avenues for the nanoscale investigation of different types of materials.

For paleobiology, these machines will allow the achievement of nanometric spatial resolution for resolving preserved microfossils and also microbial-mineral interactions with different imaging methods, high energy and high spectral resolution for probing, mapping and speciating heavy Z elements and high sensitivity to elements in trace concentrations. The possibility to explore chemical and morphological biosignatures at the nanoscale have the potential to represent a new revolution in the study of early life, consolidating the emerging field of nanopaleontology.

In Brazil, the coherent X-ray nanoprobe beamline CARNAÚBA is being developed for delivering to the scientific community spectroscopic and imaging techniques with flexible sample environments. This beamline will offer an X-ray beam up to ~30 nm for techniques as X-ray fluorescence, X-ray absorption spectroscopy, X-ray excited optical luminescence, X-ray diffraction and multimodal coherent diffraction imaging techniques. This will allow elemental, mineralogical and morphological information to be correlated in 2D and 3D with nanometric resolution. Such multi-technical approach will constitute a powerful way of restricting the interpretations of biogenicity for controversial biosignatures. This beamline will be a tool for the scientific community, including early life scientists, to inspect complex samples at the nanoscale with complementary analytical methods. Finally, in the context of the Mars sample-return missions planed by NASA and ESA for the following decades, the capabilities of synchrotron methods for detecting traces of life also emerges as important future venues for the non-destructive investigation of the most precious scientific samples of the human history.

REFERENCES

1 KELLEY, P. H. et al. From paleontology to paleobiology: a half-century of progress in understanding life history. In: BICKFORD, M. E. (Ed.). *The web of geological sciences*: advances, impacts, and interactions. New York: Geological Society of America; 2013.

2 GOMES, A. L. S. et al. Paleometry as a key tool to deal with paleobiological and astrobiological issues: some contributions and reflections on the Brazilian fossil record. *International Journal of Astrobiology*, p. 1–15, 2019. doi: 10.1017/S1473550418000538.

3 RIQUELME, F.; RUVALCABA-SIL, J. L.; ALVARADO-ORTEGA, J. Palaeometry: non-destructive analysis of fossil materials. *Boletín de la Sociedad Geológica Mexicana*, v. 61, n. 2, p.177–183, 2009.

4 BRASIER, M. D.; WACEY, D. Fossils and astrobiology: new protocols for cell evolution in deep time. *International Journal of Astrobiology*, v. 11, n. 4, p. 217–228, 2012.

5 DONOGHUE, P. C. J. J. et al. Synchrotron X-ray tomographic microscopy of fossil embryos. *Nature*, v. 442, n. 7103, p. 680–683, 2006.

6 GUERIAU, P. et al. Trace elemental imaging of rare earth elements discriminates tissues at microscale in flat fossils. *PLoS One*, v. 9, n. 1, 2014. doi: 10.1371/journal.pone.0086946.

7 BERNARD, S. et al. Evolution of the macromolecular structure of sporopollenin during thermal degradation. *Heliyon*, v. 1, n. 2, p. e00034, 2015.

8 MALDANIS, L. Heart fossilization is possible and informs the evolution of cardiac outflow tract in vertebrates. *eLIFE*, v. 5, 2016. doi: 10.7554/eLife.14698.

9 JAVAUX, E. J. The early eukaryotic fossil record. In: JÉKELY, G. (Ed.). *Eukaryotic membranes and cytoskeleton*. New York: Springer,2007. p. 1–19.

10 DOMAGAL-GOLDMAN, S. D. et al. The astrobiology primer v2.0. *Astrobiology*, v. 16, n. 8, p. 561-653, 2016.

11 MCMAHON, S. et al. A field guide to finding fossils on Mars. *Journal of Geophysical Research Planets*, v. 123, n. 5, p. 1012-1040, 2018.

12 FARLEY, K.; WILLIFORD, K. Seeking signs of life and more: NASA's Mars 2020 mission. *EOS*, 2017 doi: 10.1029/2017EO066153.

13 WILDE, S. A. et al. Evidence from detrital zircons for the existence of continental crust and oceans on the Earth 4.4 Gyr ago. *Nature*, v. 409, n. 6817, p. 175-178, 2001.

14 MOORBATH, S. Oldest rocks, earliest life, heaviest impacts, and the Hadean–Archaean transition. *Applied Geochemistry*, v. 20,n. 5, p. 819–824, 2005.

15 ABRAMOV, O.; MOJZSIS, S. J. Microbial habitability of the Hadean earth during the late heavy bombardment. *Nature*, v. 459, n. 7245, p. 419–22, 2009.

16 WACEY, D. et al. Advanced analytical techniques for studying the morphology and chemistry of Proterozoic microfossils. *Geological Society, London, Special Publications*, v. 448, n. 1, p. 81–104, 2017.

17 SANCHEZ, D. F. et al. 2D/3D microanalysis by energy dispersive X-ray absorption spectroscopy tomography. *ScienceReports*, v. 7, p. 16453, 2017. doi: 10.1038/s41598-017-16345-x

18 LEMELLE, L. et al. In situ imaging of organic sulfur in 700-800 My-old Neoproterozoic microfossils using X-ray spectromicroscopy at the S K-edge. *Organic Geochemistry*, v. 39, n. 2, p. 188–202, 2008.

19 ALLEON, J. et al. Molecular preservation of 1.88 Ga Gunflint organic microfossils as a function of temperature and mineralogy. *Nature Communications*, v. 7, n. 1, p. 11977, 2016.

20 LEPOT, K. et al. Iron minerals within specific microfossil morphospecies of the 1.88 Ga Gunflint Formation. *Nature Communications*,v. 8, n. 1, p.14890, 2017.

21 WESTALL, F. et al. Implications of in situ calcification for photosynthesis in a ~3.3Ga-old microbial biofilm from the Barberton greenstone belt, South Africa. *Earth and Planetary Science Letters*, v. 310, n. 3–4, p. 468–479, 2011.

22 WACEY, D. *Early life on earth*. Dordrecht: Springer Netherlands; 2009. (Topics in geobiology; v. 31).

23 MOJZSIS, S. J. et al. Evidence for life on Earth before 3,800 million years ago. *Nature,* v. 384, n. 6604, p. 55–59, 1996.

24 OHTOMO, Y. et al. Evidence for biogenic graphite in early archaean isua metasedimentary rocks. *Nature Geoscience*, v. 7, n. 1, p. 25–28, 2014.

25 BRASIER, M. D. et al. Questioning the evidence for Earth's oldest fossils. *Nature*, v. 416, n. 6876, p. 76–81, 2002.

26 NOFFKE, N. et al Microbially induced sedimentary structures recording an ancient ecosystem in the ca. 3.48 billion-year-old dresser formation, Pilbara, Western Australia. *Astrobiology*, v. 13, n. 12, p. 1103–1124, 2013.

27 WESTALL, F.; HICKMAN-LEWIS, K.; CAVALAZZI, B. Biosignatures in deep time. *Advances in Astrobiology and Biogeophysics*, p. 145–164, 2019. doi: 10.1007/978-3-319-96175-0_7.

28 HICKMAN-LEWIS, K. et al. Most ancient evidence for life in the Barberton greenstone belt: microbial mats and biofabrics of the ~3.47 Ga Middle Marker horizon. *Precambrian Research*, v. 312, p. 45–67, 2018. doi: 10.1016/j.precamres.2018.04.007

29 NOFFKE, N. The criteria for the biogeneicity of microbially induced sedimentary structures (MISS) in Archean and younger, sandy deposits. *Earth-Science Reviews*, v. 96, n. 3, p. 173–180, 2009.

30 MCKAY, D. S. et al. Search for past life on Mars: possible relic biogenic activity in martian meteorite ALH84001. *Science*, v. 273, p. 5277, p. 924–930, 1996.

31 BARGHOORN, E. S.; TYLER, S. A. Microorganisms from the Gunflint Chert: these structurally preserved precambrian fossils from Ontario are the most ancient organisms known. *Science*, v. 147, n. 3658, p. 563–575, 1965.

32 WACEY, D. et al. Taphonomy of very ancient microfossils from the ~3400Ma Strelley pool formation and ~1900Ma gunflint formation: new insights using a focused ion beam. *Precambrian Research*, v. 220–221, p. 234–250, 2012. doi: 10.1016/j.precamres.2012.08.005.

33 MOREAU, J. W.; SHARP, T. G. A transmission electron microscopy study of silica and kerogen biosignatures in ~1.9 Ga gunflint microfossils. *Astrobiology*, v. 4, n. 2, p. 196–210, 2004.

34 SCHOPF, J. W. Solution to Darwin's dilemma: discovery of the missing Precambrian record of life. *Proceedings of the National Academy of Sciences of the United States of America*, v. 97, n. 13, p. 6947–6953, 2000.

35 WESTALL, F.; BONI, L.; GUERZONI, E. The experimental silicification of microorganisms. *Palaeontology*, v. 38, n. 3, p. 495–528, 1995.

36 WESTALL, F. Morphological biosignatures in early terrestrial and extraterrestrial materials. *Space Science Reviews*, v. 135, n. 1–4, p. 95–114, 2008.

37 GARCÍA-RUIZ, J. M. et al. Morphology: an ambiguous indicator of biogenicity. *Astrobiology*, v. 2, n. 3, p. 353–369, 2002.

38 SCHOPF, J. W. Microfossils of the Early Archean Apex chert: new evidence of the antiquity of life. *Science*, v. 260, n. 1991, p. 640–646, 1993.

39 BRASIER, M. et al. A fresh look at the fossil evidence for early Archaean cellular life. *Philosophical Transactions of the Royal Society B*: biological sciences, v. 361, n. 1470, p. 887–902, 2006.

40 SCHOPF, J. W.; KUDRYAVTSEV, A. B. Biogenicity of Earth's earliest fossils: a resolution of the controversy. *Gondwana Research*, v. 22, n. 3–4, p. 761–771, 2012.

41 WACEY, D. et al. Volcanogenic pseudo-fossils from the ~3.48 Ga dresser formation, pilbara, western Australia. *Astrobiology*, v. 18, n. 5, p. 539–555, 2018.

42 BUICK, R. Microfossil recognition in archean rocks: an appraisal of spheroids and filaments from a 3500 M.Y. Old Chert-Barite Unit at North Pole, western Australia. *Palaios*, v. 5, n. 5, p. 441–459, 1990.

43 MENDELSON, C. et al. Proterozoic and selected early Cambrian microfossils: prokaryotes and protists. In: SCHOPF, J.; KLEIN, C. (Ed.). *The proterozoic biosphere*: a multidisciplinary study. Cambridge: Cambridge University Press, 1992. p 175-244. doi:10.1017/CBO9780511601064.007.

44 SCHOPF, J.W.; KUDRYAVTSEV, A. B. Biogenicity of Earth's earliest fossils: aresolution of the controversy. *Gondwana Research,* v. 22, n. 3–4, p. 761–771, 2012.

45 BRASIER, M. D. et al. Critical testing of Earth's oldest putative fossil assemblage from the ~3.5 Ga Apex chert, Chinaman Creek, Western Australia. *Precambrian Research*, v. 140, n.1–2, p. 55–102, 2005.

46 SCHOPF, J. W. Microfossils of the early Archean Apex chert: new evidence of the antiquity of life. *Science*, v. 260, n. 1991, p. 640–646, 1993.

47 BRASIER, M. et al. A fresh look at the fossil evidence for early Archaean cellular life. *Philosophical Transactions of the Royal Society B*: biological sciences, v. 361, n. 1470, p. 887–902, 2006.

48 SCHOPF, J. W. et al. Laser–Raman imagery of earth's earliest fossils. *Nature*, v. 416, n. 6876, p. 73–76, 2002.

49 BRASIER, M. D. et al. Changing the picture of earth's earliest fossils (3.5–1.9 Ga) with new approaches and new discoveries. *Proceedings of the National Academy of Sciences of the United States of America*, v. 112, n. 16, p. 4859–64, 2015.

50 SCHOPF, J. W. et al. SIMS analyses of the oldest known assemblage of microfossils document their taxon-correlated carbon isotope compositions. *Proceedings of the National Academy of Sciences of the United States of America*, v. 115, n. 1, p. 53–58, 2018.

51 SCHOPF, J. W.; KUDRYAVTSEV, A. B. Three-dimensional Raman imagery of precambrian microscopic organisms. *Geobiology*, v. 3, n. 1, p. 1–12, 2005.

52 WILBY, P. R.; MARTILL, D. M. Fossil fish stomachs: a microenvironment for exceptional preservation. *Historical Biology*, v. 6, n. 1, p. 25–36, 1992.

53 GIBSON, E. K. et al. Life on Mars: evaluation of the evidence within Martian meteorites ALH84001, Nakhla, and Shergotty. *Precambrian Research*, v. 106, n. 1-2, p. 15-34, 2001;

54 WILLIAMS, D. B. The transmission electron microscope.In: WILLIAMS, D. B.; CARTER, C. B. (Ed.). *Transmission electron microscopy*: a textbook for materials science. 2nd ed. Berlin: Springer, 2009. p. 3–22.

55 MURPHY, D. B.; DAVIDSON, M. W. Fundamentals of light microscopy and electronic imaging. *British Journal of Radiology*, v. 83, p. 569-577, 2012.

56 WESTALL, F. et al. Early archean fossil bacteria and biofilms in hydrothermally-influenced sediments from the Barberton greenstone belt, South Africa. *Precambrian Research*, v. 106, n. 1–2, p. 93–116, 2001.

57 WIRTH, R. Focused ion beam (FIB): a novel technology for advanced application of micro- and nanoanalysis in geosciences and applied mineralogy. *European Journal of Mineralogy*, v. 16, n. 6, p. 863–876, 2004.

58 SCHIFFBAUER, J. D.; XIAO, S. Novel application of focused ion beam electron microscopy (FIB-EM) in preparation and analysis of microfossil ultrastructures: a new view of complexity in early Eukaryotic organisms. *Palaios*, v. 24, n. 9, p. 616–626, 2009.

59 WIRTH, R. Focused ion beam (FIB) combined with SEM and TEM: advanced analytical tools for studies of chemical composition, microstructure and crystal structure in geomaterials on a nanometre scale. *Chemical Geology*, v. 261, n. 3–4, p. 217–29, 2009.

60 WESTALL, F. et al. Implications of in situ calcification for photosynthesis in a ~3.3Ga-old microbial biofilm from the Barberton greenstone belt, South Africa. *Earth and Planetary Science Letters*, v. 310, n. 3–4, p. 468–479, 2011.

61 HICKMAN-LEWIS, K. et al. X-ray microtomography as a tool for investigating the petrological context of Precambrian cellular remains. *Journal of the Geological Society*, v. 448, 2016. doi: 10.1144/SP448.11

62 ETH ZÜRICH. *The role of the Fourier transform in image formation*. 2015. Available from: <https://www.microscopy.ethz.ch/TEM_mathe.htm>. Accessible at: 23 Aug. 2019.

63 WILLMOTT, P. An introduction to synchrotron radiation. *Journal of Physics A:* mathematical and theoretical. v. 44, n. 8, p. 085201, 2011.

64 RÖNTGEN, W. C. On a new kind of rays. *Science*, v. 3, n. 59, p. 227–231, 1896.

65 KAK, A. C.; STANLEY, M. *Algorithms for reconstruction with nondiffracting sources*. 1999. Avaolable from: <https://engineering.purdue.edu/~malcolm/pct/CTI_Ch03.pdf>. Accessible at: 30 Aug. 2019.

66 PROJECTIONSLICE.png - wikimedia commons. Available from: <https://commons.wikimedia.org/wiki/File:ProjectionSlice.png>. Accessible at: 30 Aug. 2019.

67 PAGANIN, D. et al.Simultaneous phase and amplitude extraction from a single defocused image of a homogeneous object. *Journal of Microscopy*, v. 206, n. 1, p. 33–40, 2002.

68 TAFFOREAU, P. et al. Applications of X-ray synchrotron microtomography for non-destructive 3D studies of paleontological specimens. *Applied Physics A*, v. 83, n. 2, p.195–202, 2006.

69 SUTTON, M. D. Tomographic techniques for the study of exceptionally preserved fossils. *Proceedings of the Royal Society B*: biological sciences, v. 275, n.1643, p. 1587–1593, 2008. doi: 10.1098/rspb.2008.0263.

70 SUTTON, M. D.; RAHMAN, I. A.; GARWOOD, R. J. *Techniques for virtual palaeontology*. Chichester: Wiley-Blackwell; 2014.

71 MIAO, J. et al. Beyond crystallography: diffractive imaging using coherent X-ray light sources. *Science*, v. 348, p. 530-535, 2015.

72 SAYRE, D. Some implications of a theorem due to Shannon. *Acta Crystallographica*, v. 5, n. 6, p. 843, 1952.

73 SAYRE, D. Prospects for long-wavelength x-ray microscopy and diffraction. In: SCHLENKER, M. et al. (Ed.). *Imaging processes and coherence in physics*: proceedings of a workshop held at the Centre de physique, Les Houches, France, March 1979. Berlin: Springer, 1980. p. 229-235. (Lecture notes in physics; v. 112).

74 MIAO, J.; ISHIKAWA, T.; SHEN, Q.; EARNEST, T. Extending X-ray crystallography to allow the imaging of noncrystalline materials, cells, and single protein complexes. *Annual Review of Physical Chemistry*, v. 59, p. 387–410, 2008. doi: 10.1146/annurev.physchem.59.032607.093642.

75 ALS-NIELSEN, J.; MCMORROW, D. Elements of modern X-ray physics. *Physics Today*, v. 55, n. 3, 2002. doi: 10.1063/1.1472397.

76 PFEIFFER, F. X-ray ptychography. *Nature Photonics*, v. 12, n. 1, p. 9–17, 2018.

77 RODENBURG, J. M.; FAULKNER, H. M. L. A phase retrieval algorithm for shifting illumination. *Applied Physics Letters*, v. 85, n. 20, p. 4795–4797, 2004.

78 MAIDEN, A.M.; RODENBURG, J.M. An improved ptychographical phase retrieval algorithm for diffractive imaging. *Ultramicroscopy*, v. 109, n. 10, p. 1256–1262, 2009.

79 THIBAULT, P. et al. High-resolution scanning x-ray diffraction microscopy. *Science*, v. 321, n. 5887, p. 379–382, 2008.

80 THIBAULT, P. et al. Probe retrieval in ptychographic coherent diffractive imaging. *Ultramicroscopy*. v. 109, n. 4, p. 338–343, 2009.

81 THIBAULT, P.; GUIZAR-SICAIROS, M. Maximum-likelihood refinement for coherent diffractive imaging. *New Journal of Physics*, v. 14, n. 6, p. 063004, 2012.

82 DIEROLF, M. et al. Ptychographic X-ray computed tomography at the nanoscale. Nature, v. 467, n. 7314, p. 436–439, 2010.

83 DIAZ, A. et al. Quantitative x-ray phase nanotomography. Physical Review B, v. 85, n. 2, p. 1–4, 2012.

84 DIAZ, A. et al. Three-dimensional mass density mapping of cellular ultrastructure by ptychographic X-ray nanotomography. *Journal of Structural Biology*, v. 192, n. 3, p. 461–469, 2015.

85 SCHELBLE, R. T.; WESTALL, F.; ALLEN, C. C. ~1.8 Ga iron-mineralized microbiota from the Gunflint Iron formation, Ontario, Canada: implications for Mars. *Advances in Space Research,* v. 33, n. 8, p.1268–1273, 2004.

86 LOUGHEED, M. S. Origin of precambrian iron-formations in the Lake Superior region. *Geological Society of America Bulletin*, v. 94, n. 3, p. 325-340, 1983.

87 SHAPIRO, R. S.; KONHAUSER, K. O. Hematite-coated microfossils: Primary ecological fingerprint or taphonomic oddity of the Paleoproterozoic? *Geobiology*, v. 13, n. 3, p. 209–224, 2015.

88 POULTON, S. W.; FRALICK, P. W.; CANFIELD, D. E. The transition to a sulphidic ocean ~1.84 billion years ago. *Nature*. v. 431, p. 173-177, 2004. doi.org/10.1038/nature02912.

89 ALLEON, J. et al. Organic molecular heterogeneities can withstand diagenesis. *Science Reports*, v. 7, n. 1, p. 1–9, 2017.

90 WACEY, D. et al. Nanoscale analysis of pyritized microfossils reveals differential heterotrophic consumption in the 1.9-Ga Gunflint chert. *Proceedings of the National Academy of Sciences of the United States of America*, v. 110, n. 20, p. 8020–8024, 2013.

91 KNOLL, A. H. Microfossils from the Late precambrian Draken conglomerate, Ny Friesland, Svalbard. *Journal of Paleontology*, v. 56, n. 3, p. 755–790, 1982.

92 KNOLL, A. H.; SWETT, K.; MARK, J. Paleobiology of a neoproterozoic tidal flat/lagoonal complex: the draken conglomerate formation, spitsbergen. *Journal of Paleontology*, v. 65, n. 4, p. 531–570, 1991.

93 HICKMAN-LEWIS, K.; WESTALL, F.; CAVALAZZI, B. Traces of early life from the Barberton Greenstone Belt, South Africa. In: *Earth's oldest rocks*. Berlin: Elsevier, 2018. p. 1029–1058. doi: 10.1016/B978-0-444-63901-1.00042-3

94 HOLLER, M. et al. OMNY PIN - a versatile sample holder for tomographic measurements at room and cryogenic temperatures. *Review of Scientific Instruments*, v. 88, n. 11, 2017. doi: 10.1063/1.4996092.

95 HOLLER, M. et al. An instrument for 3D x-ray nano-imaging. *Review of Scientific Instruments*, v.83, n. 7, p. 073703, 2012.

96 HOLLER, M. et al. High-resolution non-destructive three-dimensional imaging of integrated circuits. *Nature*, v. 543, n. 7645, p. 402–406, 2017.

97 HUANG, X. et al. Optimization of overlap uniformness for ptychography. *Optics Express*, v. 22, n. 10, p. 12634-12644, 2014;

98 GUIZAR-SICAIROS, M. et al. Phase tomography from x-ray coherent diffractive imaging projections. *OpticsExpress*, v. 19, n. 22, p. 21345, 2011.

99 GUIZAR-SICAIROS, M. et al. Quantitative interior x-ray nanotomography by a hybrid imaging technique. *Optica*, v. 2, n. 3, p. 259, 2015.

100 VAN HEEL, M.; SCHATZ, M. Fourier shell correlation threshold criteria. *Journal of Structural Biology*, v. 151, n. 3, p. 250–262, 2005.

101 AMIRA-AVIZO SOFTWARE. 2018. Available from: <https://www.fei.com/software/avizo/?LangType=1033>. Accessible at: 30 Aug. 2019.

102 TRTIK, P. et al. Density mapping of hardened cement paste using ptychographic X-ray computed tomography. *Cement and Concrete Composites*, v. 36, n. 1, p. 71–77, 2013.

103 UNGERER, P.; COLLELL, J.; YIANNOURAKOU, M. Molecular modeling of the volumetric and thermodynamic properties of kerogen: influence of organic type and maturity. *Energy and Fuels*, v. 29, n. 1, p. 91–105, 2015.

104 BUZUG, T. M. *Computed tomography.* Berlin, Heidelberg: Springer, 2008.

105 ABEL, R.; LAURINI, C.; RICHTER, M. A palaeobiologist's guide to "virtual" micro-CT preparation. *Palaeontologia Electronica*, v. 15, n. 2, 2012.

106 JAGADISAN, A.; YANG, A.; HEIDARI, Z. Experimental quantification of the impact of thermal maturity on kerogen density. *Petrophysics*, v. 58, n. 6, p. 603–612, 2017.

107 DANG, S.T. A new approach to measure organic density. *Petrophysics*, v. 57, n. 2, p. 112–120, 2014.

108 OKIONGBO, K. S.; APLIN, A. C.; LARTER, S. R. Changes in type II kerogen density as a function of maturity : evidence from the kimmeridge clay formation. *Energy & Fuels*, v. 19, n. 6, p. 2495–2499, 2005.

109 OSTWALD, J.; ENGLAND, B.M. The relationship between euhedral and framboidal pyrite in base-metal sulphide ores. *Mineralogical Magazine*, v. 43, n. 326, p. 297–300, 1979.

110 TISSOT, B. P.; WELTE, D. H. Petroleum formation and occurrence. *Journal of Physics A*: mathematical and theoretical, v. 44, n. 8, p. 085201, 1984.

111 ALFRED, D.; VERINIK, L. A new petrophysical model for organic shales. *Petrophysics,* v. 54, n. 3, p. 240–2472013.

112 MINDAT.org - mines, minerals and more. 2019. Available from: <https://www.mindat.org/>. Accessible at: 23 Aug. 2019.

113 BARRN, V.; TORRENT, J. Evidence for a simple pathway to maghemite in earth and Mars soils. *Geochimica et Cosmochimica Acta*, v. 66, n. 15, p. 2801–2806, 2002.

114 CORNELL, R. M.; SCHWERTMANN, U. *The iron oxides*: structure, properties, reactions, occurences and uses. New York: Wiley-VCH, 2003.

115 STROTHER, P.; TOBIN, K. Observations on the genus huroniospora barghoorn: Implications for paleoecology of the gunflint microbiota. Precambrian Research, v. 36, n. 3–4, p. 323–33, 1987.

116 SCHOPF, J. W. Microflora of the bitter springs formation, late precambrian, central Australia. *Journal of Paleontology*, v. 42, n. 3, p. 651–688, 1968.

117 FOUCHER, F.; WESTALL, F. Raman imaging of metastable opal in carbonaceous microfossils of the 700–800 Ma old draken formation. *Astrobiology*, v. 13, n. 1, p. 57–67, 2013.

118 SCHOPF, J. W.; PRASAD, K. N. Microfossils in Collenia-like stromatolites from the proterozoic Vempalle formation of the Cuddapah Basin, India. Precambrian Research, v. 6, n. 3–4, p. 347–366, 1978.

119 HOFMANN, A.; BOLHAR, R.; ORBERGER, B.; FOUCHER, F. Cherts of the barberton greenstone belt, South Africa: petrology and trace-element geochemistry of 3.5 to 3.3 ga old silicified volcaniclastic sediments. *South African Journal of Geology*, v. 116, n. 2, p. 297–322, 2013.

120 BANERJEE, N. R. et al. Preservation of ~3.4-3.5 Ga microbial biomarkers in pillow lavas and hyaloclastites from the Barberton Greenstone Belt, South Africa. *Earth and Planetary Science Letters*, v. 241, n. 3–4, p. 707–722, 2006.

121 ROBERTS, A. P. et al. Resolving the Origin of Pseudo-Single Domain Magnetic Behavior. *Journal of Geophysics Research: Solid Earth,* v. 122, n. 12, p. 9534–9558, 2017.

122 BOER, C. B. DE & DEKKERS, M. J. Grain-size dependence of the rock magnetic properties for a natural rnaghernite. *Geophysucal Research Letters,* v. 23, p. 2815–2818, 1996.

APPENDIX

Manuscript: Figures of the extended section of the manuscript:

Nanoscale 3D quantitative imaging of 1.88 Ga Gunflint microfossils reveals novel insights into taphonomic and biogenic characters

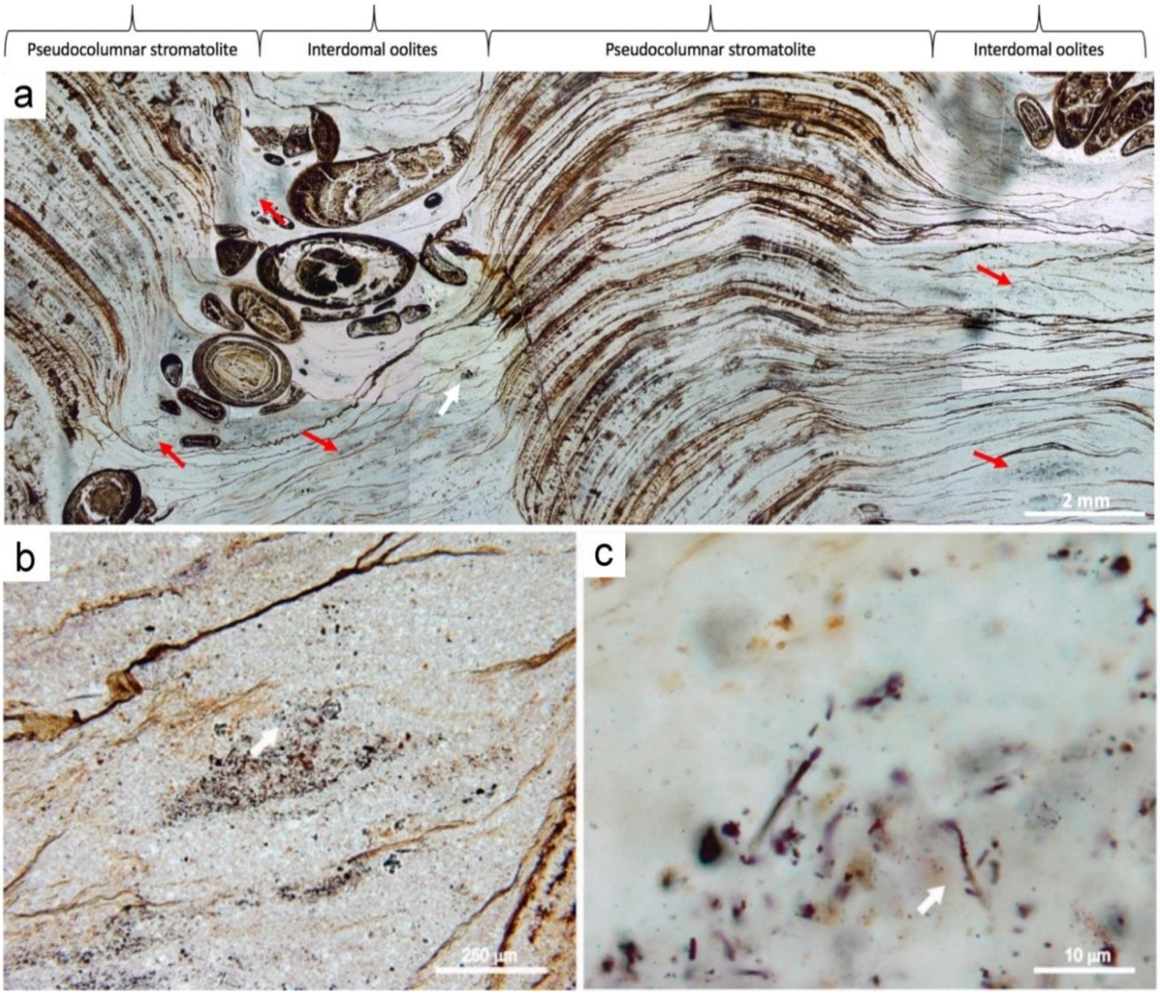

Extended Data Figure 1. Petrographic characterization of Mink Mountain specimens and sample selection from within the limb of a pseudocolumnar stromatolite. **a,** Macro-scale structure in thin section, comprising irregularly spaced stromatolitic columnar structures separated by troughs in which spherical oolites accumulate. Red arrows indicate microfossil-rich zones. The area marked with a white arrow is magnified in **b,c** and indicates the location from where the studied sample was selected. **b** Microfossil-rich region from which a cylinder was extracted for analysis by

PXCT. **c,** Photomicrographs showing the filamentous *Gunflintia sp.* Barghoorn microfossils (arrowed) studied herein by PXCT .

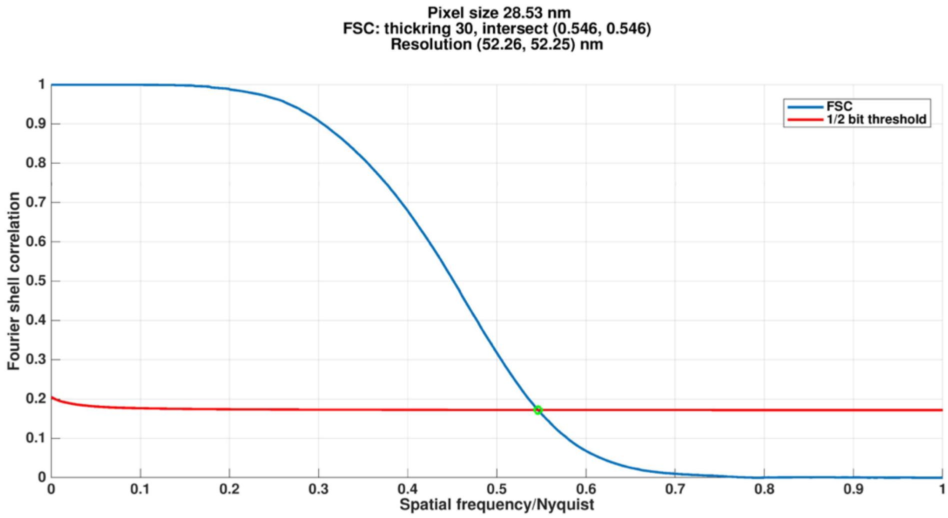

Extended Data Figure 2. Resolution estimation of the Mink Mountain sample by Fourier shell correlation (FSC) yielding a three-dimensional resolution of 52 nm. The point where the FSC curve between two independent 3D reconstructions, each from half of the data, intersects the half-bit threshold curve determines the effective spatial resolution (100).

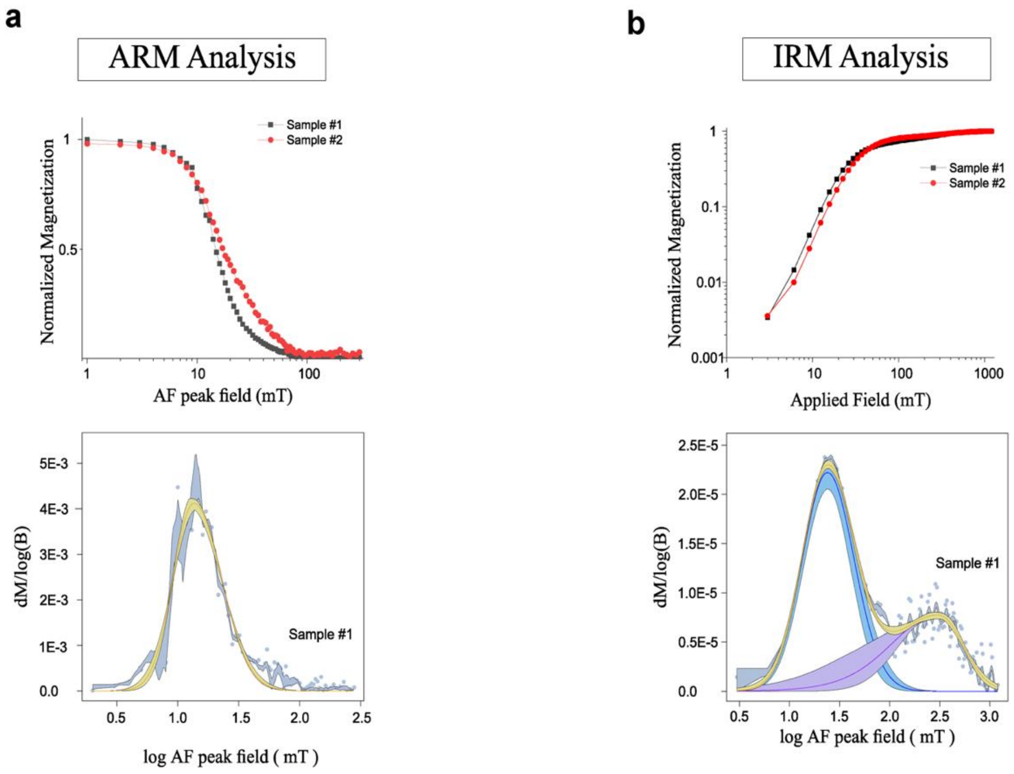

Extended Data Figure 3. Curves of remanence acquisition at room-temperature on two sections of the Mink Mountain sample from which the pillar was extracted for the PXCT analysis. a, Anhysteretic remanent magnetization (ARM) curves indicating an important low-coercivity phase interpreted as maghemite. **b,** Isothermal remanent magnetization (IRM) curves indicating two magnetic components, one of low-coercivity interpreted as maghemite, the other of high-coercivity interpreted as hematite.

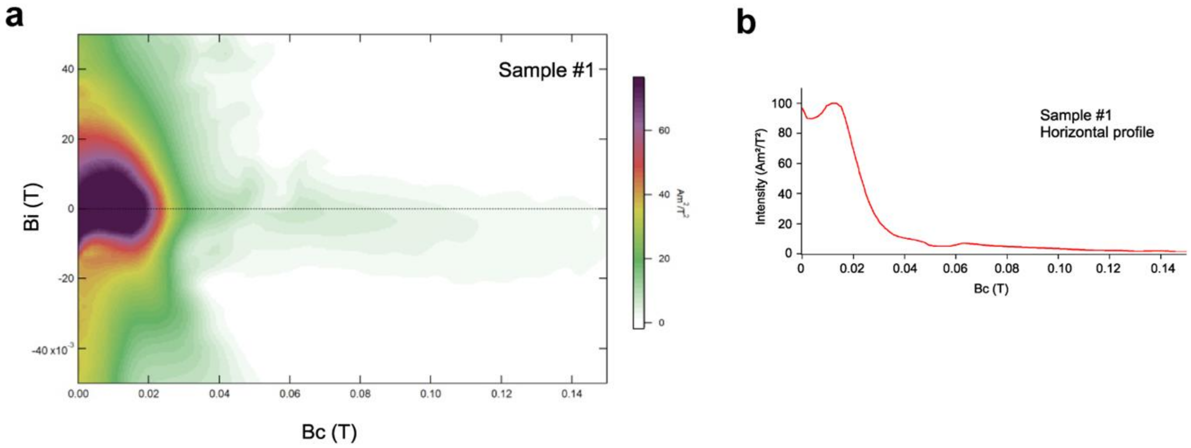

Extended Data Figure 4. First-order reversal curve (FORC) of one section of the Mink Mountain sample from which the pillar was extracted for the PXCT analysis. a, contour map of the mixed partial second derivative FORC function. **b,** Profile along the Bi = 0 line. The FORC is typical of pseudo-single domain particles (121), which for maghemite range between 1 and 20 μm (122), whereas for hematite the pseudo-single domain limit is one order of magnitude larger.

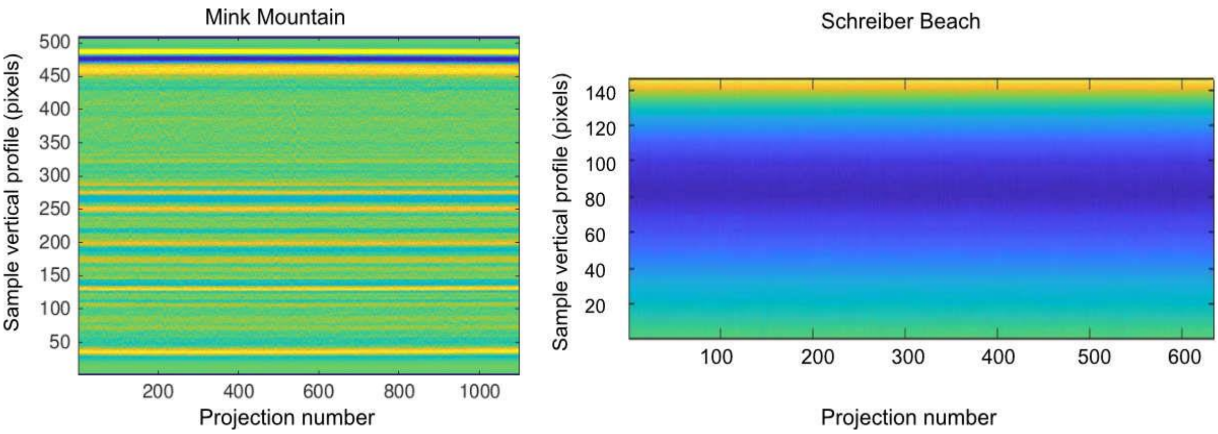

Extended Data Figure 5. Profile of the samples of Mink Mountain and Schreiber Beach after the vertical mass fluctuations alignment (98)**.** The vertical sample mass profile is constant along the 1100 projections. Radiation damage would result in a modification of this sample mass vertical profile, which is not observed here.